UC Merced

UC Merced Electronic Theses and Dissertations

Title

Computing Symbolic Dynamics and Chaotic Transport Rates from Invariant Manifolds

Permalink

https://escholarship.org/uc/item/3cs8h6fs

Author

Sattari, Sulimon

Publication Date

2017

Peer reviewed|Thesis/dissertation

eScholarship.org Powered by the California Digital Library
University of California

UNIVERSITY OF CALIFORNIA, MERCED

DISSERTATION

Computing Symbolic Dynamics and Chaotic Transport Rates from Invariant Manifolds

by

Sulimon Sattari

A technical report submitted

in partial fulfillment of the requirements for the degree of

Doctor of Philosophy in Physics

2017

Committee Members:

Professor Ajay Gopinathan, Chair

Professor Bin Liu

Professor Kevin Mitchell, Advisor

Professor Suzanne Sindi

Portion of Chapter 1 © 2016 American Institute of Physics

Chapter 2 © 2016 American Institute of Physics

All other material © 2017 Sulimon Sattari All rights reserved

The Dissertation of Sulimon Sattari is approved, and it is acceptable in quality and form for publication.

Committee Member:

Professor Suzanne Sindi

Committee Member:

Professor Bin Liu

Committee Chair:

Professor Ajay Gopinathan

Research Advisor:

Professor Kevin Mitchell

Submission Date

Abstract

Computing Symbolic Dynamics and Chaotic Transport Rates from Invariant Manifolds

by

Sulimon Sattari

Doctorate in Physics

Ajay Gopinathan, Chair

University of California, Merced

2017

Abstract

The escape rate of asteroids, chemical reaction rates, and fluid mixing rates are all examples of chaotic transport rates in dynamical systems. A Monte Carlo simulation can be used to compute such rates, for example using a model consisting of a system of ODEs or PDEs. The set of trajectories in a chaotic system can be highly complex, and a Monte Carlo simulation often requires

millions or billions of trajectories to properly sample the state space and compute accurate transport rates. We study methods of computing transport rates using a smaller number trajectories by studying the structure of the state space or phase space. One way to analyze chaotic phase spaces is to compute symbolic dynamics, which is the labeling of trajectories based on a partitioning of the space. The symbolic dynamics of the system can be represented as a network consisting of a set of partition elements, the nodes, and the allowed transitions between them, the edges. In a Hamiltonian system, for example, a partition element represents a region of phase space, and edges connect pairs of nodes between which transport is allowed in time. A firm grasp of the symbolic dynamics results in the ability to compute important transport rates, including the topological entropy and the escape rate.

One way to compute symbolic dynamics is using invariant manifolds which can divide the state space into pieces. The collection of stable and unstable invariant manifolds is known as a heteroclinic tangle, and the topology of the intersections of stable and unstable manifolds in the tangle encodes information about restrictions on the dynamics. The question we address is *How can symbolic dynamics computed from invariant manifolds reduce the number of trajectories required to compute transport rates?* In addition, we ask and try to address *what useful information does the topology of invariant manifolds tell us about a system that is not apparent from direct or Monte Carlo computation of transport rates?* An essential tool in computing the transport rates will be the computation of periodic orbits and using a function called the spectral determinant.

We study several examples of understanding phase space and computing chaotic transport rates using a technique called Homotopic Lobe Dynamics (HLD), which is an automated technique to compute accurate partitions and symbolic dynamics for maps by using the topological forcing by intersections of stable and unstable manifolds of a few anchor periodic orbits. We have applied the HLD technique to analyze and compute transport rates in three systems. In a two-dimensional, double-gyre-like cavity flow that models a microfluidic mixer, we accurately compute the topological entropy over a range of parameter value. In the Hénon map, we use periodic orbits computed from HLD to compute multiexponential decay rates from different zones. In the hydrogen atom in parallel electric and magnetic fields, we use periodic orbits computed from HLD to compute the ionization rate over a range of electron energy where the system exhibits a ternary

horseshoe. In each system, computations of transport rates over ranges of parameter value using HLD provided considerable improvements upon previous attempts to compute the same rates.

Acknowledgments

I gratefully acknowledge my advisor Kevin Mitchell for his mentorship and advice throughout this study, and for helping me improve myself as a researcher. I am thankful for committeee members Ajay Gopinathan, Bin Liu, and Suzanne Sindi for their continued feedback and advice on improving my work and its presentation. I thank my Japanese hosts Tamiki Komatsuzaki, Hiroshi Teramoto, and Mikito Toda for their supervision in the NSF EAPSI program and for teaching me new perspectives on research. I acknowledge the support of the U.S. National Science Foundation under Grant No. PHY-1408127 and the East Asia and Pacific Summer Institutes (EAPSI). I thank Jeffrey Weekley and Sarvani Chadalapaka for assisting me in using the the Multi-Environment Research Computer for Exploration and Discovery (MERCED), which is supported by the National Science Foundation Grant No. ACI-1428783.

Contents

List of Figures

List of Tables

Curriculum Vitae

Education

2011–present PhD, Physics specializing in topological techniques in dynamical systems.
Advised by Prof. Kevin Mitchell.
University of California, Merced. Merced, CA.

2009–2011 BS, Physics and BA, Mathematics.
University of California, Santa Cruz. Santa Cruz, CA

Publications

- Sattari, Chen, and Mitchell. *Using heteroclinic orbits to quantify topological entropy in fluid flows*, Journal of Chaos (2016)

Teaching Experience

2011–2013 Teaching Assistant, Intro. Physics 1/2

Chapter 1

Motivation and Background

A mathematical description of how one state develops into another state over time, also known as a dynamical system, is a fundamental tool for describing physical systems. Dynamical systems model natural phenomena at every length and time scale, for example atmospheric transport, swarming of bacteria, fluctuations in the stock market, evolution of galaxies, and photoionization of atoms [20, 21, 43, 56–58]. A remarkable result of dynamical systems theory is that universal properties apply to large classes of dynamical systems irrespective of physical phenomena and scale. One example of this is in Hamiltonian mechanics, where the same mathematical formalism applies to many types of physical systems. In some cases, the same exact Hamiltonian governs two completely different phenomena, such as in the restricted three-body problem in the Solar system, which, under proper scaling and coordinate transformation, also models a simple unimolecular chemical reaction [42]. Researchers in two different disciplines could be studying the same problem without realizing it, and dynamical systems theory is one field that attempts to bridge such gaps when possible. For example, the methods of normal form theory developed by chemical reaction dynamicists studying electron trajectories were later used by NASA to compute low-fuel spacecraft trajectories in the Solar system [41]. The relationship between chemical and astronomical Hamiltonian physics is only one specific example of universality in chaotic dynamical systems, which is one reason why it is useful to study chaotic dynamical systems from a broad point of view.

Another important universal concept in many dynamical systems, which is one we focus on in our study in this manuscript, is the geometry of phase space. The phase space is the set of all

possible states a trajectory can have in a dynamical system, and there are general statements that can be made about the geometry of the state space of certain classes of systems. For example, it is known that the phase space of a Hamiltonian system cannot contain sinks or sources because of energy conservation. Realistic physical Hamiltonian systems are typically chaotic, and although such systems contain no sources or sinks, the phase space may contain saddle fixed points or elliptic fixed points. The defining property of saddle points is that they have both stable and unstable directions, and each direction has a stable or unstable manifold associated with it which are associated with the backward- or forward-time dynamics of trajectories that begin near the saddle point. The geometry of the stable and unstable manifolds of saddle points, as we will develop in this manuscript, encodes important information about the dynamical system a a whole. Our work involves computing finite segments of stable and unstable manifolds of saddle points, analyzing their topology, and extracting relevant information such as symbolic dynamics, mixing rates, and escape rates by using a technique called homotopic lobe dynamics (HLD). We will unpack this terminology and describe an example of applying the HLD technique to a fluid flow system in Sect. 1.2.2.

We will demonstrate new applications of the HLD technique by studying three different physical systems: a two-dimensional, double-gyre-like cavity flow, the Hénon map, and the hydrogen atom in parallel electric and magnetic fields. In each system, the calculation of transport rates over ranges of parameter value using HLD provide considerable improvements upon previous attempts to compute the same rates. Each application of the HLD technique augments our understanding of it in a unique way. For example, in a fluid flow (Chapter 2) we demonstrate the first example of computing HLD in a fluid dynamics simulation, and explain the mixing by computing the important heteroclinic orbits that stir the fluid, while also providing a comparison to braiding theory an almost cyclic sets. In the Hénon map, (Chapter 3) we provide the first example of using HLD to compute multi-exponential decay rates using periodic orbits, and we compute accurate escape rates from different regions of phase space. In the hydrogen atom in parallel electric and magnetic fields (Chapter 4), we provide the first example of successfully computing ionization rates over a range of electron energy value in a classically chaotic atomic system, which can be useful for studying its quantum counterpart and the relationship between classical and quantum chaos.

Although this work involves purely mathematical models, our findings are promising for experimental applications. The ionization rates computed for the hydrogen atom can be realized in experiments involving Rydberg atoms. Furthermore, the fluid system studied in this paper was designed to mathematically model mixing phenomena in a real, experimental microcavity mixer, and the types of trajectories found responsible for mixing in our study could also be observed in a physical realization of the system. In the Hénon map, the computation of multi-exponential decay rates mimics general Hamiltonian systems where the phase space contains distinct resonance zones.

This introductory chapter is organized as follows. In Sects. 1.1-1.2.2 we introduce our methods for computing symbolic dynamics from tangles. In Sect. 1.1, we introduce saddle points in phase space and their stable and unstable manifolds. In Sect. 1.2, we demonstrate how the stable and unstable manifolds of saddle points intersect each other and form what is called a heteroclinic tangle, and we define a trellis which is used to approximate the heteroclinic tangle numerically. We then demonstrate how symbolic dynamics can be computed from a heteroclinic tangle.

1.1 Saddle points in 2D maps and their stable and unstable manifolds

In this manuscript, we study invertible maps of the plane. In 2D, we study a function that maps a point in the plane (x, y) to another point in the plane (x', y'), and the function can be denoted as $M : (x, y) \in \mathbb{R}^2 \Rightarrow (x', y') \in \mathbb{R}^2$. When M is a discrete-time mapping, the second iterate of M is $M^2 = M((M(x, y)) = M(x', y')$, and M^n can be defined for the map for any $n \in \mathbb{Z}$, assuming M is invertible for negative values of n. Initial points x, y acted on by the mapping iteratively can be viewed as trajectories in time. The mapping could also be a continuous-time mapping, where M is an evolution operator that can be denoted as $M_t(x, y)$, where $t \in \mathbb{R}$ varies continuously, and x and y vary continuously with t. Such mappings are ubiquitous in physics: any Hamiltonian system of p degrees of freedom can be viewed as a mapping M in a $2p$-dimensional space, the system's phase space. By viewing the system stroboscopically at only discrete values of time, i.e., using a Poincaré surface-of section, one can view the system using only discrete-time, which reduces the computational cost of analyzing the state space. A properly chosen Poincaré surface-of section

can retain many important dynamical quantities of the full continuous-time system, and therefore Poincaré surfaces-of-section are important for studying Hamiltonian dynamics using phase space analysis.

We are particularly interested in deterministic mappings M where the system is chaotic, which is more of a rule than an exception in Hamiltonian systems. The Poincaré conjecture states that the domain of a chaotic system is densely populated with saddle points, which exist in both discrete- and continuous-time mappings. What this means intuitively is that no matter where you are in a chaotic region of phase space, there is a saddle point arbitrarily close to you. On the other hand, the set of saddle points is measure zero, meaning it has zero volume. *While the probability of a random measurement landing on a saddle point is zero, the saddle points influence the entire phase space by influencing the local areas near the saddle points.* We harness this important result of chaos theory in the subsequent chapters, and we demonstrate how the invariant manifolds of a few saddle points can accurately compute the symbolic dynamics of the system, which can in turn be used to compute transport rates.

The defining property of saddle points is that they have both stable and unstable directions, as shown in Fig. 1.1. The stable manifold represents the backward-time dynamics of points beginning arbitrarily close to the saddle point, and the unstable manifold represents the forward-time dynamics of points beginning arbitrarily close to the saddle point. Stable and unstable manifolds of saddle points are *invariant*, i.e. points on the stable manifold will always remain on the stable manifold, and they map toward the saddle point going forward in time. Points on the unstable manifold will always remain on the unstable manifold, and they map away from the saddle point going forward in time. This invariant property is why stable and unstable manifolds are important geometric structures for analyzing Hamiltonian phase spaces. As we will show, the invariant properties of stable and unstable manifolds allow us to infer the structure of allowed trajectories in the system.

1.1.1 Computing stable and unstable manifolds numerically

When zooming arbitrarily close to the saddle point, the dynamics is described by the linearization of M, denoted as J. The eigenvector associated with the larger eigenvalue J points in the unstable direction and the eigenvector associated with the smaller eigenvalue of J points

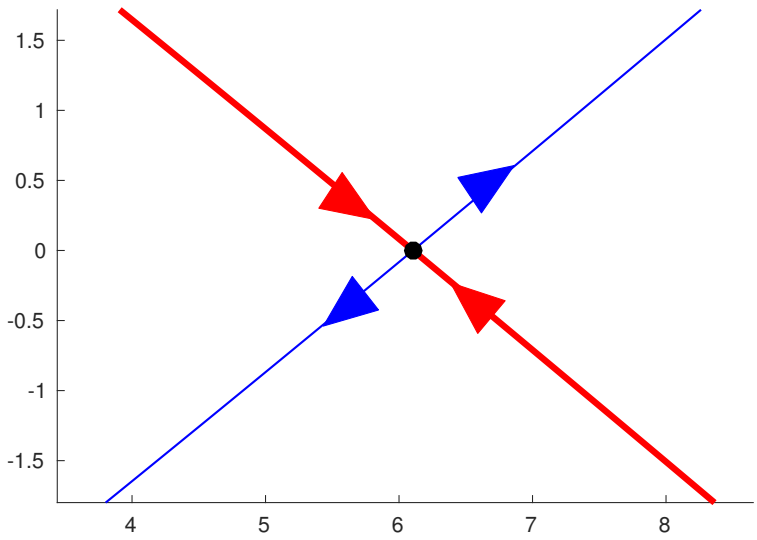

Figure 1.1. The saddle point (black) and its stable and unstable manifolds. The stable manifold (red) represents the set of trajectories near the saddle point going backward in time. The unstable manifold (blue) represents the set of trajectories near the saddle point going forward in time. Points along the stable manifold map toward the saddle point going forward in time. Points along the unstable manifold map away from the saddle point going forward in time.

in the stable eigendirection. The stable and unstable manifolds are computed using the following steps. First, the saddle point is computed either analytically or using a Newton's method solver. Then, the linearization of the map J is computed, either analytically or using finite difference. The eigenvalues and eigenvectors of the J are then computed. A large number of initial points are seeded along the corresponding stable or unstable eigendirection, very close to the fixed point. To compute the stable manifold, points are seeded along the stable direction and then propagated backward in time. To compute the unstable manifold, points are seeded along the unstable direction and then propagated forward in time. Once propagated, the points spread exponentially long and the manifold becomes longer as more and more iterates are taken. In order to maintain sufficient sampling of the manifold as the points spread apart, the manifold is interpolated and points are infilled at each step in the areas having the highest curvature, this ensures that the point density along the manifold remains adequate. The manifolds are used in the HLD technique, as we describe in Sect. 1.2.2. The use of higher-order methods using Bézier curves [31] or an adaptive refinement technique [10] to compute manifolds could lower the computational costs of computing the manifolds and could lead to improvements on utilizing the HLD technique.

1.2 Heteroclinic tangles, trellises and symbolic dynamics

Figure 1.1 shows the zoomed-in picture of the saddle point. Zooming out results in a much more complicated picture, shown in Fig. 1.2. The stable and unstable manifolds curve back and intersect. A collection of stable and unstable manifolds and their intersections is called a **homoclinic** or **heteroclinic tangle**. If the all the manifolds in the tangle are attached to the same fixed point, the tangle is **homoclinic**, and if there are multiple fixed points whose manifolds are included, the tangle is **heteroclinic**. The actual homoclinic or heteroclinic tangle is infinite in length and contains infinitely many intersections, however a finite length computation of a heteroclinic tangle is shown in Fig. 1.2. We denote a finite length computation of the heteroclinic tangle as a **trellis**. The trellis is the object from which we extract the symbolic dynamics, as we develop in the rest of this section. The intersections of the tangle encode information about the future dynamics of the system. An intersection between the stable and unstable manifolds must map to an intersection since it must remain on both stable and unstable manifolds. Furthermore, the iterate $M(p)$ for an intersection p must lie away from the fixed point along the stable manifold, and toward the fixed point along the stable manifold. This implies that the unstable manifold, when computed to longer and longer lengths, makes an infinite number of intersections with the stable manifold that progress closer and closer to the fixed point in time. This is a universal trait maps containing stable and unstable manifolds regardless of physical motivation. We will exploit such properties of heteroclinic tangles in our exploration of fluid and atomic systems in Chapters 2-4.

The dynamics implied by heteroclinic intersections is a form of topological forcing. Topological forcing can be applied to segments of the manifolds. A **bridge** is a segment of the unstable manifold that begins and ends on the stable manifold, with no additional intersections with the stable manifold. A bridge must either map to a bridge or a concatenation of bridges. *We will demonstrate how bridges map to bridges in a predictable manner.* The bridges are classified based on homotopy, which is how they wrap around **holes**. Holes are points in space which encode its topology. Given a smooth, continuous change to the coordinate system, which can be viewed as pulling or squeezing the stable and unstable manifolds, the manifolds will never pass through a hole. Holes can be singularities, certain periodic orbits, or certain heteroclinic intersections. Once a set of holes is chosen, the bridges can be divided up into **bridge classes**. A **bridge class** is a set of

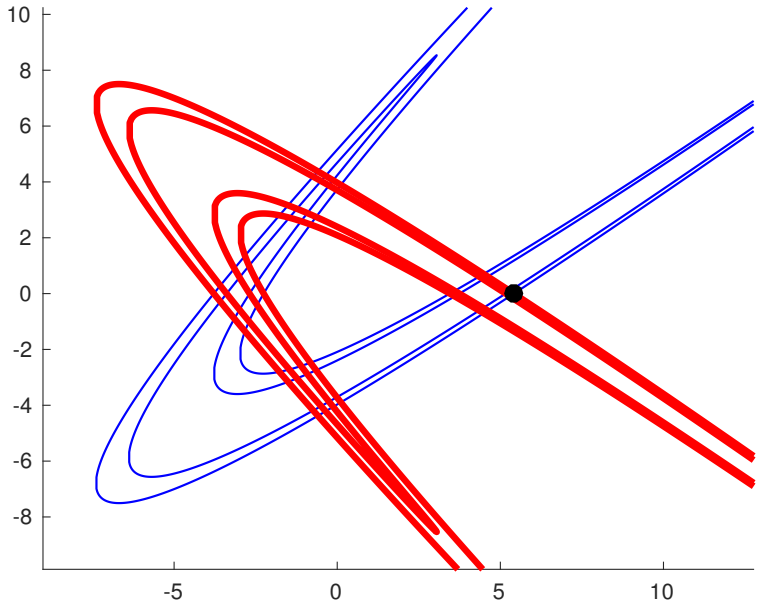

Figure 1.2. An outward zoom of Fig. 1.1. The stable and unstable manifolds curve back and intersect themselves, forming a homoclinic tangle. As the manifold is computed longer and longer, there are an infinite number of intersections. The structure of the intersections encodes the symbolic dynamics of the system, as we develop in this section.

bridges with the same homotopy type, that is, a set of bridges that wrap around the same set of holes. For example in Fig. 1.3c, the colored dots represent holes placed on a period-three orbit. The bridges $W^U_{[\mathbf{p_1},\mathbf{q_1}]}$ and $W^U_{[\mathbf{q_2},\mathbf{p_1}]}$ are both bridges of class $\mathbf{c}$, while the bridge that wraps around the blue hole is of a different class, class $\mathbf{b}$. As we will show in Sect. 1.2.1, once the bridges are divided up into classes, we can compute what classes they map forward to in time. The set of bridge classes and their allowed transitions can be represented by a directed graph and is called the system's **symbolic dynamics**. The **symbolic dynamics** consists of the set of bridge classes, the nodes, and the allowed transitions between them, the edges. In Sect. 1.2.1 we will give an example of computing symbolic dynamics with HLD by placing holes on a period-three orbit. In Sect. 1.2.2, we will show how to systematically place holes on judiciously chosen heteroclinic orbits called pseudoneighbors.

1.2.1 Homotopy types using holes placed on periodic orbits

Consider the heteroclinic tangle shown in Fig. 1.3 (See Chapter 2 for the formulas and the physical motivation for this system). Figure 1.3a shows the fluid flow in its original coordinates. The unstable manifold coming from the top fixed point, denoted $W^U_{\mathbf{z}_u}$ intersects the stable manifold

coming from the bottom fixed point, denoted $W^S_{\mathbf{z}_l}$. The manifolds $W^U_{\mathbf{z}_u}$ and $W^S_{\mathbf{z}_l}$ and their intersections are the heteroclinic tangle. We know a priori that there is a period three orbit labeled $\rho_\mathbf{1}$, $\rho_\mathbf{2}$, and $\rho_\mathbf{3}$ with the following dynamics.

$$M(\boldsymbol{\rho}_1) = \boldsymbol{\rho}_2, \quad M(\boldsymbol{\rho}_2) = \boldsymbol{\rho}_3, \quad M(\boldsymbol{\rho}_3) = \boldsymbol{\rho}_1. \tag{1.1}$$

We refer to these points as holes because as we will see, they can be used to classify the bridges and predict how they map forward in time. Bridge $\mathbf{a}$ wraps around hole $\rho_\mathbf{2}$, bridge $\mathbf{b}$ wraps around hole $\rho_\mathbf{1}$, and bridge $\mathbf{c}$ wraps around hole $\rho_\mathbf{3}$. As we continue to iterate the unstable manifold forward in time, we will encounter bridges of these three types, however, additional bridges can appear whose bridge classes are not yet realized. See Chapter 2 for the dynamics of this trellis for different parameter values of the physical flow,

As we follow the unstable manifold coming from the top of Fig. 1.3, its intersections always progress further and further down the stable manifold as the unstable manifold gets longer and longer. This is because intersections that form later must be closer to the fixed point $\mathbf{z_l}$ along the stable manifold. The unstable bridge connecting $\mathbf{p_0}$ and $\mathbf{q_0}$, denoted $W^U_{[\mathbf{p_0},\mathbf{q_0}]}$ maps to the unstable bridge connecting $\mathbf{p_1}$ and $\mathbf{q_1}$, denoted $W^U_{[\mathbf{p_1},\mathbf{q_1}]}$. Therefore bridges of class $\mathbf{a}$ map to bridges of class $\mathbf{c}$, as shown in Fig. 1.4a. This property holds for all bridges of class $\mathbf{a}$, i.e. bridges that appear when the unstable manifold grows longer that wrap around hole $\rho_\mathbf{2}$. In Fig. 1.3 there are two types of arrows. The unbarbed arrows represent the dynamical direction, the unstable manifold progresses in time along this direction. The barbed arrows all point counter-clockwise and represent the direction in which we define bridge classes. For example, any bridge wrapping around hole $\rho_\mathbf{1}$ in the clockwise direction is denoted $\mathbf{b}$, and any bridge wrapping around hole $\rho_\mathbf{1}$ in the counter-clockwise direction is denoted $\mathbf{b^{-1}}$. The inverse bridge classes are important when we look at how bridges of class $\mathbf{b}$ and $\mathbf{c}$ map forward. Bridges of type $\mathbf{b}$ and $\mathbf{c}$ do not map to bridges, they map to a segment of unstable manifold that intersects the stable manifold in multiple places, creating a concatenation of bridges. The bridge classes generated by mapping forward a bridge of class $\mathbf{b}$, for example, can be determined from the following "game." Draw a curve from point $\mathbf{p_2}$ to point $\mathbf{q_1}$, since those will be the end points of mapping forward the $\mathbf{b}$ bridge $W^U_{[\mathbf{p_1},\mathbf{q_0}]}$. The curve

of course cannot have self-intersections, so there will be a unique curve generated by this game, assuming one does not add extra oscillations in the curve that are not topologically forced. The curve we imagine is drawn in Fig. 1.4b. The curve of type $\mathbf{b}$ maps to a curve that first wraps around hole $\rho_{\mathbf{1}}$ in the clockwise direction, then around hole $\rho_{\mathbf{2}}$ in the clockwise direction, then comes back around hole $\rho_{\mathbf{1}}$ in the counter-clockwise direction. The bridge generated is a concatenation of a bridge of class $\mathbf{b}$, a bridge of class $\mathbf{a}$, and a bridge of class $\mathbf{b^{-1}}$, having an itinerary of $\mathbf{bab^{-1}}$. The "game" of predicting the iteration of bridges can also be played for bridges of class $\mathbf{c}$, shown in Fig. 1.4c. The result of computing the forward iterate of each class $\mathbf{a}$, $\mathbf{b}$, and $\mathbf{c}$ yields the following symbolic representation of the dynamics of this system

$$M(a) = c, \tag{1.2a}$$

$$M(b) = bab^{-1}, \tag{1.2b}$$

$$M(c) = c^{-1}bc. \tag{1.2c}$$

This equation is an example of a system's symbolic dynamics. Assuming that $\rho_{\mathbf{1}}$, $\rho_{\mathbf{1}}$, and $\rho_{\mathbf{3}}$ are the only relevant holes in the system, this symbolic dynamics can be used to encode any trajectory in the system, and is a very useful tool as we will develop in the rest of this manuscript. If our assumption does not hold and more topologically relevant holes exist in the system, this will reveal itself as the unstable manifold is computed longer and longer. Oscillations in the unstable manifold that are too small to observe now, will be stretched out and form new intersections with the stable manifold. These new intersections would then violate Eqs. 1.2, as new combinations of bridge classes will appear, or new bridge classes will appear altogether. The symbolic dynamics we compute in Eqs. 1.2 is then a lower bound on the true symbolic dynamics. Associated with Eqs. 1.2 is a transition matrix T:

$$\mathsf{T} = \begin{array}{c} \\ b \\ c \end{array} \begin{array}{c} \begin{array}{cc} b & c \end{array} \\ \begin{bmatrix} 2 & 0 \\ 0 & 2 \end{bmatrix} \end{array}. \tag{1.3}$$

In this transition matrix, we do not distinguish between a class an its inverse, but we include a 2 in the transition matrix when a symbol and its inverse both appear in the itinerary of an iterated

bridge class. This matrix holds important information about the dynamics of the system. The total number of bridges of a certain class as a function of iterate n goes as T^n. An important theorem known as the Frobinious-Perron theorem for positive, real matrices states that the growth rate of the entries of T^n is equal to the natural log of the largest eigenvalue of T. Here, the matrix T is the transition matrix of a dynamical system's symbolic dynamics, and therefore this growth rate is known as the **topological entropy** of the system. Roughly speaking, more topological entropy means more chaos, and hence more "mixing." We further discuss the symbolic dynamics and topological entropy for a variety of trellises at different parameters of this fluid flow in Chapter 2. The topological entropy can be physically interpreted as the stretching rate of the arc length of a material line [60] in phase space. In addition to the stretching rate of a material line, topological entropy equals the growth rate of the number of periodic orbits as a function of period [77] or the maximum amount of information lost per unit time in a system using measurements with finite precision [59]. Furthermore, topological entropy provides an upper bound on the metric entropy. Practical applications of computing topological entropy include guiding the search of periodic orbits [18], computing mixing rates in microfluidic mixers [5], extracting coherent structures in fluid flows [2], and identifying global regions of high mixing from atmospheric velocity data [37].

We have now demonstrated how holes in phase space can topologically force a specific symbolic dynamics on bridge classes, and that this symbolic dynamics can be used to compute a lower bound on topological entropy. In the following section, we will demonstrate how to identify holes based on the topology of the heteroclinic tangle itself in order to compute symbolic dynamics.

1.2.2 Homotopy types using holes placed on pseudoneighbors

In Sect. 1.2.1, we computed the symbolic dynamics based on the topological forcing of holes placed on periodic orbits. Here, we will compute the symbolic dynamics based on the topological forcing of holes placed on pseudoneighbors. We refer to this technique as **homotopic lobe dynamics (HLD)**. Here we make the important distinction between the heteroclinic tangle, $W^U \cup W^S$, and the **trellis**, $\mathbf{T} = T^U \cup T^S$, where T^U and T^S represent the *finite* length segments of the computed stable and unstable manifolds. The homotopic lobe dynamics technique takes in as input a trellis T.

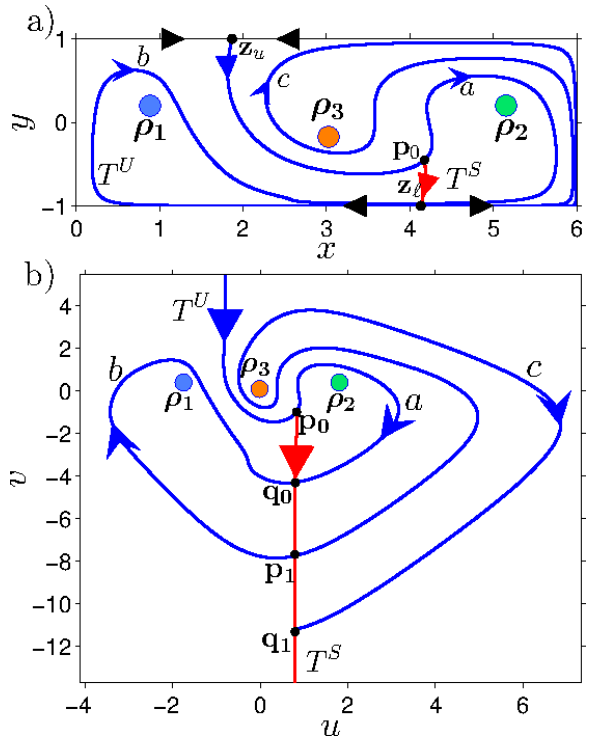

Figure 1.3. The heteroclinic tangle generated from the fluid flow discussed in Chapter 2. The unbarbed arrows represent the dynamical direction, or the direction on which time progresses along the unstable manifold. This direction is also referred to as the dynamical direction. The barbed arrows represent the direction on which the bridge classes are defined, which, in our convention is the clockwise direction. a) The original physical coordinates of the fluid. The unstable manifold coming from the top fixed point intersects the stable manifold coming from the bottom fixed point, forming the heteroclinic tangle. Shown using a coordinate transformation, defined in Chapter 2. The fixed points are now at infinity, but the topologically relevant part of the manifolds is shown. The points of the period three orbit labeled $\rho_\mathbf{1}$, $\rho_\mathbf{2}$, and $\rho_\mathbf{3}$ can be viewed as holes in phase space and bridge classes $\mathbf{a}$, $\mathbf{b}$, and $\mathbf{c}$ are defined by which hole bridges wrap around.

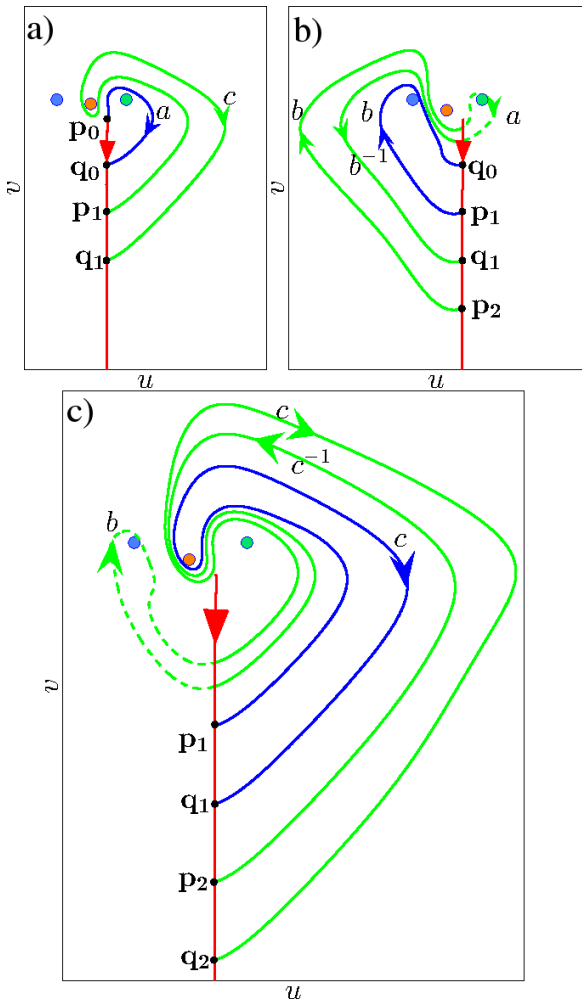

Figure 1.4. The iterates (green) of bridges from each class from Fig. 1.3 (blue). (a) The iterate of the bridge of type a. (b) The iterate of the bridge of type b. (c) The iterate of the bridge of type c.

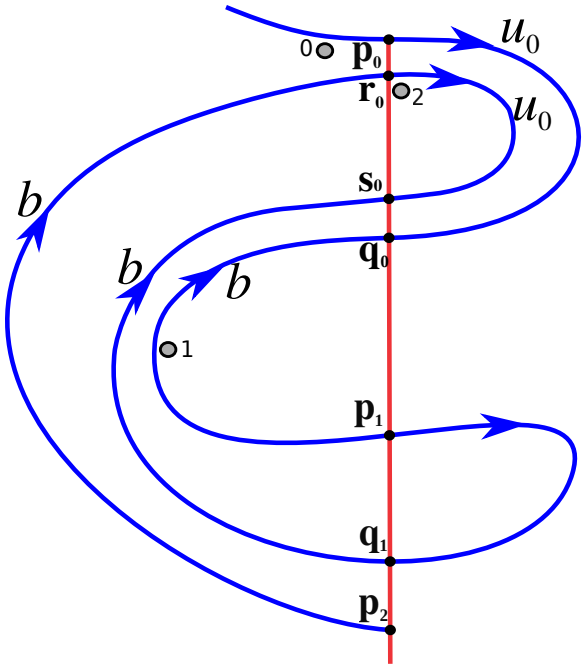

Figure 1.5. A segment of a stable (red) and unstable (blue manifolds). The fixed points attached to the blue manifold at the top of the figure (not shown, since the fixed point lies at infinity in this coordinate space. The pseudoneighbors are shown as grey circles and are numbered based on their ordering, i.e. hole 0 maps to hole 1, and hole 1 maps to hole 2. Hole 3 lies between $\mathbf{p}_1$ and $\mathbf{q}_1$ and does not add any new active symbols to the symbolic dynamics, and is therefore is not shown. The bridges are labeled by their bridge classes u_0 and b. The arrow defines the direction of the bridge class (always clockwise), the dynamical direction is away from the top fixed point.

To define pseudoneighbors, We first construct the set X, which for general n contains all trellis intersections $T_n^U \cap T^S$ iterated forward and backward any number of times,

$$X = \{M^k(\mathbf{x}) \mid \forall \mathbf{x} \in T_n^U \cap T^S, \forall k \in \mathbb{Z}\}. \tag{1.4}$$

Figure 2.8 shows that, for $n = 2$, X is obtained by iterating the four points $\mathbf{p}_0$, $\mathbf{q}_0$, $\mathbf{r}_0$, and $\mathbf{s}_0$ forward and backward,

$$X = \{\mathbf{p}_k, \mathbf{q}_k, \mathbf{r}_k, \mathbf{s}_k \mid \forall k \in \mathbb{Z}\}. \tag{1.5}$$

We next determine the pseudoneighbors of the trellis. Two points $\mathbf{x}, \mathbf{x}' \in X$ are said to form a *pair of pseudoneighbors* if there are no elements of X on either $W^U(\mathbf{x}, \mathbf{x}')$ or $W^S(\mathbf{x}, \mathbf{x}')$. In Fig. 2.8, $\mathbf{r}_0$ and $\mathbf{s}_0$ are a pair of pseudoneighbors, as are any iterates $\mathbf{r}_k$ and $\mathbf{s}_k$. Note that $\mathbf{p}_1$ and $\mathbf{q}_1$ do not form a pair of pseudoneighbors; even though there are no trellis intersections on the intervals

$W^U(\mathbf{p}_1, \mathbf{q}_1)$ or $W^S(\mathbf{p}_1, \mathbf{q}_1)$, the points $\mathbf{r}_1, \mathbf{s}_1 \in X$ lie on the interval $W^S(\mathbf{p}_1, \mathbf{q}_1)$. Similarly, $\mathbf{q}_0$ and $\mathbf{p}_1$ do not form a pair of pseudoneighbors since $\mathbf{r}_{-1}, \mathbf{s}_{-1} \in X$ lie on the interval $W^U(\mathbf{q}_0, \mathbf{p}_1)$. Thus, $\mathbf{r}_k$ and $\mathbf{s}_k$ form the only pair of pseudoneighbor *trajectories* for T_2.

In Sect. 2.4, we punched holes at each point of the period-three orbit $\boldsymbol{\rho}_i$. For the trellis T_n we instead punch holes adjacent to *heteroclinic* orbits. Specifically, for T_2 we punch one hole for each pair of pseudoneighbors $\mathbf{r}_k$ and $\mathbf{s}_k$. This hole is placed within the region bounded by $W^U[\mathbf{r}_k, \mathbf{s}_k]$ and $W^S[\mathbf{r}_k, \mathbf{s}_k]$, and infinitesimally close to either $\mathbf{r}_k$ or $\mathbf{s}_k$; here, we choose $\mathbf{r}_k$. Specifically, Fig. 2.8 shows a hole (denoted by a shaded circle) adjacent to $\mathbf{r}_0$ and within the D-shaped region bounded by $W^U[\mathbf{r}_0, \mathbf{s}_0]$ and $W^S[\mathbf{r}_0, \mathbf{s}_0]$. In Fig. 2.8, we only plot the holes up to hole number 2, which is the first hole to lie adjacent to T^S. Note that an infinite number of holes actually line the right side of T^S, converging upon $\mathbf{z}_\ell$ in the forward time direction. (In the uv-coordinates of Fig. 2.8, these holes progress infinitely far downward.) Mapping hole 2 backward, it lies adjacent to the point $\mathbf{r}_{-1}$. The point r_{-1} is not explicitly shown in Fig. 2.8, but it must lie on the bridge $W^U[\mathbf{q}_0, \mathbf{p}_1]$. Furthermore, hole 0 lies adjacent to point $\mathbf{r}_{-2}$, which lies on $W^U[\mathbf{z}_u, \mathbf{p}_0]$. Similarly, an infinite number of holes lie adjacent to $W^U[\mathbf{z}_u, \mathbf{p}_0]$, converging upon $\mathbf{z}_u$ in the backward time direction (and progressing infinitely far upward in Fig. 2.8.) However, in Fig. 2.8, we only plot the holes back to hole number 0, which is the first to lie adjacent to $W^U[\mathbf{z}_u, \mathbf{p}_0]$.

Note in Sect. 2.4 the holes were punched at exactly the period-three points $\boldsymbol{\rho}_i$. Here, however, the holes are infinitesimal perturbations from the heteroclinic points $\mathbf{r}_k$. Thus, we must use a separate notation and separate labels for the holes than we use for the heteroclinic points.

The homotopy class of a bridge is now defined relative to the holes punched here, rather than holes on the period-three orbit $\boldsymbol{\rho}_i$. On the left side of T_S in Fig. 2.8, there is a single bridge class b, which by convention winds clockwise around hole 1. The symbol b is used for this bridge class because b was used previously for the bridge class of $W^U[\mathbf{p}_1, \mathbf{q}_0]$ in Fig. 2.5. On the right side, there is an infinite sequence of bridge classes u_k, $k \geq 0$, where u_k winds clockwise around hole $2 + k$.

We next determine the dynamics on the bridge classes. Figure 2.8 shows that the bridge $W^U[\mathbf{p}_1, \mathbf{q}_0]$ is of class b and maps forward to $W^U[\mathbf{p}_2, \mathbf{q}_1] = W^U[\mathbf{p}_2, \mathbf{r}_0] \cup W^U[\mathbf{r}_0, \mathbf{s}_0] \cup W^U[\mathbf{s}_0, \mathbf{q}_1]$, whose homotopy class is bu_0b^{-1}. Thus,

$$M(b) = bu_0b^{-1}. \tag{1.6}$$

Refs. [53, 54] emphasize that the bridge dynamics should be represented by a *concise* product of bridge classes. In the present case, a concise product is one in which the bridge classes alternate between being on the left and right sides of T^S. Since b is on the left and u_0 is on the right, Eq. (2.14) is indeed concise.

Next, Figure 2.8 shows that $W^U[\mathbf{p}_0, \mathbf{q}_0]$ is a bridge of class u_0 that maps forward to $W^U[\mathbf{p}_1, \mathbf{q}_1]$, which is of class u_1. More generally,

$$M(u_k) = u_{k+1}. \tag{1.7}$$

All the classes u_k are said to be *inert* because the forward iterate of any one of them never generates more than one bridge class, no matter how many times it is iterated; we call u_0 the *primary* inert class. On the other hand b is said to be *active* because its forward iterate is the product of three bridge classes. We will always denote active classes by a, b, and c, and inert classes by u and v. We will also denote *types* of bridge classes by an index such as u_k, which represents the set of inert bridge classes of type u.

The dynamics of the inert classes contribute nothing to the topological entropy. Thus, we restrict the transition matrix T to the active classes. Since the present case has only a single active class b that maps to two copies of itself, we find

$$\mathsf{T} = [2]. \tag{1.8}$$

We further discuss the symbolic dynamics and topological entropy for a variety of trellises at different parameters of this fluid flow in Chapter 2.

1.3 Summary of manuscript

This manuscript is organized as follows. In Chapter 2 we introduce our first physical application of HLD, a chaotic 2D double-gyre cavity flow, for which we compute topological entropy over a range of parameter value by computing symbolic dynamics using HLD. We compare our result to previously computed data using braiding theory and almost-cyclic sets, and find that the HLD method can explain topological entropy that is left unexplained by previous studies of topological entropy in the system. In Chapter 3 we compute periodic orbits for a 2D chaotic analytic map, the Hénon map. We compute the decay rate over hyperbolic plateaus, which are ranges of parameter where the symbolic dynamics does not change. We also compute multiple distinct decay rates for a parameter value exhibiting multiexponential decay, providing the first successful application of periodic orbit theory to computing multi-exponential decay rates in maps. We compare our results using periodic orbits to Monte Carlo computations of escape and find good agreement. In Chapter. 4 we apply HLD to an atomic scattering problem, the hydrogen atom in parallel electric and magnetic fields. Using HLD, a hyperbolic plateau is are identified, and its symbolic dynamics is computed. The periodic orbits and decay rates are then computed from the symbolic dynamics, and the decay rate is computed from the periodic orbits over a range of initial electron energy value. The decay rate computed from periodic orbits matches Monte Carlo, demonstrating that periodic orbit theory can be used for realistic physical chaotic systems. The computation of periodic orbits in this system will lead to future work in studying quantum resonances.

Chapter 2

Computing topological entropy in a chaotic 2D cavity flow

2.1 Introduction

We begin our journey into applications of HLD by computing topological entropy of fluid systems at very low Reynolds number, i.e. in the Stokes regime. Understanding mixing in such flows has many physical applications ranging from microfluidics [68] to oceanic and atmospheric circulation [37, 74]. We focus specifically on flows in which the fluid velocity field is periodic in time, which means that the dynamics of passive tracers in the fluid exhibit chaotic trajectories. The amount of chaos in the tracer dynamics can be quantified through the topological entropy. In a compact 2D phase space which is not necessarily area-preserving, topological entropy is equal to the exponential stretching rate of a material line embedded in the fluid [59] governed by

$$L(t) = L_0 e^{ht}, \tag{2.1}$$

where h is the topological entropy, L_0 is the initial line length, and $L(t)$ is the length of the line at time t.

Roughly speaking, more topological entropy means more chaos, and hence more "mixing." In addition to the stretching rate of a material line, topological entropy equals the growth rate of

periodic orbits as a function of period [77] or the maximum amount of information lost per unit time in a system using measurements with finite precision [59]. Furthermore, topological entropy provides an upper bound on the metric entropy. Practical applications of computing topological entropy include guiding the search of periodic orbits [18], computing mixing rates in microfluidic mixers [5], extracting coherent structures in fluid flows [2], and identifying global regions of high mixing from atmospheric velocity data [37].

The important question we address is *What is the origin of topological entropy?* Much like how Li and Yorke [48] showed that for interval maps the existence of a period-three orbit implies the existence of orbits with arbitrary period, whose growth rate is bounded below by a minimum topological entropy, we study chaos through the existence of certain topological structures that are "responsible" for the topological entropy. More specifically, the presence of some structures implies a certain minimum amount of topological entropy. We seek those structures that give us the best lower bound.

A recent approach to explaining topological entropy in a fluid flow is to associate the topological entropy with periodic orbits, i.e. the presence of a given periodic orbit of a passive tracer implies a minimum topological entropy for the flow [2, 7–9, 73]. Such a periodic orbit may be imposed externally on the fluid by stirring the fluid with rods following the periodic trajectory [7, 8]. Alternatively, a periodic tracer orbit may already exist within a fluid driven by some other means, and one may imagine virtual, or "ghost," rods following this orbit; for example, it is particularly natural to consider ghost rods placed at stable orbits within a periodic island chain [32, 67, 73, 74]. The topological entropy of the fluid flow implied by the ghost rods is exactly the same as the topological entropy implied by actual stirring rods. All that matters is the presence of the orbit in the flow.

The method of ghost rods was applied by Grover et al. [33, 69] to the "lid-driven" cavity flow, a chaotic 2D double-vortex flow. The flow depends on the driving period τ_f, which can be varied. Grover et al. found that over a particular range of τ_f a period-three orbit produced most of the topological entropy. However, outside this range either the periodic orbit did not exist or the orbit existed but the topological entropy significantly exceeded that of the orbit. Grover et al., examining the former case, accounted for the topological entropy when the period-three orbit did not exist

through the presence of almost cyclic sets [1,26,28,29]. Such sets are nearly coherent regions of the fluid that are advected in a nearly periodic fashion. They were discovered through an analysis of the Frobinous-Perron operator. Even though no periodic orbits where shown to exist within the almost cyclic sets, the topological entropy of the nearly periodic motion of the sets, viewed as though they were true periodic orbits, nevertheless generated a lower bound to the topological entropy of the fluid flow. Furthermore, this bound was tight for the lowest τ_f value for which particular almost-cyclic sets existed, but excess topological entropy, not explained by the almost-cyclic sets, was found for higher values of τ_f. The origin of this excess topological entropy remained unexplained.

In this paper, we propose another technique for explaining the topological entropy of the lid-driven flow, namely through heteroclinic orbits that connect two fixed points on the boundary of the fluid cavity. (Note that "fixed point" throughout the text refers to period-one orbits, i.e. fixed points of the flow map, and not points of zero velocity of the fluid flow.) These heteroclinic orbits persist even for lower values of τ_f where the period-three orbit fails to exist. In fact, they persist all the way down to $\tau_f = 0$. Like periodic orbits, heteroclinic orbits also have an associated topological entropy that provides a lower bound to the topological entropy of the fluid flow that contains the orbit. Roughly speaking, the heteroclinic orbits that we consider are "remnants" of the period-three orbit that exists at higher τ_f values. We compute the topological entropy from these heteroclinic orbits using the technique of homotopic lobe dynamics [52–55] (HLD). In general, HLD extracts symbolic dynamics from a *tangle*, i.e., transversely intersecting stable and unstable manifolds attached to unstable periodic orbits. The HLD technique proceeds by placing holes at certain tangle intersections, which we call pseudoneighbor orbits in Sect. 2.5. Segments of the unstable manifold are classified by how they "wrap around" the holes, i.e. by their homotopy classes. The forward evolution of the holes induces a dynamics on the homotopy classes, which can be expressed in symbolic form. Thus the pseudoneighbor orbits force a certain symbolic representation of the dynamics. This symbolic dynamics in turn yields a lower bound on the topological entropy of the system. For other approaches to the symbolic dynamics of tangles, see Refs. [11–15, 22, 23, 64, 65]. In summary, we explain the topological entropy of the fluid flow in terms of stirring by "ghost rods" attached to heteroclinic orbits. Using this approach, we construct a tight lower bound on the topological entropy for a large interval over which the period-three orbit fails to exist. For τ_f values

for which the period-three orbit does exist, we use heteroclinic orbits to explain some of the excess topological entropy above that predicted by the period-three orbit.

Finally, we note that the topological methods used in this work, specifically the HLD technique, do not require a map defined by a fluid flow nor do they require area-preservation. Our purpose is to explicitly demonstrate how the HLD technique can offer insight into fluid flows and to compare to the results of Grover et. al [33, 69] specifically. More broadly, we wish to draw parallels between our approach and the literature on "stirring" by ghost rods [2, 32, 67, 73, 74].

This paper is organized as follows. Section 2.2 introduces the chaotic cavity flow. Section 2.3 details the direct numerical method of computing topological entropy via the stretching rate Eq. (2.1). Section 2.4 introduces the HLD technique in the context of the period-three orbit, giving us the topological entropy for this orbit. Section 2.5 analyzes the symbolic dynamics of the heteroclinic tangle generated by the period-three orbit. In this manner we compute the topological entropy for heteroclinic orbits that are topologically forced to exist by the period-three orbit, but that persist for τ_f values where the period-three orbit has vanished. These heteroclinic orbits can be viewed as a kind of "remnant" of the period-three orbit. We work out the symbolic dynamics explicitly using longer and longer finite-length intervals of the unstable manifold, thereby including information about more and more complex heteroclinic orbits. These intervals are generated by iterating an initial length of the manifold forward n times. After discussing the cases $n = 1, 2, 3, 4, 5$ in Sects. 2.5.2-2.5.5, we give the general formulation in Sects. 2.5.6-2.5.8. Section 2.6 applies these results to the τ_f values where the period-three orbit does not exist. Section 2.7 uses an automated algorithm to apply the HLD technique to thousands of numerically computed pieces of the unstable manifold, which are chosen to fill in the fluid cavity up to a given area resolution. This symbolic dynamics yields our tightest lower bound on the topological entropy over the range of τ_f studied. Section 2.8 compares our results to the previous work using almost-cyclic sets by Grover et al [33, 69].

2.2 A chaotic time-periodic two-dimensional cavity flow

The chaotic time-periodic lid-driven cavity flow used here was used previously in Refs. [33, 63, 69] to study chaotic advection. It has been physically motivated through studies of the staggered herringbone mixer [70, 71] for low Reynolds numbers, and may find application in the design of microfluidic mixers. The flow is two-dimensional and area preserving, being defined over a 2D vertical cross-section of a rectangular cavity. The cavity cross-section extends vertically from $-b \leq y \leq b$ and horizontally from $0 \leq x \leq a$. The flow does not depend on the second horizontal coordinate z, nor is there a component of the fluid velocity in the z-direction. The two-dimensional flow $\mathbf{u}$ in the xy-plane is thus given by a stream function $\psi(x, y, t)$ according to

$$\mathbf{u}(x, y, t) = \left(\frac{\partial \psi}{\partial y}, -\frac{\partial \psi}{\partial x}\right). \tag{2.2}$$

The specific stream function used in Refs. [33, 63, 69] was derived as the exact solution to the biharmonic equation [51] $\nabla^2 \nabla^2 \psi = 0$ (a consequence of the Stokes-flow assumption) with time-periodic boundary conditions on the top ($y = b$) and bottom ($y = -b$) of the cavity (hence the name "lid-driven"). See Refs. [33, 63, 69] for details of the derivation. The resulting stream function is periodic in time with period τ_f. Over the first half-period, the stream function is constant in time with value

$$\psi(x, y) = U_1 C_1 f_1(y) \sin\left(\frac{\pi x}{a}\right) + U_2 C_2 f_2(y) \sin\left(\frac{2\pi x}{a}\right). \tag{2.3}$$

Over the second half-period, the stream function is again constant in time with value

$$\psi(x, y) = -U_1 C_1 f_1(y) \sin\left(\frac{\pi x}{a}\right) + U_2 C_2 f_2(y) \sin\left(\frac{2\pi x}{a}\right). \tag{2.4}$$

Here

$$\begin{aligned} f_k(y) =& \frac{2\pi y}{a} \cosh\left(\frac{k\pi b}{a}\right) \sinh\left(\frac{k\pi y}{a}\right) \\ & - \frac{2\pi b}{a} \sinh\left(\frac{k\pi b}{a}\right) \cosh\left(\frac{k\pi y}{a}\right), \quad k = 1, 2, \end{aligned} \tag{2.5}$$

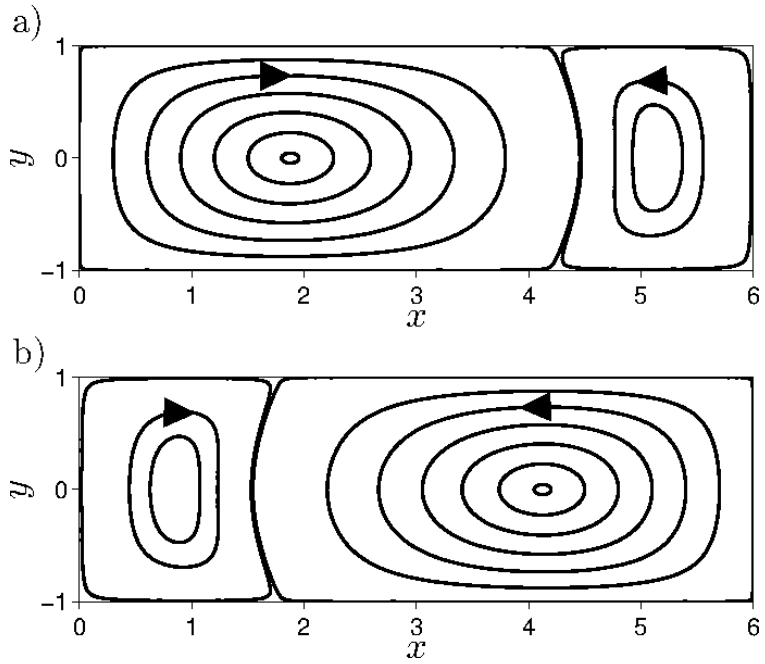

Figure 2.1. Streamlines given by the streamfunctions (a) Eq. (2.3) and (b) Eq. (2.4).

and

$$C_k = \frac{a^2}{2k\pi^2 b}\left[\frac{a}{2k\pi b}\sinh\left(\frac{2k\pi b}{a}\right)+1\right]^{-1}, \quad k=1,2. \tag{2.6}$$

Following Grover et al [33], we use the following constants throughout this paper [1]: $U_1 = 9.9279$, $U_2 = 8.3523$, $a = 6$, $b = 1$. The driving period τ_f is varied in our analysis.

Figure 2.1 shows the streamlines for the two constant flows Eq. (2.3) and (2.4). Each flow is asymmetric in x, with a large vortex on one side and a small vortex on the other. Though each flow is separately integrable, blinking between the two flows introduces chaos. We define M to be the flow map that evolves a point (x, y) forward to the point $(x', y') = M(x, y)$ after one period τ_f.

For $\tau_f \geq \tau_f^* = 0.9553$, M contains a period-three orbit $\boldsymbol{\rho}_i, i = 1, 2, 3$, with nontrivial braiding,

$$M(\boldsymbol{\rho}_1) = \boldsymbol{\rho}_2, \quad M(\boldsymbol{\rho}_2) = \boldsymbol{\rho}_3, \quad M(\boldsymbol{\rho}_3) = \boldsymbol{\rho}_1. \tag{2.7}$$

Following Grover et al [33], we introduce the rescaled period $\bar{\tau}_f = \tau_f/\tau_f^*$, so that the period-three orbit is born at $\bar{\tau}_f = 1$. [2] Figure 2.2a shows the points $\boldsymbol{\rho}_i$ along with their time evolution $\boldsymbol{\rho}_i(t)$

[1] This U_1 value is used for all the results in this paper as well as in [33]; Ref. [33] does not state the correct U_1 value used.

[2] This scaling of τ_f is not explicitly defined in Ref. [33], but was privately communicated to us by the authors.

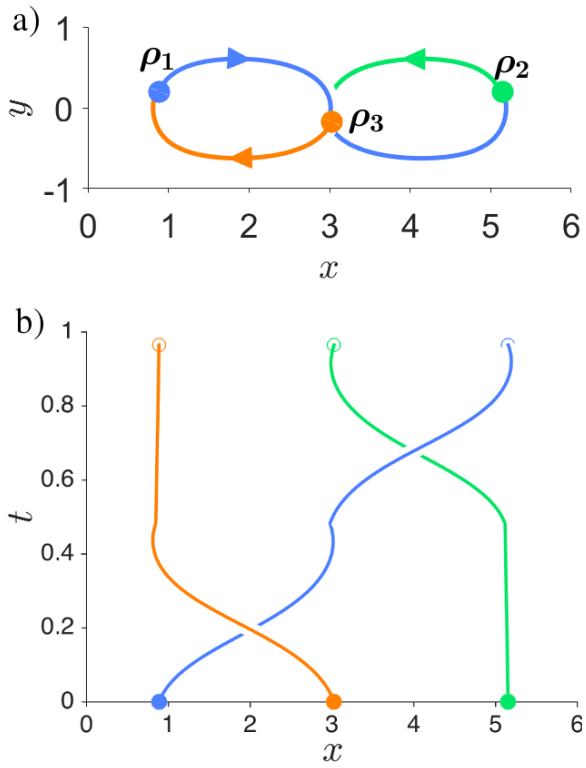

Figure 2.2. Trajectory of the period-three orbit in the model flow viewed in a) the xy space from above the xy plane and b) the xt space.

over one period, i.e. $0 \leq t \leq \tau_f$. Roughly speaking, one can understand the orbit dynamics as follows. In the first half-period, the left two trajectories swap places in a clockwise fashion, and in the second half-period the right two swap places in a counter-clockwise fashion. This can be seen clearly in Fig. 2.2b which shows the trajectories in xt-space. Thinking of the trajectories in the full xyt-space, they can be viewed as a set of three strands braiding around one another and connecting the top ($t = 0$) to the bottom ($t = \tau_f$). The presence of this braid alone in the dynamics implies a lower bound $h_{\text{po3}} = \ln\left(3 + \sqrt{5}\right) = 0.9624$ on the true topological entropy of the fluid flow. This is the perspective adopted in Refs. [6–8], where the topological entropy of the braid is computed using the Bestvina-Handel algorithm [4]. A central question of this paper, as well as of Grover et al. [33, 63, 69], is how to explain the topological entropy when either $\boldsymbol{\rho}_i$ does not exist or when $\boldsymbol{\rho}_i$ does exist but the entropy significantly exceeds h_{po3}.

2.3 Direct computation of the topological entropy via the stretching rate

The topological entropy can be computed directly from Eq. (2.1) using the following method originally proposed by Newhouse et al. [59].

1) Choose an initial material line within the fluid domain. We use the horizontal line extending from $x = \epsilon$, $y = 0$ to $x = 6 - \epsilon$, $y = 0$, with $\epsilon = 10^{-5}$. (The small quantity ϵ is used to avoid any potential numerical error that would cause the material line to exit the cavity.) This choice of initial line was found to adequately intersect the most stretching regions of phase space, leading to small transients and quick exponential growth.

2) Use the flow map M to numerically evolve the initial line forward until transients have decayed and the length $L(t)$ grows exponentially with iterate number. Here, we iterate the initial segment nine times. When evolving the line forward, it is important to infill the line with interpolated points as the point separation becomes too great. We use linear interpolation; though less accurate than higher order schemes, it has the advantage of never placing an interpolated point outside the cavity.

3) Fit an exponential function to the asymptotic growth of $L(t)$ according to Eq. (2.1). Here, the fitting is done using the points from $t = 3$ to $t = 9$. An example of $L(t)$ along with its fitting function is shown in Fig. 2.3.

Although other methods for computing topological entropy numerically exist, for example, constructing a Markov chain using finite partitions [27]. We have chosen the method described above because it is the more familiar method for 2D flows, and was used previously for this same flow by Grover et. al [33, 69].

Figure 2.4 shows the direct stretching computation of topological entropy h for $\bar{\tau}_f$ in the range $[0.8374, 1.099]$. An alternative way to compute topological entropy numerically is by approximating the symbolic dynamics using finite partitions [27].

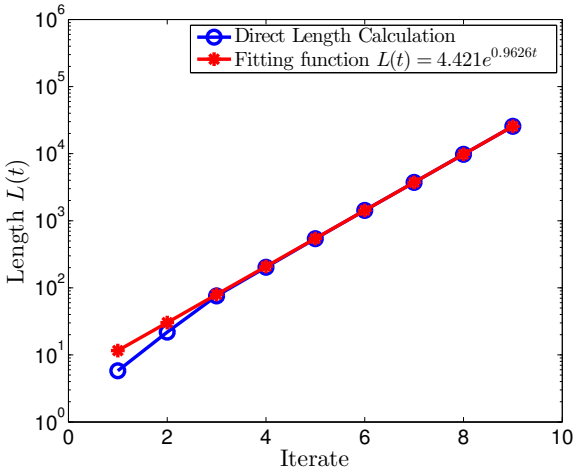

Figure 2.3. The length of an advected material line as a function of iterate, along with the corresponding fitting function for $\bar{\tau}_f = 0.9945$. The topological entropy computed from this fit is 0.9626 ± 0.0008.

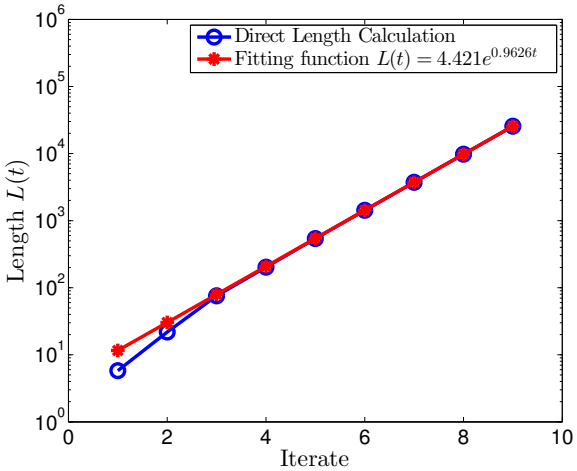

Figure 2.4. The direct computation of topological entropy as a function of driving period. Error bounds are 95% confidence intervals computed from the exponential fit. The period-three orbit exists for values of $\bar{\tau}_f$ greater than 1, i.e. right of the green vertical line. The horizontal black line marks the topological entropy $h_{\text{po3}} = \ln\left(3 + \sqrt{5}\right) = 0.9624$ of the period-three orbit.

2.4 A tangle analysis of the topological dynamics generated by the period-three orbit

This section derives the symbolic dynamics and computes the topological entropy generated by the period-three orbit, using the homotopic lobe dynamics technique [53, 54]. Previously, it has been common to use the Bestvina-Handel algorithm to compute the topological entropy of the period-three orbit. [4, 8, 32]. The HLD technique requires a tangle as its starting point. We choose the heteroclinic tangle attached to the two hyperbolic fixed points $\mathbf{z}_u$ and $\mathbf{z}_\ell$ that lie on the upper and lower boundaries of the fluid domain, respectively, Fig. 2.5. The stable and unstable manifolds are computed using an algorithm similar to Yorke et. al [76]. The initial segment is chosen as a small line along the eigenvector of the fixed point, and it is iterated forward by integrating the flow map M along the respective points. In order to maintain accuracy while exponentially growing the manifold, interpolated points are inserted at each iterate to maintain sufficient density. The unstable manifold $W^U_{\mathbf{z}_u}$ lies within the fluid domain and is attached to the upper fixed point $\mathbf{z}_u$; the stable manifolds of $\mathbf{z}_u$ lie on the fluid boundary and do not concern us. Similarly, the stable manifold $W^S_{\mathbf{z}_\ell}$ lies within the fluid domain and is attached to the lower fixed point $\mathbf{z}_\ell$; again, we are not concerned with the unstable manifold of $\mathbf{z}_\ell$ on the fluid boundary. Points on the unstable manifold $W^U_{\mathbf{z}_u}$ map away from $\mathbf{z}_u$, while points on the stable manifold $W^S_{\mathbf{z}_\ell}$ map toward $\mathbf{z}_\ell$. This dynamical direction is denoted by a triangular arrow in Fig. 2.5 (in contrast to the barbed arrows used below for the homotopy direction.) The stable and unstable manifolds $W^S_{\mathbf{z}_\ell}$ and $W^U_{\mathbf{z}_u}$ intersect at a primary intersection point (pip) $\mathbf{p}_0$; a pip $\mathbf{p}_0$ is an intersection point such that $W^S_{\mathbf{z}_\ell}[\mathbf{z}_\ell, \mathbf{p}_0) \cap W^U_{\mathbf{z}_u}[\mathbf{z}_u, \mathbf{p}_0) = \emptyset$ [22, 23]. Note that the pip $\mathbf{q}_0$, or any iterate of $\mathbf{p}_0$ or $\mathbf{q}_0$ could in principle also be used.

Figure 2.5a shows the (infinitely-long) stable manifold $W^S_{\mathbf{z}_\ell}$ only up to the pip $\mathbf{p}_0$, but shows the (infinitely-long) unstable manifold $W^U_{\mathbf{z}_u}$ beyond the $\mathbf{p}_0$ intersection. The unstable manifold has several oscillations that quickly press against the lower fluid boundary, making it hard to visualize the manifold topology. It is helpful, therefore, to view the manifolds in the transformed log-coordinates

$$u = \ln(x) - \ln(6 - x), \tag{2.8a}$$

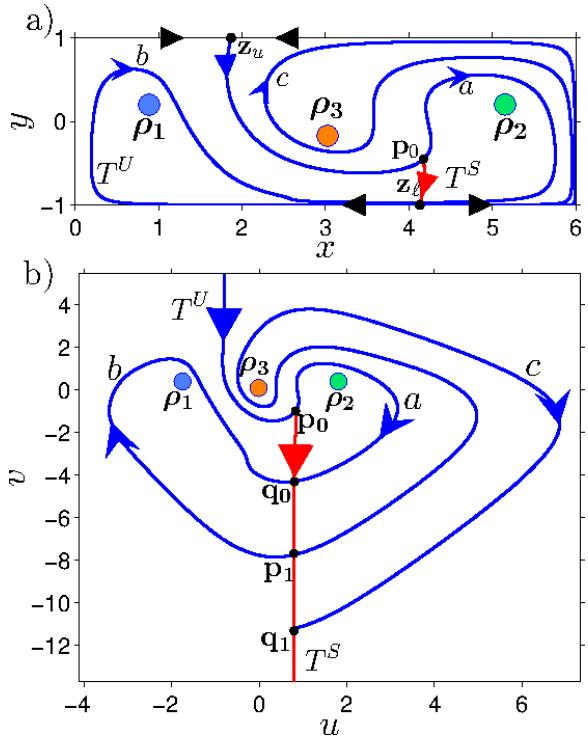

Figure 2.5. Computation of the trellis for $\bar{\tau}_f = 1.057$. The stable and unstable manifolds $W^S_{\mathbf{z}_\ell}$ and $W^U_{\mathbf{z}_u}$ are computed long enough to identify the three bridge classes a, b, and c defined by the period-three orbit. a) Trellis in the original rectangular co-ordinates. b) Trellis in the log co-ordinates defined by Eqs. (2.8).

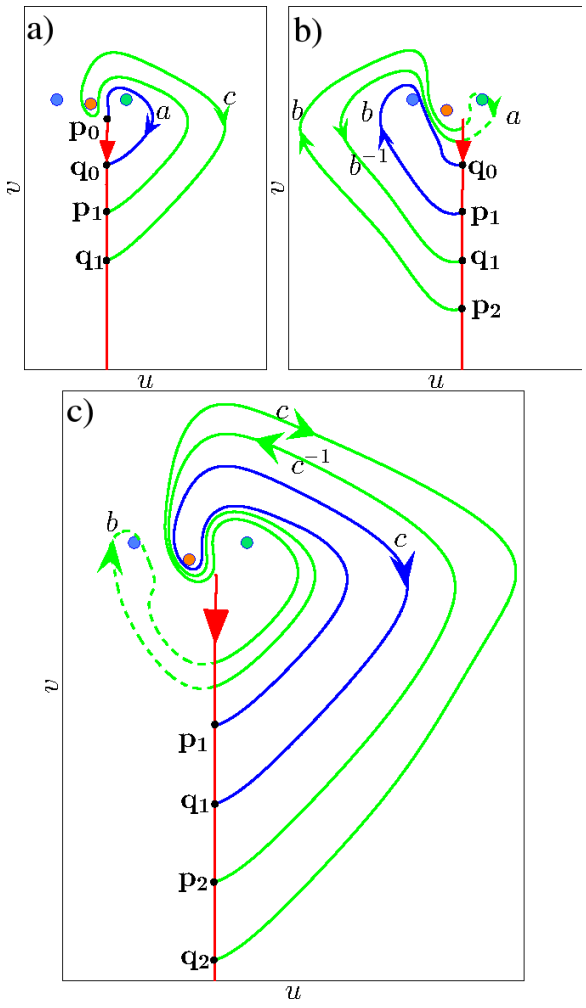

Figure 2.6. The iterates (in green) of the bridge classes a, b, and c (in blue) for $\bar{\tau}_f = 1.057$ in the log space. The decomposition of each iterate into bridge classes is also shown.

$$v = \ln(y+1) - \ln(1-y). \tag{2.8b}$$

These coordinates map the boundary of the fluid domain to infinity and spread the manifold oscillations apart, as shown in Fig. 2.5b. This figure shows that $W^U_{\mathbf{z}_u}$ is plotted up to point $\mathbf{q}_1 = M(\mathbf{q}_0)$, where $\mathbf{q}_0$ is the pip between $\mathbf{p}_0$ and $\mathbf{p}_1 = M(\mathbf{p}_0)$. In general, we use the notation that for any heteroclinic orbit $\mathbf{x}_i$, i records its iterate, i.e. $\mathbf{x}_{i+1} = M(\mathbf{x}_i)$.

A *bridge* is a segment of $W^U_{\mathbf{z}_u}$ that begins and ends on the stable segment $W^S_{\mathbf{z}_\ell}[\mathbf{z}_\ell, \mathbf{p}_0]$ without otherwise intersecting this stable segment. In order to obtain the symbolic dynamics of the period-three orbit, we classify bridges by how they wind around the period-three points, or "stirring rods", $\boldsymbol{\rho}_1$, $\boldsymbol{\rho}_2$, and $\boldsymbol{\rho}_3$. As shown in Fig. 2.5b, a bridge of class a winds clockwise around rod $\boldsymbol{\rho}_2$, a bridge of class b winds clockwise around rod $\boldsymbol{\rho}_3$, and a bridge of class c winds clockwise around rod $\boldsymbol{\rho}_1$. Mathematically, we punch "holes" in the plane at the periodic points $\boldsymbol{\rho}_1$, $\boldsymbol{\rho}_2$, and $\boldsymbol{\rho}_3$, and view a, b, and c as the homotopy classes of bridges relative to the starting and ending segment $W^S_{\mathbf{z}_\ell}[\mathbf{z}_\ell, \mathbf{p}_0]$. We shall consider the periodic points as holes or rods interchangeably, depending on context. In general, the homotopy class of a path P, with endpoints on $W^S_{\mathbf{z}_\ell}[\mathbf{z}_\ell, \mathbf{p}_0]$, consists of all those paths that can be continuously distorted from P without passing through a hole and without the endpoints leaving $W^S_{\mathbf{z}_\ell}[\mathbf{z}_\ell, \mathbf{p}_0]$. The homotopy classes a, b, and c are special because they are the classes of bridges; we call a, b, and c *bridge classes*. The direction of a bridge class is denoted by a barbed arrow on the unstable manifold (Fig. 2.5), in contrast to the dynamical direction denoted by an unbarbed (triangular) arrow. Note that the HLD analysis in this section differs in one crucial respect from the development of HLD in Refs. [53, 54]; in these references holes were punched along heteroclinic orbits (See Sect. 2.5B-2.5H) rather than periodic orbits.

Physically, as the rods undergo one stirring period, the bridges within each class are stretched and folded, becoming new segments of the unstable manifold. These new segments are typically not bridges, but since they still begin and end on $W^S_{\mathbf{z}_\ell}[\mathbf{z}_\ell, \mathbf{p}_0]$, each can be decomposed into a concatenation of bridges. At the level of homotopy, the homotopy class of such a new segment can be decomposed into a *product* of bridge classes. Figure 2.6 shows representative bridges from each of the three bridge classes and their iterates. The decomposition of each iterate into bridge classes is also shown, yielding the bridge dynamics

$$M(a) = c, \tag{2.9a}$$

$$M(b) = bab^{-1}, \tag{2.9b}$$

$$M(c) = c^{-1}bc. \tag{2.9c}$$

The topology of the iterates shown in Fig. 2.6 can be determined either from a direct numerical computation of the iterates, as shown, or from just the bridges shown in Fig. 2.5b together with Eq. (2.7). Following the latter approach, the topology of $M(b)$ in Fig. 2.6b, for example, can be determined from the following "game". Draw a curve from point $\mathbf{p}_2$ to point $\mathbf{q}_1$ (since there is a curve of class b connecting $\mathbf{p}_1$ to $\mathbf{q}_0$) such that it does not self-intersect or intersect any other unstable segment in Fig. 2.5b and such that it wraps clockwise once around hole $\boldsymbol{\rho}_3$ (since b wraps clockwise once around hole $\boldsymbol{\rho}_1$.) It is straightforward to see that the solution curve has the unique homotopy class given by Eq. (2.9b). The reader is invited to play this game for classes a and c as well.

We define the transition matrix T as the matrix whose component T_{ij} records the number of times bridge class s_i, or its inverse s_i^{-1}, appears in the iterate of bridge class s_j, where $s_i, s_j \in \{a, b, c\}$. Equations (2.9) imply

$$\mathsf{T} = \begin{array}{c} \\ a \\ b \\ c \end{array} \begin{array}{c} \begin{array}{ccc} a & b & c \end{array} \\ \begin{bmatrix} 0 & 1 & 0 \\ 0 & 2 & 1 \\ 1 & 0 & 2 \end{bmatrix} \end{array}. \tag{2.10}$$

The log of the largest eigenvalue of T is the topological entropy of the symbolic dynamics Eqs. (2.9), or equivalently of the period-three orbit $\boldsymbol{\rho}_i$.

$$h_{\mathrm{po3}} = \ln\left(3+\sqrt{5}\right) = 0.9624. \tag{2.11}$$

This is the same as the topological entropy of the period-three braid computed from the Bestvina-Handel algorithm [4]. It is a lower bound to the topological entropy of the fluid flow M for any parameter value τ_f in which the period-three orbit exists.

2.5 A tangle analysis of the topological dynamics generated by heteroclinic orbits

As seen in Fig. 2.4, the period-three orbit $\boldsymbol{\rho}_i$ fails to exist below $\bar{\tau}_f = 1$. [3] How then are we to understand the origin of the topological entropy in this case? How can we place a lower bound on the topological entropy of the fluid flow? One possibility derives from the fact that the hyperbolic fixed points $\mathbf{z}_u$ and $\mathbf{z}_\ell$, and their associated stable and unstable manifolds, persist down to $\bar{\tau}_f = 0$. This can be shown by noticing that both stream functions Eq. (2.3) and Eq. (2.4) have four hyperbolic fixed points at the corners of the rectangular domain. Any dynamics generated by the switching between the two stream functions must also have the same fixed points with the same stable and unstable directions. For example, the top left fixed point has an unstable direction pointing to the right and the top right fixed point has an unstable direction pointing to the left. (See Fig. 2.1.) It is then necessary that a fixed point $\mathbf{z}_u$ lies between these two points with its *stable* direction along the boundary, and an unstable direction pointing downward into the domain. Similarly, for all $\bar{\tau}_f$ there must exist a fixed point $\mathbf{z}_\ell$ on the bottom boundary with a stable direction pointing upward into the domain.

As with periodic orbits, the heteroclinic intersections between the stable and unstable manifolds attached to $\mathbf{z}_\ell$ and $\mathbf{z}_u$, respectively, also generate topological entropy [11–15,53,54]. In this section, we compute the topological entropy forced by heteroclinic intersections arising from the dynamics

[3] Other period-three orbits exist below $\bar{\tau}_f = 1$; for example, two period-three orbits persist on the right side and two period-three orbits persist on the left side. However, these orbits have smaller topological entropy.

in Eq. (2.9). More precisely, we consider finite-length pieces of the unstable manifold forced by the dynamics of Eq. (2.9). These pieces have the fewest intersections consistent with Eq. (2.9), i.e. there are no additional unforced intersections. We then forget about the period-three orbit $\boldsymbol{\rho}_i$ itself and compute symbolic dynamics based solely on the finite-length pieces and their intersections with the stable manifold. The resulting topological entropy will be less than that of the period-three orbit. The period-three topological entropy is only recovered in the limit of using infinitely long pieces of unstable manifold. Finally, we are not trying to exactly reproduce the trellis for a particular $\bar{\tau}_f$ value. We are constructing a trellis with minimal complexity consistent with the presence of the period-three orbit.

We examine the development of the tangle by iterating the *fundamental segment* $U_0 = W^U[\mathbf{p}_{-1}, \mathbf{p}_0]$ forward n times. We go up to $n = 5$ because this is sufficient to illustrate the general pattern, which we then work out explicitly for the cases $n = 3k - 1$, $3k$, and $3k + 1$. Progressing through the cases $n = 1$ to $n = 5$ also allows us to review the HLD technique through a series of examples of increasing complexity. The particular analysis in Sects. 2.5.1- 2.5.8 applies in general when you have the period-three braid applied to a phase space exhibiting topology in Fig. 2.7. The following sections rely heavily on the HLD technique; for complete details on the HLD technique see Refs. [53, 54].

2.5.1 The development of the trellis at $n = 1$

At $n = 1$, the unstable manifold is computed up to $\mathbf{p}_1$ as shown in Fig. 2.7. This segment is the union of the segment $W^U[\mathbf{z}_u, \mathbf{p}_0]$, connecting the fixed point (not shown) to the pip, with the segment $U_1 = M(U_0) = W^U[\mathbf{p}_0, \mathbf{p}_1]$. We use the term *trellis* for the finite intervals of the stable and unstable manifolds that are computed and used for our topological analysis. The unstable and stable components of the trellis T_n are denoted T_n^U and T^S, respectively. (The stable component T^S will not change with n.) At $n = 1$, $T_1^U = W^U[\mathbf{z}_u, \mathbf{p}_1]$ and $T^S = W^S[\mathbf{z}_\ell, \mathbf{p}_0]$. The unstable trellis T_1^U contains two bridges, $W^U[\mathbf{p}_0, \mathbf{q}_0]$ and $W^U[\mathbf{q}_0, \mathbf{p}_1]$. By a classic result of Smale [66], the transverse intersections $\mathbf{p}_0$ and $\mathbf{q}_0$ seen in the trellis guarantee a nonzero topological entropy for the map M. This is because each of the two bridges will eventually develop additional intersections with T^S when they are iterated forward, ultimately resulting in an exponential explosion of intersections,

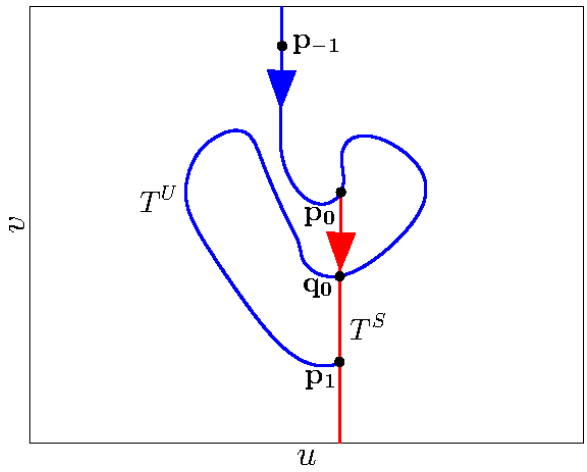

Figure 2.7. The trellis at $n = 1$ in the log space.

with the topological entropy being the growth rate of the intersections. However, the trellis itself does not contain enough information to determine how many iterates it will take to develop additional intersections or what the corresponding growth rate will be. As a consequence, the trellis at $n = 1$ yields a lower bound of zero on the topological entropy of the fluid flow M.

2.5.2 The development of the trellis at $n = 2$

At $n = 2$, the trellis now includes the second iterate U_2 of the fundamental segment. In order to determine the structure of the trellis at $n = 2$, we apply the dynamics of Eqs. (2.9) to the two segments $W^U[\mathbf{q}_0, \mathbf{p}_0]$ and $W^U[\mathbf{p}_1, \mathbf{q}_0]$ from the trellis at $n = 1$. The left segment $W^U[\mathbf{p}_1, \mathbf{q}_0]$ is a curve of class b in Fig. 2.5, and thus maps forward to a curve of class bab^{-1} according to Eq. (2.9b) and shown in Fig. 2.6b. Therefore, the curve $W^U[\mathbf{p}_2, \mathbf{q}_1]$ has the structure shown in Fig. 2.8, with two new secondary intersections $\mathbf{r}_0$ and $\mathbf{s}_0$ with T^S. Likewise, the right segment $W^U[\mathbf{q}_0, \mathbf{p}_0]$ from the trellis at $n = 1$ is a curve of class a in Fig. 2.5, and thus maps forward to a curve of class c according to Eq. (2.9a) and shown in Fig. 2.6a. Therefore, $W^U[\mathbf{q}_1, \mathbf{p}_1]$ has no additional intersections with T^S beyond its endpoints. We have thus determined the structure of the trellis $T_2^U = W^U[\mathbf{z}_u, \mathbf{p}_2]$ shown in Fig. 2.8. The stable trellis T^S is the same as $n = 1$. The new intersections $\mathbf{r}_0$ and $\mathbf{s}_0$ yield a nonzero lower bound on the topological entropy of M, as we now show.

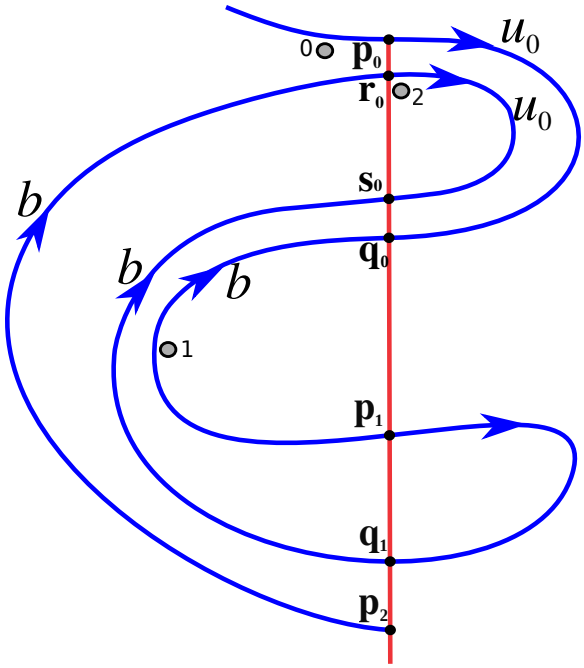

Figure 2.8. Development of the trellis at $n = 2$, drawn schematically rather than computed numerically to better visualize the topology. Arrows represent the direction of the bridge classes.

We outline here the homotopic lobe dynamics technique applied to the trellis T_2 in Fig. 2.8. We first construct the set X, which for general n contains all trellis intersections $T_n^U \cap T^S$ iterated forward and backward any number of times,

$$X = \{M^k(\mathbf{x}) \mid \forall \mathbf{x} \in T_n^U \cap T^S, \forall k \in \mathbb{Z}\}. \tag{2.12}$$

Figure 2.8 shows that, for $n = 2$, X is obtained by iterating the four points $\mathbf{p}_0$, $\mathbf{q}_0$, $\mathbf{r}_0$, and $\mathbf{s}_0$ forward and backward,

$$X = \{\mathbf{p}_k, \mathbf{q}_k, \mathbf{r}_k, \mathbf{s}_k \mid \forall k \in \mathbb{Z}\}. \tag{2.13}$$

We next determine the pseudoneighbors of the trellis. Two points $\mathbf{x}, \mathbf{x}' \in X$ are said to form a *pair of pseudoneighbors* if there are no elements of X on either $W^U(\mathbf{x}, \mathbf{x}')$ or $W^S(\mathbf{x}, \mathbf{x}')$. In Fig. 2.8, $\mathbf{r}_0$ and $\mathbf{s}_0$ are a pair of pseudoneighbors, as are any iterates $\mathbf{r}_k$ and $\mathbf{s}_k$. Note that $\mathbf{p}_1$ and $\mathbf{q}_1$ do not form a pair of pseudoneighbors; even though there are no trellis intersections on the intervals $W^U(\mathbf{p}_1, \mathbf{q}_1)$ or $W^S(\mathbf{p}_1, \mathbf{q}_1)$, the points $\mathbf{r}_1, \mathbf{s}_1 \in X$ lie on the interval $W^S(\mathbf{p}_1, \mathbf{q}_1)$. Similarly, $\mathbf{q}_0$ and $\mathbf{p}_1$ do not form a pair of pseudoneighbors since $\mathbf{r}_{-1}, \mathbf{s}_{-1} \in X$ lie on the interval $W^U(\mathbf{q}_0, \mathbf{p}_1)$. Thus, $\mathbf{r}_k$ and $\mathbf{s}_k$ form the only pair of pseudoneighbor *trajectories* for T_2.

In Sect. 2.4, we punched holes at each point of the period-three orbit $\boldsymbol{\rho}_i$. For the trellis T_n we instead punch holes adjacent to *heteroclinic* orbits. Specifically, for T_2 we punch one hole for each pair of pseudoneighbors $\mathbf{r}_k$ and $\mathbf{s}_k$. This hole is placed within the region bounded by $W^U[\mathbf{r}_k, \mathbf{s}_k]$ and $W^S[\mathbf{r}_k, \mathbf{s}_k]$, and infinitesimally close to either $\mathbf{r}_k$ or $\mathbf{s}_k$; here, we choose $\mathbf{r}_k$. Specifically, Fig. 2.8 shows a hole (denoted by a shaded circle) adjacent to $\mathbf{r}_0$ and within the D-shaped region bounded by $W^U[\mathbf{r}_0, \mathbf{s}_0]$ and $W^S[\mathbf{r}_0, \mathbf{s}_0]$. In Fig. 2.8, we only plot the holes up to hole number 2, which is the first hole to lie adjacent to T^S. Note that an infinite number of holes actually line the right side of T^S, converging upon $\mathbf{z}_\ell$ in the forward time direction. (In the uv-coordinates of Fig. 2.8, these holes progress infinitely far downward.) Mapping hole 2 backward, it lies adjacent to the point $\mathbf{r}_{-1}$. The point r_{-1} is not explicitly shown in Fig. 2.8, but it must lie on the bridge $W^U[\mathbf{q}_0, \mathbf{p}_1]$. Furthermore, hole 0 lies adjacent to point $\mathbf{r}_{-2}$, which lies on $W^U[\mathbf{z}_u, \mathbf{p}_0]$. Similarly, an infinite number of holes lie adjacent to $W^U[\mathbf{z}_u, \mathbf{p}_0]$, converging upon $\mathbf{z}_u$ in the backward time direction (and progressing infinitely far upward in Fig. 2.8.) However, in Fig. 2.8, we only plot the holes back to hole number 0, which is the first to lie adjacent to $W^U[\mathbf{z}_u, \mathbf{p}_0]$.

Note in Sect. 2.4 the holes were punched at exactly the period-three points $\boldsymbol{\rho}_i$. Here, however, the holes are infinitesimal perturbations from the heteroclinic points $\mathbf{r}_k$. Thus, we must use a separate notation and separate labels for the holes than we use for the heteroclinic points.

The homotopy class of a bridge is now defined relative to the holes punched here, rather than holes on the period-three orbit $\boldsymbol{\rho}_i$. On the left side of T_S in Fig. 2.8, there is a single bridge class b, which by convention winds clockwise around hole 1. The symbol b is used for this bridge class because b was used previously for the bridge class of $W^U[\mathbf{p}_1, \mathbf{q}_0]$ in Fig. 2.5. On the right side, there is an infinite sequence of bridge classes u_k, $k \geq 0$, where u_k winds clockwise around hole $2 + k$.

We next determine the dynamics on the bridge classes. Figure 2.8 shows that the bridge $W^U[\mathbf{p}_1, \mathbf{q}_0]$ is of class b and maps forward to $W^U[\mathbf{p}_2, \mathbf{q}_1] = W^U[\mathbf{p}_2, \mathbf{r}_0] \cup W^U[\mathbf{r}_0, \mathbf{s}_0] \cup W^U[\mathbf{s}_0, \mathbf{q}_1]$, whose homotopy class is bu_0b^{-1}. Thus,

$$M(b) = bu_0b^{-1}. \tag{2.14}$$

Refs. [53, 54] emphasize that the bridge dynamics should be represented by a *concise* product of bridge classes. In the present case, a concise product is one in which the bridge classes alternate between being on the left and right sides of T^S. Since b is on the left and u_0 is on the right, Eq. (2.14) is indeed concise.

Next, Figure 2.8 shows that $W^U[\mathbf{p}_0, \mathbf{q}_0]$ is a bridge of class u_0 that maps forward to $W^U[\mathbf{p}_1, \mathbf{q}_1]$, which is of class u_1. More generally,

$$M(u_k) = u_{k+1}. \tag{2.15}$$

All the classes u_k are said to be *inert* because the forward iterate of any one of them never generates more than one bridge class, no matter how many times it is iterated; we call u_0 the *primary* inert class. On the other hand b is said to be *active* because its forward iterate is the product of three bridge classes. We will always denote active classes by a, b, and c, and inert classes by u and v. We will also denote *types* of bridge classes by an index such as u_k, which represents the set of inert bridge classes of type u.

The dynamics of the inert classes contribute nothing to the topological entropy. Thus, we restrict the transition matrix T to the active classes. Since the present case has only a single active class b

that maps to two copies of itself, we find

$$\mathsf{T} = [2]. \tag{2.16}$$

The topological entropy of the trellis T_2, i.e. of Eq. (2.14), thus equals

$$h_2 = \ln 2 = 0.6931. \tag{2.17}$$

This topological entropy is a lower bound for the topological entropy of the fluid flow M. Note that $h_2 = 0.6931$ is less than the entropy $h_{\text{po3}} = 0.9624$ of the period-three orbit $\boldsymbol{\rho}_i$ itself, as it must be, since T_2 is only part of the full tangle generated by $\boldsymbol{\rho}_i$.

2.5.3 The development of the trellis at $n = 3$

If we followed the pattern established in Sects. 2.5.1 and 2.5.2 at $n = 3$, the trellis T_3 would include the third iterate $U_3 = M^3(U_0)$ of the fundamental segment $U_0 = W^U[\mathbf{p}_{-1}, \mathbf{p}_0]$. However, U_3 contains so many new bridges (ten) that the figure of the trellis would become crowded and hard to visually analyze. More importantly, the majority of these new bridges result from the topological constraints already established by T_2 and provide no new topological information. Specifically, U_2 in Fig. 2.8 contains the two bridges $W^U[\mathbf{q}_1, \mathbf{s}_0]$ and $W^U[\mathbf{p}_2, \mathbf{r}_0]$ of class b, and these bridges map forward into three new bridges each, exactly as predicted by Eq. (2.14). On the other hand, U_2 also contains the two inert bridges (i.e. bridges with an inert class) $W^U[\mathbf{r}_0, \mathbf{s}_0]$ and $W^U[\mathbf{p}_1, \mathbf{q}_1]$. Though the iterates of these bridges are not forced by the topology of T_2 to produce any new intersections, they do in fact produce new intersections when analyzed in the context of Fig. 2.5 and Eqs. (2.9). Thus, we construct the trellis T_3 by adding to T_2 those bridges (and only those bridges) that result from mapping forward the inert bridges in U_2. This is how we shall proceed from now on, i.e. T^U_{n+1} will be the union of T^U_n and the forward iterate of the inert bridges from $T^U_n \cap U_n$. Mapping forward the inert bridges $W^U[\mathbf{r}_0, \mathbf{s}_0]$ and $W^U[\mathbf{p}_1, \mathbf{q}_1]$ in T_2, we include $W^U[\mathbf{r}_1, \mathbf{s}_1]$ and $W^U[\mathbf{p}_2, \mathbf{q}_2]$ in T^U_3. The segment $W^U[\mathbf{r}_0, \mathbf{s}_0]$ in T^U_2 is a curve of class a in Fig. 2.5, which maps forward to a curve of class c according to Eqs. (2.9). Thus $W^U[\mathbf{r}_1, \mathbf{s}_1]$ shown in Fig. 2.9 contains no new intersections in T^U_3. Similarly, the segment $W^U[\mathbf{p}_1, \mathbf{q}_1]$ in T^U_2 is a curve of class c in Fig. 2.5, which maps

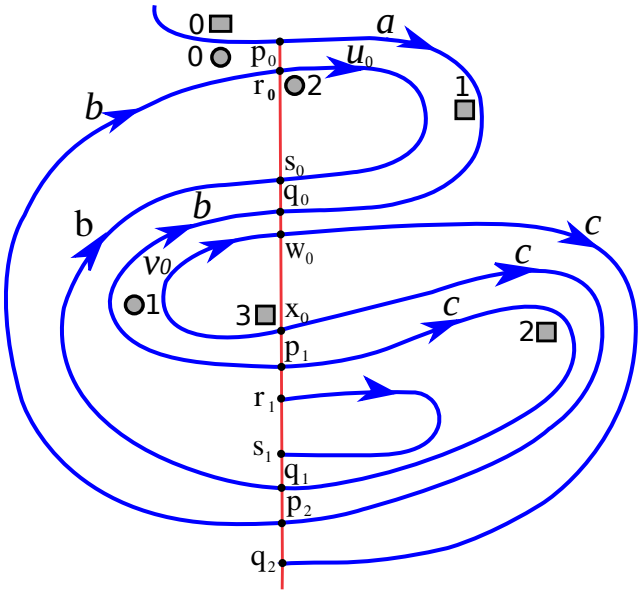

Figure 2.9. Schematic illustration of the development of the trellis at $n = 3$.

forward to a curve of class $c^{-1}bc$ according to Eqs. (2.9). Thus, $W^U[\mathbf{p}_2, \mathbf{q}_2]$ contains the two new heteroclinic intersections $\mathbf{w}_0$ and $\mathbf{x}_0$ in T_3^U, as shown in Fig. 2.9.

To carry out the HLD technique, we next construct the set X from Eq. (2.12),

$$X = \{\mathbf{p}_k, \mathbf{q}_k, \mathbf{r}_k, \mathbf{s}_k, \mathbf{w}_k, \mathbf{x}_k \mid \forall k \in \mathbb{Z}\}. \tag{2.18}$$

As for T_2, $\mathbf{r}_k$ and $\mathbf{s}_k$ form a pair of pseudoneighbors, but now $\mathbf{w}_k$ and $\mathbf{x}_k$ form a new pair of pseudoneighbors, as can be easily checked with Fig. 2.9. We again punch a hole for each pair of pseudoneighbors, with a hole (denoted by a circle) in the region bounded by $W^U[\mathbf{r}_k, \mathbf{s}_k]$ and $W^S[\mathbf{r}_k, \mathbf{s}_k]$ as well as a hole (denoted by a square) in the region bounded by $W^U[\mathbf{w}_k, \mathbf{x}_k]$ and $W^S[\mathbf{w}_k, \mathbf{x}_k]$. As in Fig. 2.8, Fig. 2.9 shows the backward iterates of the holes only until they first land adjacent to $W^U[\mathbf{z}_u, \mathbf{p}_0]$; these holes are numbered 0. Similarly, Fig. 2.9 shows the forward iterates of these holes only up to the first ones to lie adjacent to T^S. Recall, however, that there are an infinite number of holes adjacent to T^S, converging upon $\mathbf{z}_\ell$. These holes create some technical subtleties in analyzing the bridge dynamics, as discussed in Ref. [53, 54]. For the practical purpose of determining the active bridge dynamics, however, we may ignore all holes after those that first lie adjacent to T^S, as shown in Fig. 2.9.

We proceed now to identify all bridge classes in Fig. 2.9. There are three active classes: a, which encloses circle-hole 2 and square-hole 1 clockwise; b, which encloses circle-hole 1 and square-hole 3 clockwise; and c, which encloses circle-hole 3 and square-hole 2 clockwise. There are two primary inert classes, u_0, encircling circle-hole 2, and v_0, encircling square-hole 3. The choice of symbols a, b, and c is consistent with the labels in Fig. 2.5.

To determine how the active classes map forward, we investigate how a representative bridge in T^U from each class maps forward.

$$T^U[\mathbf{p}_0, \mathbf{q}_0] \mapsto T^U[\mathbf{p}_1, \mathbf{q}_1], \tag{2.19a}$$

$$T^U[\mathbf{p}_1, \mathbf{q}_0] \mapsto T^U[\mathbf{p}_2, \mathbf{r}_0] \cup T^U[\mathbf{r}_0, \mathbf{s}_0] \cup T^U[\mathbf{s}_0, \mathbf{q}_1], \tag{2.19b}$$

$$T^U[\mathbf{p}_1, \mathbf{q}_1] \mapsto T^U[\mathbf{p}_2, \mathbf{x}_0] \cup T^U[\mathbf{x}_0, \mathbf{w}_0] \cup T^U[\mathbf{w}_0, \mathbf{q}_2]. \tag{2.19c}$$

Replacing each bridge in the above by its bridge class, we obtain

$$M(a) = c, \tag{2.20a}$$

$$M(b) = bu_0b^{-1}, \tag{2.20b}$$

$$M(c) = cv_0c^{-1}. \tag{2.20c}$$

Note that the class a is not *recurrent*, i.e. mapping a forward an arbitrary number of times never produces another copy of a. Thus a is a transient symbol and has no bearing on the topological entropy of the bridge dynamics. The transition matrix for the remaining two active classes b and c is then

$$\mathsf{T} = \begin{array}{c} \\ b \\ c \end{array} \begin{array}{c} \begin{array}{cc} b & c \end{array} \\ \begin{bmatrix} 2 & 0 \\ 0 & 2 \end{bmatrix} \end{array}. \tag{2.21}$$

T is diagonal because b only produces additional copies of b, and c only produces additional copies of c. Hence, for T_3 there is no mixing between symbols on the left- and right-hand sides of T^S. The

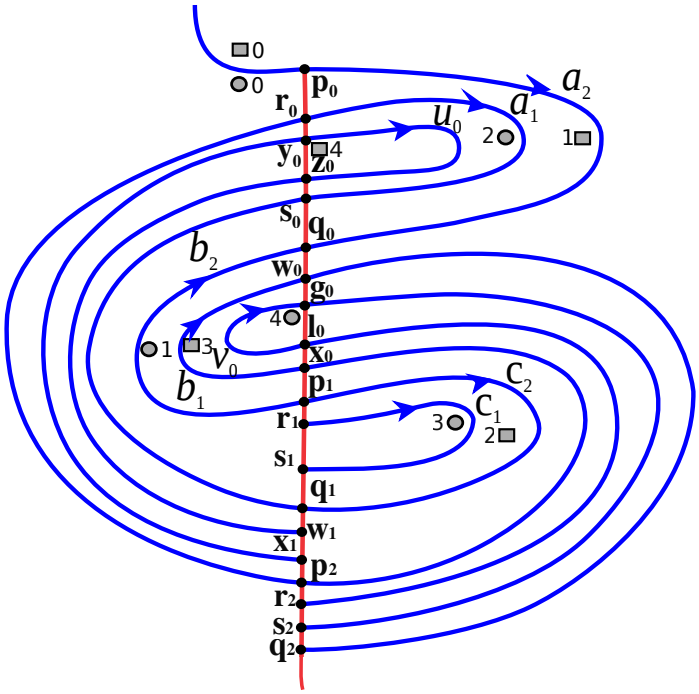

Figure 2.10. Schematic illustration of the development of the trellis at $n = 4$.

topological entropy of T_3 is clearly

$$h_3 = \ln 2 = 0.6931, \tag{2.22}$$

which is the same as h_2 for T_2.

2.5.4 The development of the trellis at $n = 4$

To construct T_4, we take the union of T_3 with the iterate of the inert bridges in $T_3 \cap U_3$, namely $T^U[\mathbf{r}_1, \mathbf{s}_1]$ and $T^U[\mathbf{x}_0, \mathbf{w}_0]$, which iterate forward to the segments $T^U[\mathbf{r}_2, \mathbf{s}_2]$ and $T^U[\mathbf{x}_1, \mathbf{w}_1]$ in Fig. 2.10. The segment $W^U[\mathbf{r}_1, \mathbf{s}_1]$ in T_3^U is a curve of class c in Fig. 2.5, which maps forward to a curve of class $c^{-1}bc$ according to Eqs. (2.9). Thus $W^U[\mathbf{r}_2, \mathbf{s}_2]$ shown in Fig. 2.10 contains one new pair of intersections in T_4^U, namely $(\mathbf{g}_0, \ell_0)$. Similarly, the segment $W^U[\mathbf{x}_0, \mathbf{w}_0]$ in T_3^U is a curve of class b in Fig. 2.5, which maps forward to a curve of class bab^{-1} according to Eqs. (2.9). Thus, $W^U[\mathbf{x}_1, \mathbf{w}_1]$ also contains one new pair of heteroclinic intersections $(\mathbf{y}_0, \mathbf{z}_0)$ in T_4^U, as shown in Fig. 2.10.

To carry out the HLD technique, we again construct the set X from Eq. (2.12),

$$X = \{\mathbf{p}_k, \mathbf{q}_k, \mathbf{r}_k, \mathbf{s}_k, \mathbf{w}_k, \mathbf{x}_k, \mathbf{y}_k, \mathbf{z}_k, \mathbf{g}_k, \boldsymbol{\ell}_k \mid \forall k \in \mathbb{Z}\}. \tag{2.23}$$

In Fig. 2.10, $\mathbf{y}_0$ and $\mathbf{z}_0$ are a pair of pseudoneighbors because none of the intersections in X lie on $W^S(\mathbf{y}_0, \mathbf{z}_0)$ or $W^U(\mathbf{y}_0, \mathbf{z}_0)$. Likewise, $\mathbf{g}_0$ and $\boldsymbol{\ell}_0$ are a pair of pseudoneighbors, and $(\mathbf{y}_k,\ \mathbf{z}_k)$ and $(\mathbf{g}_k,\ \boldsymbol{\ell}_k)$ are the only pairs of pseudoneighbor trajectories for T_4. Note that the number of pseudoneighbor trajectories (and hence holes) does not necessarily increase as more bridges are added to the trellis. In fact, the number can even decrease, as in the $n = 5$ case discussed below in Sect. 2.5.5. Figure 2.10 shows the corresponding holes 0 through 4 (marked as squares and circles). We ignore all holes numbered 5 and above. There are three families of active bridge classes in T_4 (Fig. 2.10): a_i, b_i, and c_i, with $i = 1, 2$. These three families correspond to the three classes a, b, and c in Fig. 2.5. The classes a_1 and a_2 encircle holes clockwise on the upper right of T^S; b_1 and b_2 encircle holes clockwise on the left of T^S; and c_1 and c_2 encircle holes clockwise on the lower right of T^S. The subscript on each class denotes the number of holes encircled by the class, not counting the inert holes, i.e. those adjacent to T^S. Finally, Fig. 2.10 shows two primary inert classes u_0 and v_0.

To determine how the active classes map forward, we again investigate how a representative bridge in T^U from each class maps forward.

$$T^U[\mathbf{r}_0, \mathbf{s}_0] \mapsto T^U[\mathbf{r}_1, \mathbf{s}_1], \tag{2.24a}$$

$$T^U[\mathbf{p}_0, \mathbf{q}_0] \mapsto T^U[\mathbf{p}_1, \mathbf{q}_1], \tag{2.24b}$$

$$T^U[\mathbf{x}_0, \mathbf{w}_0] \mapsto T^U[\mathbf{x}_1, \mathbf{y}_0] \cup T^U[\mathbf{y}_0, \mathbf{z}_0] \cup T^U[\mathbf{z}_0, \mathbf{w}_1], \tag{2.24c}$$

$$T^U[\mathbf{p}_1, \mathbf{q}_0] \mapsto T^U[\mathbf{p}_2, \mathbf{r}_0] \cup T^U[\mathbf{r}_0, \mathbf{s}_0] \cup T^U[\mathbf{s}_0, \mathbf{q}_1], \tag{2.24d}$$

$$T^U[\mathbf{r}_1, \mathbf{s}_1] \mapsto T^U[\mathbf{r}_2, \boldsymbol{\ell}_0] \cup T^U[\boldsymbol{\ell}_0, \mathbf{g}_0] \cup T^U[\mathbf{g}_0, \mathbf{s}_2], \tag{2.24e}$$

$$T^U[\mathbf{p}_1, \mathbf{q}_1] \mapsto T^U[\mathbf{p}_2, \mathbf{x}_0] \cup T^U[\mathbf{x}_0, \mathbf{w}_0] \cup T^U[\mathbf{w}_0, \mathbf{q}_2]. \tag{2.24f}$$

Replacing each bridge in the above by its bridge class, we obtain

$$M(a_1) = c_1, \tag{2.25a}$$

$$M(a_2) = c_2, \tag{2.25b}$$

$$M(b_1) = b_2 u_0 b_2^{-1}, \tag{2.25c}$$

$$M(b_2) = b_2 a_1 b_2^{-1}, \tag{2.25d}$$

$$M(c_1) = c_2^{-1} v_0 c_2, \tag{2.25e}$$

$$M(c_2) = c_2^{-1} b_1 c_2, \tag{2.25f}$$

with transition matrix

$$\mathsf{T} = \begin{array}{c} \\ a_1 \\ a_2 \\ b_1 \\ b_2 \\ c_1 \\ c_2 \end{array} \begin{array}{c} \begin{array}{cccccc} a_1 & a_2 & b_1 & b_2 & c_1 & c_2 \end{array} \\ \begin{bmatrix} 0 & 0 & 0 & 1 & 0 & 0 \\ 0 & 0 & 0 & 0 & 0 & 0 \\ 0 & 0 & 0 & 0 & 0 & 1 \\ 0 & 0 & 2 & 2 & 0 & 0 \\ 1 & 0 & 0 & 0 & 0 & 0 \\ 0 & 1 & 0 & 0 & 2 & 2 \end{bmatrix} \end{array}. \tag{2.26}$$

Note, that Eqs. (2.25) mix active symbols between the left- and right-hand sides; the symbolic dynamics is transitive. The topological entropy of the trellis T_4 is then

$$h_4 = \ln \lambda = 0.9181. \tag{2.27}$$

This is indeed greater than $h_3 = 0.6931$, but less than the topological entropy of the period-three orbit $h_{\rm po3} = \ln\left(3 + \sqrt{5}\right) = 0.9624$.

2.5.5 The development of the trellis at $n = 5$

To construct the trellis T_5 (Fig. 2.11), we take the union of T_4 (Fig. 2.10) with the forward iterate of the inert bridges $T^U[\mathbf{y}_0, \mathbf{z}_0]$ and $T^U[\mathbf{g}_0, \boldsymbol{\ell}_0]$ from $T_4 \cap U_4$. The forward iterate of the latter produces two new intersections $\mathbf{d}_0$ and $\mathbf{e}_0$. Furthermore, the trajectories $\mathbf{d}_i$ and $\mathbf{e}_i$ are the

only pseudoneighbor pairs in T_5, similar to the case seen at $n = 2$. There is thus a single trajectory of holes, denoted by circles in Fig. 2.11, where we ignore holes 6 and higher and the holes -1 and lower.

Following the same naming convention as the $n = 4$ case, there are four active bridge classes a_1, b_1, b_2, c_1, and one primary inert class u_0. Representative curves of the active classes map forward as follows.

$$T^U[\mathbf{r}_0, \mathbf{s}_0] \mapsto T^U[\mathbf{r}_1, \mathbf{s}_1], \tag{2.28a}$$

$$T^U[\boldsymbol{\ell}_0, \mathbf{g}_0] \mapsto T^U[\boldsymbol{\ell}_1, \mathbf{d}_0] \cup T^U[\mathbf{d}_0, \mathbf{e}_0] \cup T^U[\mathbf{e}_0, \mathbf{g}_1], \tag{2.28b}$$

$$T^U[\mathbf{p}_1, \mathbf{q}_0] \mapsto T^U[\mathbf{p}_2, \mathbf{r}_0] \cup T^U[\mathbf{r}_0, \mathbf{s}_0] \cup T^U[\mathbf{s}_0, \mathbf{q}_1], \tag{2.28c}$$

$$T^U[\mathbf{r}_1, \mathbf{s}_1] \mapsto T^U[\mathbf{r}_2, \boldsymbol{\ell}_0] \cup T^U[\boldsymbol{\ell}_0, \mathbf{g}_0] \cup T^U[\mathbf{g}_0, \mathbf{s}_2], \tag{2.28d}$$

which gives the following dynamics for the active bridge classes,

$$M(a_1) = c_1, \tag{2.29a}$$

$$M(b_1) = b_2 u_0 b_2^{-1}, \tag{2.29b}$$

$$M(b_2) = b_2 a_1 b_2^{-1}, \tag{2.29c}$$

$$M(c_1) = c_1^{-1} b_1 c_1, \tag{2.29d}$$

and the transition matrix

$$\mathsf{T} = \begin{array}{c} \\ a_1 \\ b_1 \\ b_2 \\ c_1 \end{array} \begin{array}{c} \begin{array}{cccc} a_1 & b_1 & b_2 & c_1 \end{array} \\ \begin{bmatrix} 0 & 0 & 1 & 0 \\ 0 & 0 & 0 & 1 \\ 0 & 2 & 2 & 0 \\ 1 & 0 & 0 & 2 \end{bmatrix} \end{array}. \tag{2.30}$$

with topological entropy

$$h_5 = \ln\left(\sqrt{\sqrt{2}+1}+1\right) = 0.9376. \tag{2.31}$$

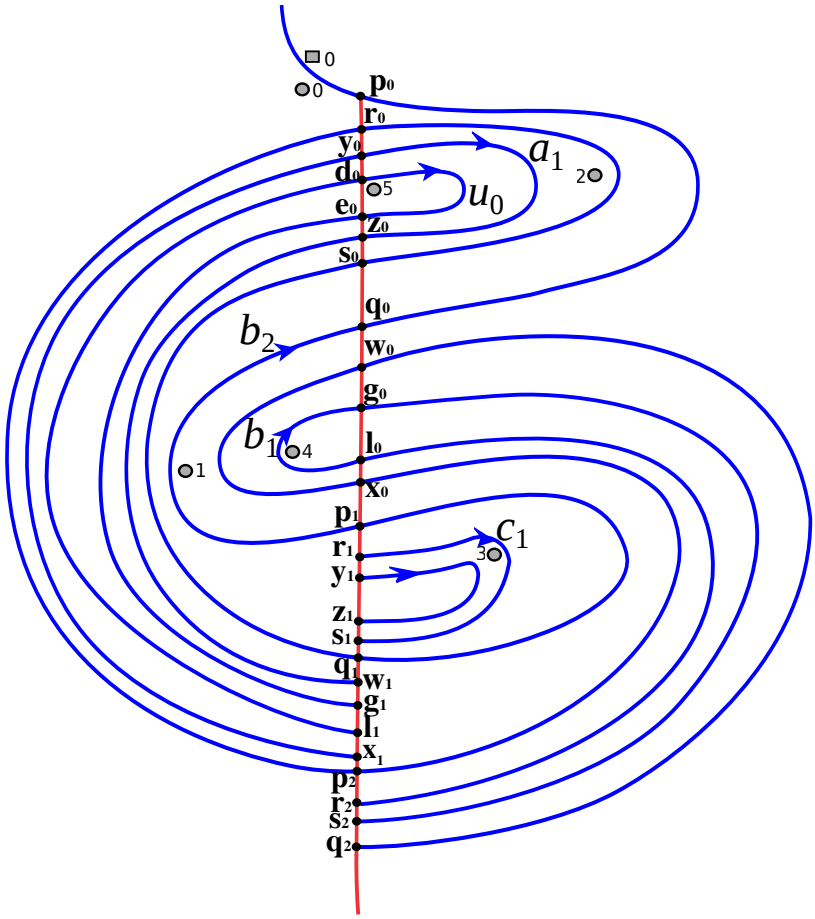

Figure 2.11. Schematic illustration of the development of the trellis at $n = 5$.

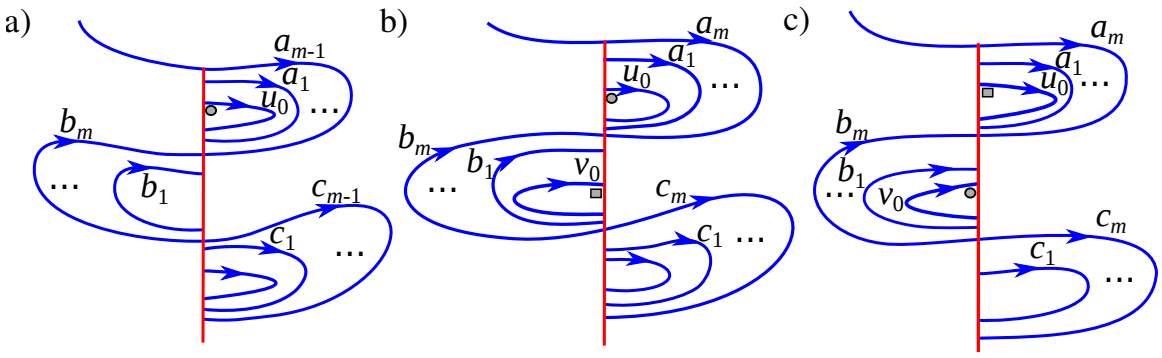

Figure 2.12. Representative bridge classes for general values of n. a) $n = 3k - 1$, $m = k$; b) $n = 3k$, $m = 2k - 1$; c) $n = 3k + 1$, $m = 2k$. In all cases, $k = 1, 2, ...$

2.5.6 The development of the trellis for $n = 3k - 1$

In Sects. 2.5.6 – 2.5.8, we summarize the results for a general trellis with $n \geq 2$. These results can be proved by induction by iterating the inert classes under the dynamics of Eqs. (2.9).

A schematic of the trellis at $n = 3k - 1$, $k = 1, 2, ...,$ is shown in Fig. 2.12a. There is a single trajectory of holes. Of these, only the first hole to lie adjacent to T^S is shown. This hole is surrounded by an inert bridge of class u_0. There are $m = k$ bridges of type b_i, nested within one another, and similarly $m - 1$ bridges of type a_i and c_i

$$a_1, ..., a_{m-1} \qquad b_1, ..., b_m \qquad c_1, ..., c_{m-1} \quad m = k \tag{2.32}$$

Only one representative of each class is shown in the figure. These classes map forward according to

$$M(a_i) = c_i, \quad i = 1, ..., m - 1, \tag{2.33a}$$

$$M(b_1) = b_m u_0 b_m^{-1}, \tag{2.33b}$$

$$M(b_i) = b_m a_{i-1} b_m^{-1}, \quad i = 2, ..., m, \tag{2.33c}$$

$$M(c_i) = c_{m-1}^{-1} b_i c_{m-1}, \quad i = 1, ..., m - 1. \tag{2.33d}$$

These equations reduce to Eqs. (2.14) and (2.29), for $n = 2$ and $n = 5$, respectively. Eqs. (2.33) yield the transition matrix

$$\mathsf{T} = \begin{array}{c} \\ a_1 \\ \\ a_{m-1} \\ b_1 \\ \\ \\ b_m \\ c_1 \\ \\ c_{m-1} \end{array} \begin{array}{c} \begin{array}{ccccccc} a_1 & \cdots & a_{m-1} & b_1 & \cdots & b_m & c_1 \cdots c_{m-1} \end{array} \\ \left[\begin{array}{c|c|c} \multirow{3}{*}{0} & \begin{array}{cccc} 0 & 1 & 0 \cdots & 0 \\ & \ddots & \ddots & \vdots \\ & & \ddots & 0 \\ 0 & \cdots & 0 & 1 \end{array} & \multirow{3}{*}{0} \\ & & \\ & & \\ \hline \multirow{3}{*}{0} & \begin{array}{cccc} 0 & \cdots & \cdots & 0 \\ \vdots & & & \vdots \\ \vdots & & & \vdots \\ 0 & \cdots & \cdots & 0 \end{array} & \begin{array}{ccc} 1 & 0 \cdots & 0 \\ 0 & \ddots & \vdots \\ \vdots & \ddots & 0 \\ 0 & \cdots & 1 \end{array} \\ & & \\ & \begin{array}{cccc} 2 & \cdots & \cdots & 2 \end{array} & \begin{array}{ccc} 0 & \cdots & 0 \end{array} \\ \hline \multirow{3}{*}{I} & \multirow{3}{*}{0} & \begin{array}{ccc} 0 & \cdots & 0 \\ \vdots & & \vdots \\ 0 & \cdots & 0 \\ 2 & \cdots & 2 \end{array} \\ & & \\ & & \\ \end{array}\right] \end{array} . \tag{2.34}$$

2.5.7 The development of the trellis for $n = 3k$

A schematic of the trellis at $n = 3k$, $k = 1, 2, ...$, is shown in Fig. 2.12b. There are now two trajectories of holes. Again only the first holes to lie adjacent to T^S are shown. These holes are surrounded by the inert classes u_0 and v_0. There are now $m = 2k - 1$ bridge classes of each type

$$a_1, ..., a_m \qquad b_1, ..., b_m \qquad c_1, ..., c_m \quad m = 2k - 1. \tag{2.35}$$

These classes map forward according to

$$M(a_i) = c_i, \quad i = 1, ..., m, \tag{2.36a}$$

$$M(b_1) = b_m u_0 b_m^{-1}, \tag{2.36b}$$

$$M(b_i) = b_m a_{i-1} b_m^{-1}, \quad i = 2, ..., m, \tag{2.36c}$$

$$M(c_1) = c_m^{-1} v_0 c_m, \tag{2.36d}$$

$$M(c_i) = c_m^{-1} b_{i-1} c_m, \quad i = 2, ..., m. \tag{2.36e}$$

These equations reduce to Eqs. (2.20) for $n = 3$. Eqs. (2.36) yield the transition matrix

$$\mathsf{T} = \begin{array}{c} \\ a_1 \\ \vdots \\ a_m \\ b_1 \\ \vdots \\ b_m \\ c_1 \\ \vdots \\ c_m \end{array} \begin{array}{c} \begin{array}{cccccccc} a_1 & \cdots & a_m & b_1 & & & b_m & c_1 & & c_m \end{array} \\ \left[\begin{array}{cccc|cccc|cccc} & & & & 0 & 1 & 0 & 0 & & & & \\ & & & & & \ddots & & \vdots & & & & \\ & 0 & & & & & & 0 & & 0 & & \\ & & & & & & & 1 & & & & \\ & & & & 0 & & & 0 & & & & \\ \hline & & & & 0 & & & 0 & 0 & 1 & 0 & 0 \\ & 0 & & & & & & & & & & 0 \\ & & & & 0 & & & 0 & & & & 1 \\ & & & & 2 & & & 2 & 0 & & & 0 \\ \hline & & & & & & & & 0 & & & 0 \\ & I & & & & 0 & & & & & & \\ & & & & & & & & 0 & & & 0 \\ & & & & & & & & 2 & & & 2 \end{array}\right] \end{array} . \tag{2.37}$$

2.5.8 The development of the trellis for $n = 3k + 1$

A schematic of the trellis at $n = 3k + 1$, $k = 1, 2, ...$, is shown in Fig. 2.12c. There are again two trajectories of holes, but there are now $m = 2k$ bridge classes of each type

$$a_1, ..., a_m \qquad b_1, ..., b_m \qquad c_1, ..., c_m \quad m = 2k. \tag{2.38}$$

These classes map forward according to the same Eqs. (2.36) with the same transition matrix Eq. (2.37) as above. These equations reduce to Eqs. (2.25) for $n = 4$.

2.6 For $\bar{\tau}_f < 1$, T_n yields a lower bound on the topological entropy of the fluid flow

Though the trellis T_n was extracted as a finite length approximation to the tangle forced by the braiding of the period-three orbit $\boldsymbol{\rho}_i$, *any* tangle that has T_n as a subtrellis must have a topological entropy at least equal to the topological entropy of T_n itself. Furthermore, though the period-three orbit vanishes below $\bar{\tau}_f = 1$, the trellises T_n persist to lower $\bar{\tau}_f$ values. Thus, these trellises provide a rigorous method by which we may bound the topological entropy below $\bar{\tau}_f = 1$, without relying

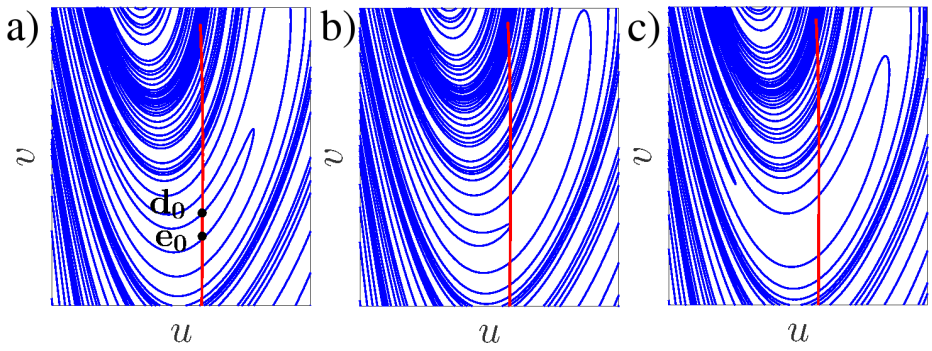

Figure 2.13. Transition of the trellis from $n = 5$ to $n = 4$ as $\bar{\tau}_f$ is lowered. The pseudoneighbors $\mathbf{d}_0$ and $\mathbf{e}_0$ from Fig. 2.11 at $\bar{\tau}_f = 0.932$ (dots in panel a) merge together at a heteroclinic tangency at $\bar{\tau}_f = 0.921$ (panel b) and disappear at $\bar{\tau}_f = 0.911$ (panel c).

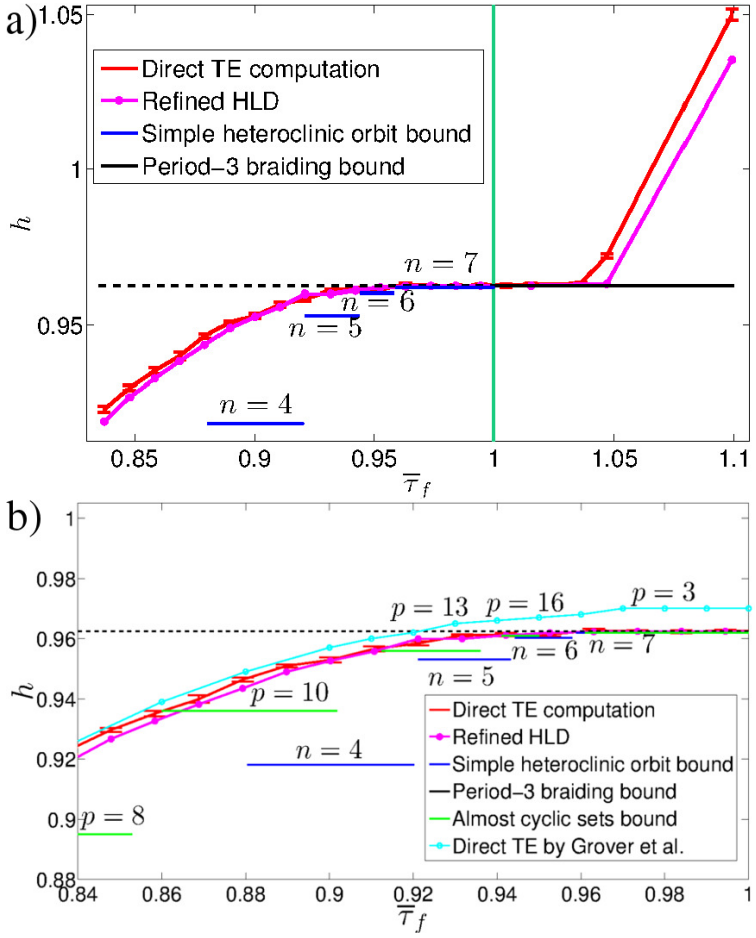

Figure 2.14. Topological entropy results. a) Comparison of the direct computation of topological entropy (red), refined HLD (magenta), simple heteroclinic orbit bound (blue), and period-three braiding bound (black) over the full $\bar{\tau}_f$ interval studied. Error bounds (red) are 95% confidence intervals computed from the exponential fit. b) Comparison of the results in (a) to the value using almost-cyclic sets (green) in Grover et al., Chaos, Vol. 22, Pg. 12 (2012) AIP [33].

on the period-three orbit, which does not exist, or indeed any other periodic orbit, with the exception of the two fixed points $\mathbf{z}_u$ and $\mathbf{z}_\ell$, which persist to $\bar{\tau}_f = 0$.

As $\bar{\tau}_f$ is lowered for a given trellis T_n, the first heteroclinic intersections of T_n to vanish in a bifurcation must be a pair of pseudoneighbors. That is, the pseudoneighbors of T_n force all the other heteroclinic intersections of T_n to exist. Thus, to determine the lowest $\bar{\tau}_f$ value at which T_n forms a subtrellis of the full tangle, we need only track the pseudoneighbors and determine when they collide in a tangency between the stable and unstable manifolds. An example is shown for T_5 in Fig. 2.13, where we see that T_5 persists down to $\bar{\tau}_f = 0.923$. In a similar manner, we determine the lowest value of $\bar{\tau}_f$ for which T_n exists for all $n = 4, 5, 6, 7$. These $\bar{\tau}_f$-values form the left endpoints of the horizontal segments in Fig. 2.14. The vertical positions of the segments are the topological entropies h_n of T_n, as computed in Sect. 2.5. As expected, h_n falls below the direct topological entropy computation of the fluid, and even provides a fairly accurate estimate of the fluid entropy down to $n = 6$. At $n = 5$ and lower, however, a noticeable gap develops between the fluid entropy and the h_n bound. This difference is due to the finite length of T_n, and in particular the failure of T_n to account for the future behavior of its inert bridge classes. For example, in Fig. 2.11, the trellis T_5 contains the inert bridge $T^U[\mathbf{y}_1, \mathbf{z}_1]$, but contains no information about when its forward iterate develops new intersections. At some future iterate $T^U[\mathbf{y}_1, \mathbf{z}_1]$ must produce more intersections with T^S, and must hence generate more topological entropy, but T_5 contains no information about when this will happen or how many new intersections will be produced when it does happen. This problem can be addressed by using a longer and more detailed trellis to approximate the dynamics; this is studied in Sect. 2.7.

The topological entropy h_n of the trellis T_n can be interpreted as resulting from the braiding of the pseudoneighbor orbits; this is analogous to the topological entropy generated by the braiding of periodic orbits (Sect. 2.5) except that the pseudoneighbors are heteroclinic and do not close on themselves. Only one orbit from each pseudoneighbor pair is needed, which can be taken to be the orbit next to which the hole is punched. For T_5, there is a single pair of pseudoneighbor orbits $\mathbf{d}_i$ and $\mathbf{e}_i$ (Fig. 2.11). Fig. 2.15a shows points from the orbit $\mathbf{d}_i$ evolved forward in time. The dots show the heteroclinic intersections $\mathbf{d}_i$ at $t = 0$, while the curves show the evolution of each intersection from $t = 0$ to $t = \bar{\tau}_f$. In that time, $\mathbf{d}_i$ evolves forward to $\mathbf{d}_{i+1}$. Some of these forward evolution

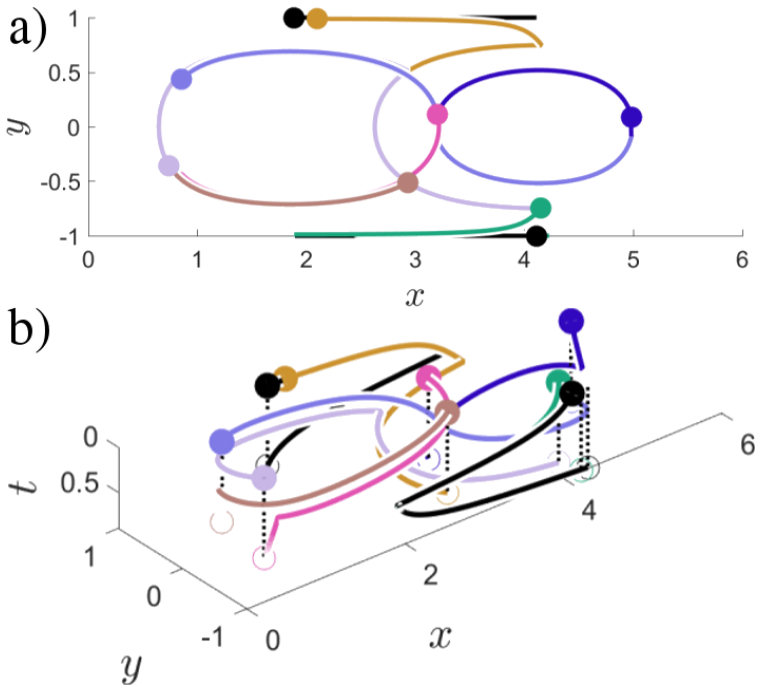

Figure 2.15. Visual representation of the heteroclinic orbit braid (colored curves) for n=4 shown in a) the xy space viewed from above the xy plane and b) the xyt space. The two black curves are the two periodic orbits at the top and bottom boundary of the cavity.

curves intersect. The trajectory that arrives first is shown above the trajectory that arrives later. A more three-dimensional view is shown in Fig. 2.15b, plotted in xyt-space, where time t progresses downward. In this way, we have a visual representation of the braid formed by the heteroclinic trajectory $\mathbf{d}_i$. Note that this braid has an infinite number of strands, one strand for each value of i, and that none of the strands themselves are periodic. However, an infinity of strands converge upon the top boundary of the cavity (going backward in time), ultimately following the periodic orbit swept out by the fixed point $\mathbf{z}_u$ of M. A similar infinity of strands converge upon the periodic orbit swept out by the fixed point $\mathbf{z}_\ell$ at the bottom of the cavity. Only a finite number of strands are responsible for truly stirring the interior of the fluid domain.

2.7 Automated HLD analysis yields a tight lower bound on topological entropy

As noted above, the lower bound given by h_n to the topological entropy h of the fluid flow is not tight for all $\bar{\tau}_f$ values because the bridges included in T_n can fail to capture a significant portion of the topological structure. We can thus address this deficiency by using a trellis with more bridges covering a larger fraction of the phase space. In practice, we construct such a trellis by setting an area-criterion for iterating a given bridge forward. Specifically, to determine whether a bridge is iterated forward, we compute the areas of the trellis domains on both sides of a bridge; here, trellis domains refer to those connected regions of phase space obtained by cutting phase space along the stable and unstable segments of T^S and T^U. If both areas are greater than some specified area tolerance, the given bridge is mapped forward to a new set of bridges, which are then added to the trellis. By using a sufficiently small area tolerance, we can refine the trellis to a high degree. In this study, the area tolerance used is 0.005 for values of $\bar{\tau}_f$ less than 0.932 and 0.001 for values of $\bar{\tau}_f$ greater than 0.932. A smaller tolerance is used when more bridges are created, i.e. when there is more topological entropy.

The HLD algorithm in Refs. [53, 54] for computing symbolic dynamics has been automated in MATLAB. It can handle a trellis of arbitrary complexity. Thus, once a refined trellis has been computed, the HLD technique can be applied to it automatically, yielding symbolic dynamics and the topological entropy of the trellis.

We summarize our automated approach for computing topological entropy. For a fixed area tolerance, we compute the trellis by iterating bridges forward n times, using the area criterion mentioned above to determine whether a bridge should or should not be iterated at each step. The first iterate $n = 1$ is the iterate of the initial unstable segment from the fixed point $\mathbf{z}_u$ to the pip $\mathbf{p}_0$. At each value of n we compute the topological entropy h from the trellis using the automated MATLAB code. Figure 2.16a shows h versus iterate n for different values of the area tolerance at $\bar{\tau}_f = 0.9$. For each area tolerance, the topological entropy appears to have converged by $n = 13$. Figure 2.16b shows h versus the area tolerance at the fixed value of $n = 14$. h increases monotonically as the area tolerance decreases. The value of h for the smallest area tolerance of

0.001 appears within the error bars for the direct computation of topological entropy (red horizontal lines.)

We repeat the above procedure for a range of $\bar{\tau}_f$ values. Figure 2.14 records the topological entropy (magenta) computed from the trellis with the smallest area tolerance (either 0.001 or 0.005) and the most iterates ($n = 14$ for all but the largest value $\bar{\tau}_f = 1.099$). This curve is a lower bound on the true topological entropy of the fluid flow. For $\bar{\tau}_f < 1$ the lower bounds are quite good, with only a small gap less than about 0.004 between the direct topological entropy computation and the refined HLD computation. For $\bar{\tau}_f \gtrsim 1.05$, the direct computation of topological entropy increases significantly away from h_{po3}.

The refined HLD computation does indeed give a lower bound above h_{po3}, but it is not nearly as tight as at lower values of $\bar{\tau}_f$. This is due to numerical issues that make it harder to compute a sufficient number of bridges in the trellis within a reasonable amount of time. To show this computation in more detail, Fig. 2.17 repeats the analysis of Fig. 2.16 for $\bar{\tau}_f = 1.099$. As Fig. 2.17b makes clear, we would need to use a stricter area tolerance in order to resolve more of the topological entropy of the flow. However, this is computationally intensive. Figure 2.18a shows the trellis used at $\bar{\tau}_f = 1.099$ for the smallest area tolerance. It fills in most of the fluid, except for three regions around the period-three orbit. The topological entropy is not as well measured in these three regions, which we believe is the main reason for the large gap between the direct topological entropy computation and the refined HLD topological entropy computation shown on the far right of Fig. 2.14a or in Fig. 2.17b. We believe a more efficient approach to sampling phase space would be to directly target the three undersampled regions by using the tangle attached to hyperbolic period-three orbits within these regions. Such nested tangles approaches have proved useful in prior work [53, 54]. Finally, Figs. 2.18b shows the braiding of pseudoneighbor orbits responsible for "stirring" the fluid at $\bar{\tau}_f = 1.099$. Though the detailed braiding structure can obviously not be discerned in these figures, they give a sense of the complexity involved for more complicated flows.

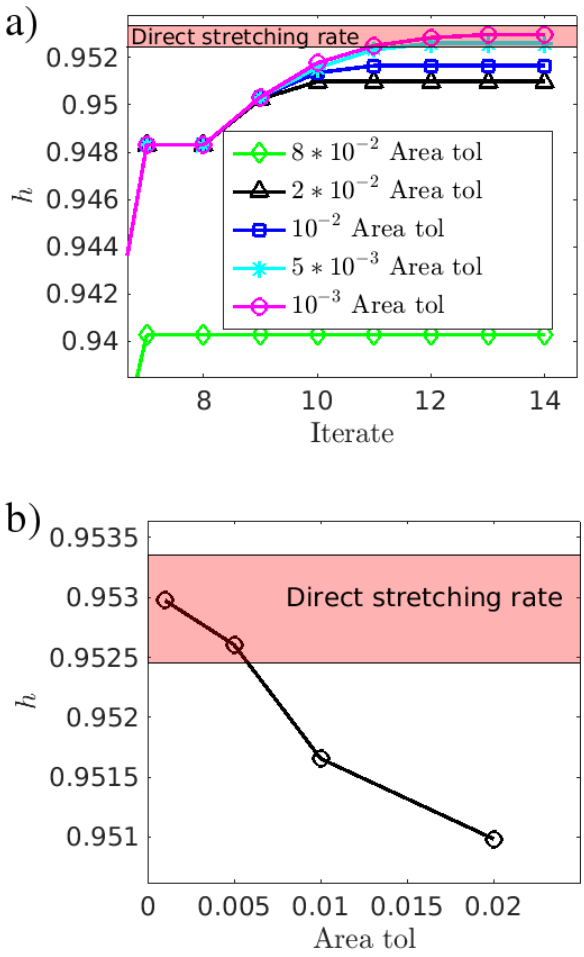

Figure 2.16. Calculation of the HLD topological entropy bound using different values of area cutoff for $\bar{\tau}_f = 0.9$. a) Topological entropy as a function of iterate n for different values of area cutoff. b) Topological entropy as a function of area cutoff for $n = 14$. In both plots the horizontal red lines denote the error bounds on the direct computation of topological entropy.

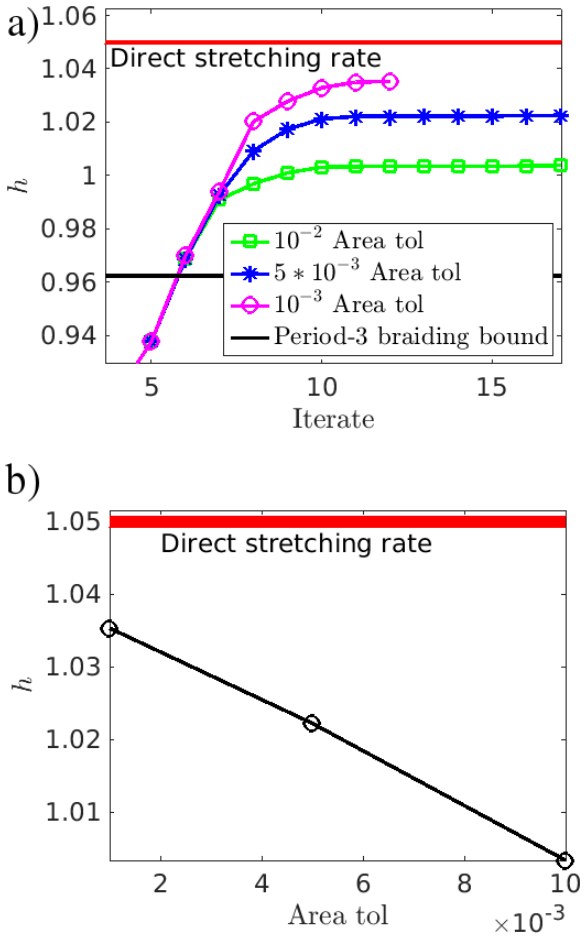

Figure 2.17. Calculation of the HLD topological entropy bound using different values of area cutoff for $\bar{\tau}_f = 1.099$. a) Topological entropy as a function of iterate n for different values of area cutoff. b) Topological entropy as a function of area cutoff for $n = 12$. In both plots the horizontal red lines denote the error bounds on the direct computation of topological entropy.

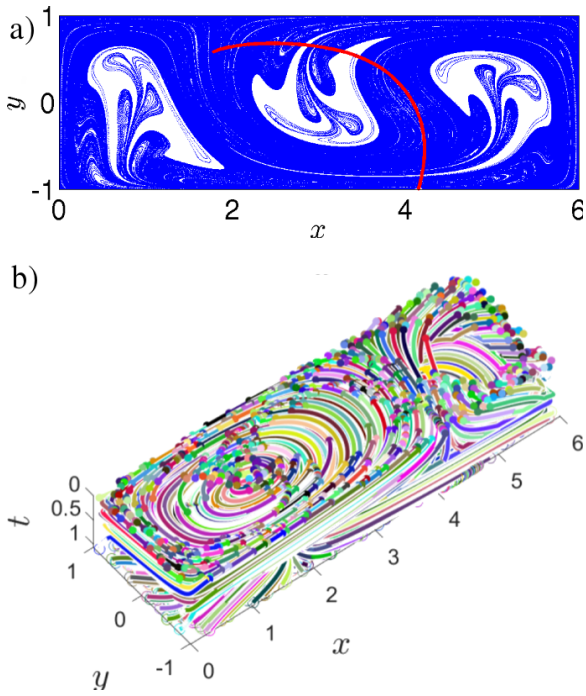

Figure 2.18. a) The refined tangle for $\bar{\tau}_f = 1.099$ computed up to iterate $n = 12$. b) Trajectories of the pseudoneighbors of the refined tangle in the xyt space.

2.8 Comparison to braiding by almost-cyclic sets

Grover et. al [33, 69] explained topological entropy in the absence of the period-three orbit ($\bar{\tau}_f < 1$) by first identifying nearly coherent regions of the fluid that braid around one another in a periodic fashion. These nearly coherent regions are called almost-cyclic sets, and they are identified and computed from an eigenfunction analysis of a set-based approximation to the Frobinous-Perron operator [1, 26, 28, 29]. Since the almost-cyclic sets have a high degree of coherence, they can be viewed as stirring the fluid like true periodic orbits. It is then natural to associate a braid to their motion, even though no periodic orbit within the almost-cyclic sets is shown to exist. Under this approximation, the topological entropy of the braid associated with the almost-cyclic set provides a lower bound to the topological entropy of the fluid motion.

As $\bar{\tau}_f$ is decreased below 1, the period-three orbit disappears, but a period-three almost-cyclic set with the same braid type remains, extending the lower bound h_{po3} below $\bar{\tau}_f = 1$. At about $\bar{\tau}_f = 0.96$ this almost-cyclic set disappears and an almost-cyclic set of period 16, with smaller topological entropy, is formed. In this manner, Grover et al. witness a series of bifurcations of

the almost-cyclic sets with periods $p = 3, 16, 13, 10, 8$, providing a monotonically decreasing set of bounds on the topological entropy as $\bar{\tau}_f$ is lowered. See Fig. 2.14b. This method produces steps in topological entropy, just as our simple heteroclinic orbit bound from Sect. 2.5, though there is no direct relationship between the steps in these two approaches. The two approaches do approximately agree for the almost-cyclic set with $p = 16$ and the simple heteroclinic analysis for $n = 6$. However, the $p = 13$ and $p = 10$ bounds are clearly tighter than the $n = 5$ and $n = 4$ bounds. Furthermore, the left endpoints of the $p = 13$ and $p = 10$ intervals almost exactly agree with our direct computation of the topological entropy. However, the right endpoints of these intervals clearly drops below the direct topological entropy computation, i.e. there is excess topological entropy at the right endpoints that is unexplained by the almost-cyclic sets.

As noted in Sect. 2.7, the refined HLD analysis, which goes beyond that of Sect. 2.5, produces a topological entropy bound that closely follows the direct topological entropy computation. It produces a bound that is comparable to the cyclic-set bound of the left endpoints at $p = 13$ and $p = 10$, but it also produces good bounds at the right endpoints of these intervals. We can thus interpret the heteroclinic orbits at these endpoints as creating the excess topological entropy.

It would be interesting to more directly relate the almost-cyclic-set approach to the heteroclinic orbit approach. For example, it might be that there exist heteroclinic orbits that nearly follow the braiding pattern of the almost cyclic sets.

2.9 Concluding remarks

We have learned from this study that topological entropy can be reliably computed for a realistic fluid model based on the "stirring" of the fluid by heteroclinic orbits. Ultimately, this computation is possible through the use of symbolic dynamics (HLD) derived from finite-length pieces of stable and unstable manifolds. An advantage of this technique is that it only relies on the existence of the periodic orbits to which the stable and unstable manifolds are attached, in this case the period-one orbits on the cavity boundary. These orbits persist for all values of the driving period τ_f, whereas other periodic orbits in the interior of the fluid cavity come or go with changing τ_f values.

The limiting factor in computing topological entropy with HLD is the computation of sufficiently many segments of the unstable manifold, in order to compute sufficiently many heteroclinic intersections contributing to the entropy. This computation of stable and unstable segments can be achieved in various ways, but there are two basic approaches. The first is to simply include in the trellis more and more segments of the manifolds connected to the original fixed points that define the tangle; this is the approach taken in this study. The second is to include in the trellis more periodic orbits (not necessarily fixed points) along with segments of their invariant manifolds. This latter technique allows one to target regions of phase space more precisely, for example, by including new tangles surrounding stable islands. Ultimately, we believe this latter approach will provide a more efficient means of targeting phase space and lead to faster computations of the topological entropy from symbolic dynamics. For example, we could use this approach to refine the topological information surrounding the stable period-three islands that exist for $\bar{\tau}_f > 1$. We plan to explore this issue in future work.

Chapter 3

Computing multiexponential decay rates for the Hénon map

Transport properties of chaotic systems are computable from data extracted from periodic orbits. Given a sufficient number of periodic orbits, the escape rate can be computed using the spectral determinant, a function that incorporates the eigenvalues and periods of periodic orbits. The escape rate computed from periodic orbits converges to the true value as more and more periodic orbits are included. Escape from a given region of phase space can be computed by considering only periodic orbits that lie within the region. An accurate symbolic dynamics along with a corresponding partitioning of phase space is useful for systematically obtaining all periodic orbits up to a given period, to ensure that no important periodic orbits are missing in the computation. Homotopic lobe dynamics (HLD) is an automated technique for computing accurate partitions and symbolic dynamics for maps using the topological forcing of intersections of stable and unstable manifolds of a few anchor periodic orbits. In this study, we apply the HLD technique to compute symbolic dynamics and periodic orbits to compute distinct escape rates from different regions of phase space for the Hénon map. We focus on computing escape rates in parameter ranges spanning hyperbolic plateaus, which are intervals of parameter where the dynamics is hyperbolic and the symbolic dynamics does not change. After the periodic orbits are computed for a single parameter value within a hyperbolic plateau, periodic orbit continuation is used to compute periodic orbits over an interval that spans the hyperbolic plateau. From the periodic orbits, the escape rate is accurately

computed over the hyperbolic plateau using the spectral determinant, and escape from individual regions of phase space is computed by considering only periodic orbits that lie in those regions. The escape rates computed from a few thousand periodic orbits agree with escape rates computed from Monte Carlo simulations requiring hundreds of billions of orbits.

The escape rate of asteroids, chemical reaction rates, and fluid mixing rates are all examples of chaotic transport rates. One can compute transport rates by launching a Monte Carlo simulation over millions of trajectories. However, it is possible extract this information from a much smaller number of trajectories. One method of doing so is by focusing on unstable periodic orbits, which form the skeleton for the long-time behavior of chaotic dynamical systems. The local stretching near periodic orbits contributes to the overall escape rate which can be computed from the spectral determinant, a function which incorporates the eigenvalues of the periodic orbits. We classify and find periodic orbits using finite-length segments of a heteroclinic tangle, which is a collection of invariant manifolds and their intersections. The heteroclinic tangle encodes the topology of phase space and can be used to compute the system's symbolic dynamics, giving additional insight on how material is transported in phase space, and allowing for characterizing and computing periodic orbits. The use of heteroclinic tangles to compute symbolic dynamics can improve estimates of chaotic transport rates in a broad range of deterministic chaotic dynamical systems.

3.1 Introduction

We study asymptotic transport rates in chaotic systems, namely the escape rates of trajectories from one region of phase space to another. The calculation of escape rates has direct physical applications such as computing atomic ionization rates, chemical reaction rates, and the escape rates of asteroids. Given physically relevant criteria for survival and escape, a chaotic system can exhibit an exponential decay given by

$$N(t) = N_0 e^{-\gamma t}, \tag{3.1}$$

where $N(t)$ is the number of surviving trajectories as a function of time, N_0 is a constant, and γ is the asymptotic escape rate. The escape rate γ can be computed via Monte Carlo simulation

by iterating an initial ensemble of points forward in time and counting the number of surviving trajectories as a function of time. Unfortunately a large number of initial points, often exceeding the millions or billions, can be necessary to accurately resolve the asymptotic escape rate.

Our aim is to compute γ using fewer orbits, namely unstable periodic orbits. Gutzwiller [34, 35] made early insights in methods using periodic orbits when he developed the Gutzwiller trace formula, which he used to compute quantum eigenvalues in the anisotropic Kepler problem (the computation of classical escape rates follows directly from Gutzwiller's semiclassical formulation.) Although Gutzwiller's original trace formula method did not permit the convergent computation of individual quantum eigenvalues, subsequent reformulations in terms of cycle expansions of spectral determinants, or "zeta functions," provided better convergence properties. For example, Cvitanovic and Eckhardt [17] successfully computed individual complex resonances of the three-disk scattering problem based on cycle expansions. An in-depth explanation of spectral determinants along with examples of escape rate computations can be found in The Chaos Book [16]. Our work is also motivated by prior theoretical and experimental work demonstrating the role of periodic orbits in quantum chaos [20, 21, 39, 40, 44, 49, 50].

For a system such as the three-disk scattering problem, the periodic orbits can be labeled by a simple symbolic labeling based on the sequence of disks that are visited. Given a set of allowed symbol sequences, known as the system's symbolic dynamics, one can write down the symbolic itinerary for any periodic orbit. This ability allows for accurately characterizing and computing all periodic orbits up to a chosen period, which is necessary to apply the spectral determinant and compute escape rates. In many realistic physical systems, however, the construction of symbolic dynamics is not obvious, making the periodic orbits difficult to characterize and compute. *We wish to compute escape rates in realistic physical systems from the spectral determinant by computing periodic orbits using improved methods of computing symbolic dynamics*. The ability to systematically compute symbolic dynamics, partitions, and periodic orbits allows for applying periodic orbit theory to a broad range of physical applications, including studying the role of periodic orbits in quantum chaos in a real physical system, which is a future goal of this work.

One challenge we wish to address is computing escape rates in a mixed Hamiltonian phase space, where stable islands are embedded in a chaotic sea. The rich fractal structure of escape

dynamics near the stable islands leads to two complications in computing the spectral determinant. The first complication is that the symbolic dynamics becomes very complex, requiring hundreds of symbols, and more complicated periodic orbits are necessary to converge to the true escape rate. The second complication is that the system no longer exhibits a single exponential escape rate as in Eq. (4.1), but rather a multiexponential escape rate given by

$$N(t) = N_0 e^{-\gamma_0 t} + N_1 e^{-\gamma_1 t} + N_2 e^{-\gamma_2 t} + ..., \tag{3.2}$$

where N_0, N_1, N_2 are constants and $\gamma_0, \gamma_1, \gamma_2$ are different escape rates representing different regions of phase space. An example of a bi-exponential escape rate is shown in Fig. 3.3. When the number of terms in Eq. (4.2) is infinite, the resulting curve is an algebraic escape rate.

We address these two complications by using a technique called homotopic lobe dynamics [53, 54] (HLD), which uses the topological forcing by intersections of stable and unstable manifolds of a few anchor orbits to compute symbolic dynamics and partition the phase space. Using HLD, an arbitrarily accurate partition of phase space can be computed by incorporating longer and longer segments of the stable and unstable manifolds of anchor orbits. Moreover, the periodic orbits are identified by which region of phase space they occur in, and the distinct escape rates γ_i in Eq. (4.2) can be computed by computing the spectral determinant using only periodic orbits that lie in the region from which escape is being computed from (see Sect. 3.7). The HLD technique can be used to specifically target the symbolic dynamics of a given region to search for periodic orbits in that region. Once the periodic orbits and their eigenvalues are computed, the spectral determinant is used to compute the escape rate. The escape rate computed from the spectral determinant is compared to Monte Carlo computations. This work augments previous studies on heteroclinic tangles by using the symbolic dynamics computed from HLD to compute periodic orbits and transport rates. For other approaches to symbolic dynamics of tangles, see Refs. [12–15, 22, 23, 64, 65].

Although we provide the machinery for computing the spectral determinant in a mixed phase space, we focus this study on a system where the accuracy of the symbolic dynamics can be verified. One way to verify the accuracy of symbolic dynamics is by computing the topological entropy, a measure of complexity and mixing in phase space. Once the symbolic dynamics is computed

from HLD, the topological entropy computed by taking the natural log of the largest eigenvalue of the transition matrix. Over the intervals of Hénon map studied in Sect. 3.6, for example, the topological entropy computed from HLD matches the values computed using a method based on computational Conley index theory by Frongillo et. al [19, 25], and also matches the topological entropy values computed using pruning of symbolic dynamics by Hagiwara and Shudo [36]. Agreement in topological entropy indicates that our symbolic dynamics accounts for all periodic orbits. Therefore, by computing periodic orbits over the ranges of hyperbolic plateaus, which are intervals of parameter where the symbolic dynamics does not change, we can accurately compute the escape rate using the spectral determinant. We also study what happens to the convergence of the escape rate as the parameter is varied within and away from the hyperbolic plateau. To compute multiexponential escape rates, we focus on a parameter range where a subregion of phase space is within a hyperbolic plateau, while the full phase space has a higher topological entropy and may or may not be hyperbolic.

This paper is organized as follows. Section 3.2 summarizes the method for computing the escape rate from periodic orbits using the spectral determinant. Section 3.3 introduces the map used in our study, the area-preserving Hénon map. Section 3.4 details the numerical technique for computing the escape rate directly from a Monte Carlo simulation. Section 3.5 describes the two-symbol symbolic dynamics for an interval of parameter of the Hénon map, and presents the escape rate data computed from periodic orbits over this parameter range. Section 3.6 presents the symbolic dynamics and partitions for two hyperbolic plateaus of the Hénon map, along with periodic orbits and the escape rates computed from periodic orbits. Section 3.7 presents the symbolic dynamics and escape rates for a parameter range where the Hénon map exhibits multiexponential escape rates, namely a faster short-time escape rate and a slower, long term escape rate. Section 3.8 compares the results computed from HLD with those computed from continuing orbits downward from the full shift on two symbols.

3.2 Computing Escape Rates from Periodic Orbits Using the Spectral Determinant

We present the derivation of the spectral determinant for computing the escape rate γ in Eq. (4.1) following the discussion in Chaos Book [16]. The following derivation applies for area-preserving maps on a 2D plane, but a similar function applies for continuous-time maps and in higher dimensions [16]. For a mapping $f(x)$, the Perron-Frobinous operator given by

$$\mathcal{L}(y,x) = \delta(y - f(x)) \tag{3.3}$$

is used to compute the escape rate. The Perron-Frobinious operator is used to map forward *densities* using the formula

$$\rho'(y) = \int dx \mathcal{L}(y,x)\rho(x) \tag{3.4}$$

where ρ is an initial distribution of densities in phase space and ρ' is the mapped distribution of densities. The escape rate γ is equal to the natural log of the largest eigenvalue λ of $\mathcal{L}$. One way to compute the leading eigenvalue of $\mathcal{L}$ is to find the zeros of the determinant $\det(1 - z\mathcal{L})$, known as the spectral determinant. The smallest real root of the spectral determinant greater than 1 yields λ in the form $z = 1/\lambda$, where $\lambda = e^{\gamma}$. The spectral determinant can be written as a power series given by

$$\det(1 - z\mathcal{L}) = 1 - \sum_{n=1}^{\infty} Q_n z^n, \tag{3.5}$$

where Q_n are coefficients to be determined. The computation of γ then lies in computing the coefficients Q_n and finding the zeros of Eq. (3.5). To compute the coefficients Q_n, it helps to take the logarithmic derivative of the spectral determinant. The logarithmic derivative of the spectral determinant be written in terms of the trace using the identity

$$\begin{aligned} \text{tr}\left(\frac{z\mathcal{L}}{1 - z\mathcal{L}}\right) &= -z\frac{d}{dz}\ln\det(1 - z\mathcal{L}) \\ &= -\frac{z\frac{d}{dz}\det(1 - z\mathcal{L})}{\det(1 - z\mathcal{L})}. \end{aligned} \tag{3.6}$$

The left hand side of Eq. (3.6) can be expanded in a Taylor series in z as

$$\text{tr}\left(\frac{z\mathcal{L}}{1-z\mathcal{L}}\right) = \sum_{n=1}^{\infty} C_n z^n, \tag{3.7}$$

where

$$C_n = \text{tr}(\mathcal{L}^n) \tag{3.8}$$

are known as the trace coefficients. Taking the derivative in Eq. (3.6) and substituting Eqs. (3.5) and (3.7) into Eq. (3.6) yields the equation

$$(1 - \sum_{n=1}^{\infty} Q_n z^n) \sum_{n=1}^{\infty} C_n z^n = \sum_{n=1}^{\infty} n Q_n z^n. \tag{3.9}$$

Equation (3.9) provides a convenient way to compute the coefficients Q_n in terms of the coefficients C_n. Plugging in $n = 1$ shows that $Q_1 = C_1$, and it is easy to prove by induction that

$$Q_n = \frac{1}{n}[C_n - \sum_{i=1}^{n-1} Q_i C_{n-i}]. \tag{3.10}$$

The coefficients C_n are defined in Eq. (3.8) and can be written as

$$C_n = \int dx \mathcal{L}^n(x,x) = \int dx \delta(x - f^n(x). \tag{3.11}$$

The delta function in Eq. (3.11) picks up a contribution whenever x is a fixed point of $f^n(x)$, and so

$$C_n = \sum_{x_*} \frac{1}{|\det(1 - \frac{\partial f^n}{\partial x}|_{x_*})|}, \tag{3.12}$$

where the sum is taken over all fixed points x_* of f^n. A *prime* periodic orbit is one that is not a copy (or several copies) of a lower-period orbit retracing itself. Equation (3.12) can be re-written in terms of *prime* orbits as

$$\begin{aligned} C_n &= \sum_p n_p \sum_{r=1}^{\infty} \frac{1}{|\det(1 - M_p^r)|} \delta_{r n_p n}, \\ |\det(1 - M_p^r)| &= |(1 - \lambda_p^r)\left(1 - \lambda_p^{-r}\right)|, \end{aligned} \tag{3.13}$$

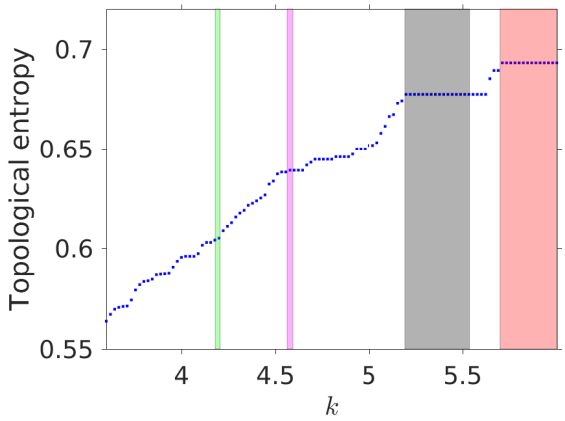

Figure 3.1. The topological entropy lower bound computed from HLD as a function of k for the area-preserving Hénon map. The vertical bands indicate the parameter ranges whose periodic orbits are computed in Sects. 3.5-3.7. The right-most band (red) marks the k interval $[5.699, \infty)$ where the topological entropy is $\ln(2)$. The black and magenta regions denote the k intervals $[5.194, 5.5366]$ and $[4.5624, 4.5931]$ respectively, which are both hyperbolic plateaus with topological entropy $\ln(1.969)$ and $\ln(1.895)$ respectively. The green region denotes the interval $[4.1930, 4.201]$ found using HLD has and is an estimate for the interval where the inner region is fully hyperbolic. The topological entropy for this k interval is exactly half the entropy as the k interval [4.5624, 4.5931], $\ln(1.895)/2$. See Sect. 3.7 for more discussion on this interval.

where

$$M_p = \left. \frac{\partial f^{n_p}}{\partial x} \right|_{x_*}, \tag{3.14}$$

n_p is the period of x_*, and λ_p is the greater eigenvalue of M_p. The escape rate γ is computed by first computing all periodic orbits up to period n and computing the trace coefficients C_n using Eq. (4.15). Then the coefficients Q_n are computed using Eq. (3.10). The escape rate γ is then computed by finding the roots of the polynomial in Eq. (3.5).

One consequence of the spectral determinant for computing γ is that escape from a given region only depends on the periodic orbits in that region, and adding or subtracting regions that have no periodic orbits in them does not change the escape rate.

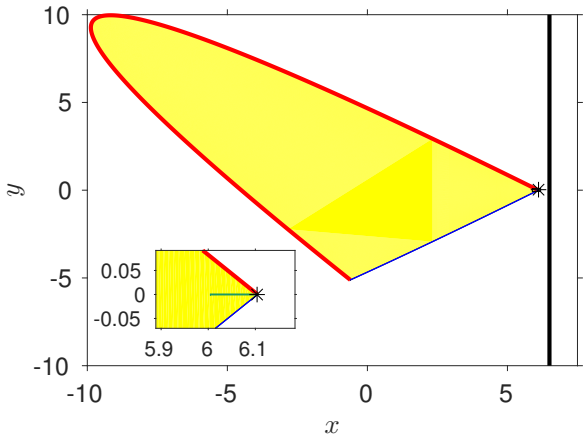

Figure 3.2. The resonance zone (yellow) for $k = 10$. The asterix marks the location of the fixed point whose stable (red) and unstable (blue) manifolds bound the resonance zone. The detection line used to define escape for Monte Carlo is shown in black. The initial ensemble of points for Monte Carlo is shown in green.

3.3 The area-preserving Hénon map

Our model of choice for computing escape rates is the Hénon map [38], given by

$$\begin{aligned} x_{t+1} =& y_t - k + x_t^2, \\ y_{t+1} =& -bx_t. \end{aligned} \tag{3.15}$$

where k and b are parameters of the map. In the figures, we rotate the coordinates (x, y) by 45 degrees in the counter-clockwise direction so that the symmetry axis is the horizontal axis. We define $M(x_t, y_t)$ as the map which evolves a point $\mathbf{x}_t = (x_t, y_t)$ forward to the point $\mathbf{x}_{t+1} = (x_{t+1}, y_{t+1})$. Although the techniques discussed throughout this paper are valid for maps that are not area-preserving, we set $b = 1$ to connect with Hamiltonian dynamical systems where area is preserved in phase space. Given $b = 1$, the map defined by Eq. (3.15) can exhibit a variety of chaotic phase spaces ranging from a full binary horseshoe at $k > 5.699$ to having a mixed phase space with stable islands embedded in a chaotic sea at lower k values.

Figure 3.1 shows the topological entropy of the Hénon map computed over a wide range of parameter value using symbolic dynamics computed from HLD. The rightmost shaded region denotes the interval $k \in [5.699, \infty)$ where the dynamics exhibits a full horseshoe with topological entropy of $\ln(2)$. Escape rates for $k \in [5.699, \infty)$ are computed using periodic orbits in Sect. 3.5. As k is lowered, the topological entropy decreases monotonically. This decrease is not *strictly*

monotonic because of the existence of hyperbolic plateaus, which are intervals of k where the dynamics is hyperbolic and the topological entropy does not change. The black and magenta shaded regions denote the intervals of k which Arai identified to be hyperbolic plateaus [3], namely $k \in [5.194, 5.5366]$ and $k \in [4.5624, 4.5931]$ for which we compute escape rates in Sect. 3.6. The green shaded band denotes an interval of k where a subregion of phase space exhibits exactly half the entropy as the plateau shown in magenta, and escape rates are computed in this interval in Sect. 3.7. In this case, the subregion exhibits a hyperbolic plateau when treated as its own dynamical system. See Sect. 3.7 for more discussion on this interval.

3.4 Monte Carlo Computation of Escape Rate γ

Throughout this study, we compute the escape rate γ using a Monte Carlo method to compare with the value obtained from periodic orbits. The phase portrait for $k = 10$ is shown in Fig. 3.2. The resonance zone (yellow) is bounded by the stable and unstable manifolds of a hyperbolic fixed point, and contains all of the periodic orbits in the system. Escape from the resonance zone is defined by leaving the zone and entering the unbounded white region. Equivalently, escape can be defined as passing to the right of the detection line shown in Fig. 3.2. Since the escape rate does not depend on the initial conditions within the resonance zone, the initial points are chosen within the resonance zone near the fixed point, shown in green in Fig. 3.2.

Figure 3.4 shows the number of surviving trajectories along with the fit line whose slope gives the approximation to the escape rate. Depending on available computational resources at the time of study, the Monte Carlo simulations were computed in parallel using the Message Passing Interface (MPI) [62] on the Multi-Environment Research Computer for Exploration and Discovery (MERCED), or on an NVIDIA GTX 970 graphics processing unit using the Compute Unified Device Architecture (CUDA) [61]. Sect. 3.4.1 describes the fitting method used and the choice of error bounds based on the goodness of fit.

In the case of a multiexponential escape rate as in Eq. 4.2, choosing an initial ensemble just outside the resonance zone is more suitable for detecting multiple exponential escape rates. After iterating the initial points forward they enter the resonance zone before escaping past the detection

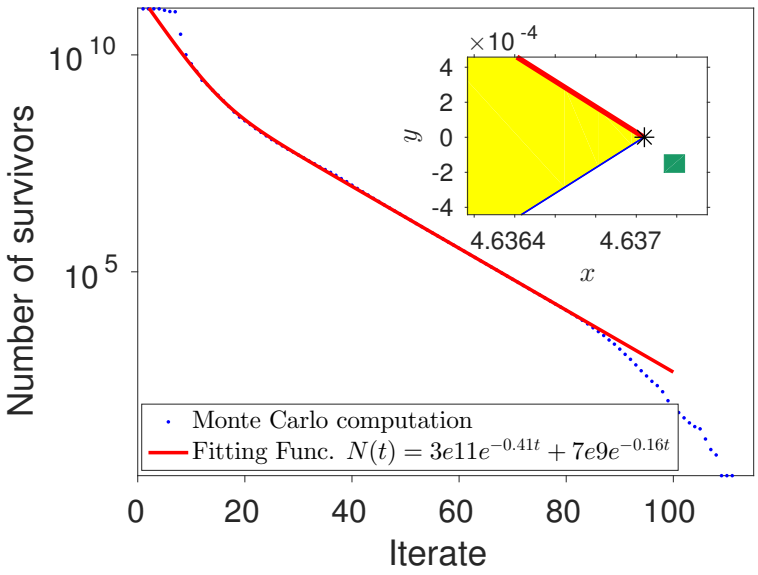

Figure 3.3. The number of surviving trajectories as a function of iterate for $k = 4.1933$, using initial points outside the resonance zone. The fit interval is computed by taking a log of the data and first fitting to the interval starting at iterate 52 and ending at iterate 80 to compute the asymptotic escape rate, then subtracting the resulting fitting function from the data and fitting to the interval starting at iterate 13 and ending at iterate 24 to compute the short-time escape rate. Inset: The phase portrait near the fixed point for $k = 4.1933$. The asterix marks the location of the fixed point whose stable (red) and unstable (blue) manifolds bound the resonance zone. The initial ensemble of points for Monte Carlo is shown in green. The method of computing the fitting function is described in Appendix A.

line. For $k = 4.1933$, the escape curve is biexponential as in Fig 3.3, exhibiting a fast, initial escape rate and then a slow, asymptotic escape rate. Starting the initial points outside the resonance zone gives more time for transients to expire before the points begin to escape, allowing for more accurate observation of the fast, initial escape rate. Such a computation of escape mimics the scattering of electrons from nuclei in chaotic atomic systems, as studied in Refs. [56, 75]. We compute the two escape rates for $k = 4.1933$ using periodic orbits and using a more accurate Monte Carlo method that targets individual resonance zones in Sect. 3.7.

3.4.1 Choosing appropriate fit intervals and error bounds for Monte Carlo escape rates

Once the Monte Carlo data shown in Fig. 3.4 (blue) is computed by counting the number of surviving trajectories as a function of time, the escape rate is computed by fitting a line to the log of this data. The error bars used in the figures are the 95% confidence intervals computed from the fit.

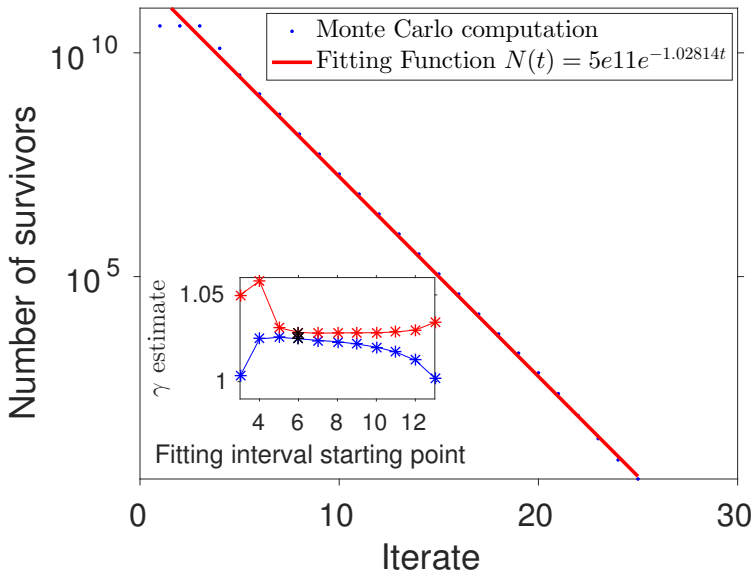

Figure 3.4. The number of surviving trajectories as a function of iterate (blue) for $k = 10$. The fitting function (red) is fit to the iterate interval $[11, 20]$. The escape rate computed from this fit is 1.02814 ± 0.00071. Inset: The escape rate upper (red) and lower (blue) bounds as a function of fit interval. The end point of the fit interval is 20 iterates. The error bounds chosen for comparison with periodic orbits are shown in black.

The starting and ending iterates for the fit interval must however be carefully chosen to obtain an accurate bound on the escape rate. If the starting iterate of the fit interval is too low, the transients will not have expired, and correlated trajectories that escape in the first several iterates will provide an inaccurate result for the escape rate. If the starting iterate of the fit interval is too high, there will be too few points remaining in the simulation to properly sample the phase space and resolve the true asymptotic escape rate of the system. The fit is computed over every possible starting and ending point value, and the starting and ending point with the tightest confidence interval is chosen. The inset of Fig. 3.4 shows the escape rate upper and lower bounds computed as a function of the starting point of the fit interval by fixing the ending point of the fit interval at 25. The escape rate estimates are wider first few iterates, then they level off and remain flat, but at even later iterates the error bars eventually grow large when the remaining number of surviving trajectories is low. The smallest error bounds shown in black are chosen. This technique is used for computing all Monte Carlo escape rates in Sects. 3.5-3.7.

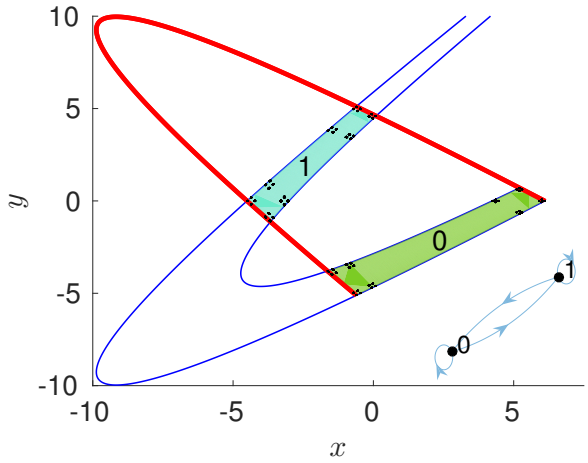

Figure 3.5. k=10 partitions. The periodic orbits up to period 13 are plotted in black. The symbolic dynamics (inset) is a full shift on two symbols.

In the case of the scattering problem studied in Fig. 3.3, the bi-exponential escape rate is computed by first fitting an exponential to the later iterates to extract the asymptotic decay, then subtracting that fit function from the data, and finally fitting to the earlier iterates of the data to compute the initial decay.

3.5 Hénon Escape For Full a Shift on Two Symbols

We first demonstrate the spectral determinant technique for the k range where the dynamics is a full binary horseshoe, $k > 5.699$. The dynamics can be encoded using two symbols denoted $\mathbf{0}$ and $\mathbf{1}$, whose corresponding partition elements are shown for $k = 10$ in Fig. 3.5. The symbolic dynamics transition graph is shown in the inset of Fig. 3.5. All periodic orbits in the system consist of points lying in region $\mathbf{0}$ and region $\mathbf{1}$, and the symbolic itinerary of any period-N orbit is a binary string of length N.

3.5.1 Periodic orbit computation of γ

An accurate partitioning of the phase space and corresponding symbolic dynamics allows for characterizing and computing periodic orbits in order to compute γ from the spectral determinant. The symbolic dynamics is used to compute a symbolic itinerary for a given periodic orbit. The symbolic itinerary along with the corresponding partitions are used to construct a seed. The seed is

Period	Cumulative number of orbits	γ
1	2	1.1989476364
2	3	0.99036961
3	5	1.0371111058
4	8	1.0274997079
5	14	1.0278413650
6	23	1.0279897430
7	41	1.0280053653
8	71	1.0280053619
9	127	1.0280053745
10	226	1.0280053736
11	412	1.0280053736
12	747	1.0280053734
13	1337	1.0280053742
Monte Carlo		1.02814 ± 0.00071

Table 3.1. The cumulative number of periodic orbits used up to the given period and the value of γ computed from the spectral determinant up to that period for $k = 10.0$. The error bound for the Monte Carlo method is computed using the 95% confidence interval from the fit.

then used in a multi-shooting Newton's method to compute the periodic orbit. Appendix A explains how to generate accurate seeds using the boundaries of the partitions and compute periodic orbits, which are shown for $k = 10.0$ in black in Fig. 3.13. Once the periodic orbits are computed, the greater eigenvalue of each orbit λ_p is computed by using an analytic formula for the linearization of the Hénon map derived from Eq. (3.15). The values of λ_p and their corresponding periods are used to construct the spectral determinant and find the zeros of Eq. (3.5). The escape rate computed from periodic orbits becomes more accurate as higher periodic orbits are used, as shown in Fig. 3.6 and Table 3.2.

3.5.1.1 Periodic orbit continuation

Once periodic orbits are computed for a given value of k, they can be used as seeds for computing orbits for a nearby k value, because a small change in k results in a small change in the locations of the periodic orbits. Thus, k can be varied iteratively and periodic orbits can be computed over a range of parameter value, which is a technique known as periodic orbit

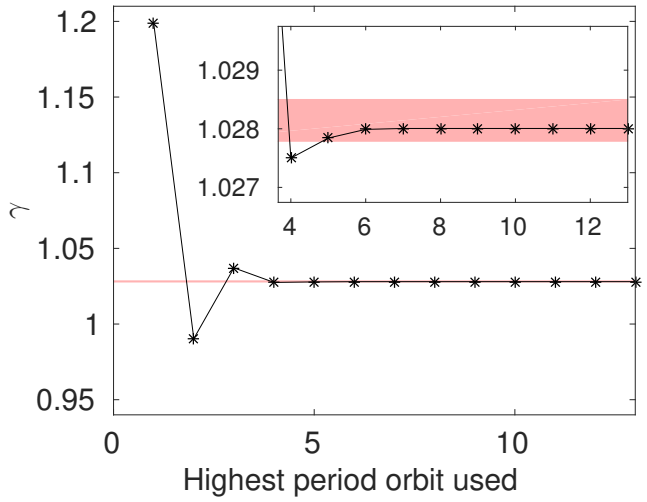

Figure 3.6. Escape rate vs. period for $k = 10$ using the spectral determinant (black). The red band is the Monte Carlo confidence interval 1.02814 ± 0.00071. Due to strong hyperbolicity for this k value, periodic orbit escape rate is computed with high accuracy, and the periodic orbit escape rate converges exponentially to the Monte Carlo value as a function of period.

continuation. Figure 3.7 shows the escape rate as a function of k for the interval [5.1, 10.0] using both Monte Carlo and periodic orbit methods. Periodic orbits disappear or become stable in a bifurcation below $k = 5.699$ are removed from the spectral determinant computation.

3.6 Computing Periodic Orbits over Hyperbolic Plateaus with HLD

As k is lowered, the Hénon system no longer exhibits a binary symbolic dynamics. When k is less than 5.699, the topological entropy begins to fall below $\ln(2)$ as periodic orbits become stable or are lost in bifurcations, and the new symbolic dynamics for any given k value can require tens or hundreds of symbols in order to characterize and compute periodic orbits. We employ a technique called Homotopic Lobe Dynamics [53, 54] (HLD) to compute the system's symbolic dynamics and the corresponding partitioning scheme. This automated technique uses information encoded in the intersections of finite-length segments of stable and unstable manifolds of periodic orbits to compute symbolic dynamics and a corresponding partitioning scheme. In the HLD technique, the stable and unstable manifolds of the anchor periodic orbit are first computed up to a primary intersection point. Then the unstable manifold is iterated forward for a finite number of iterates, and

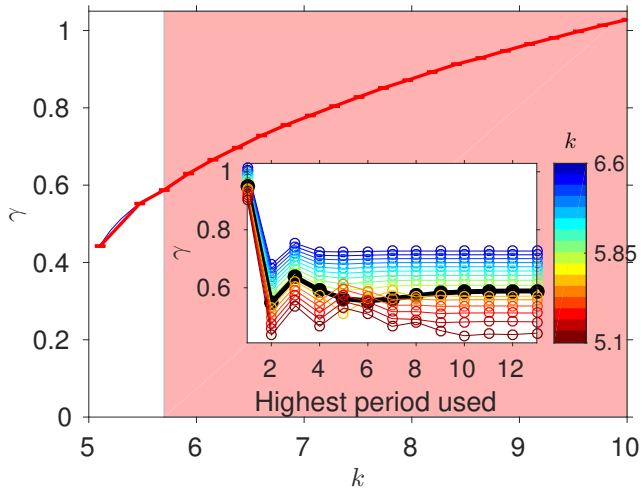

Figure 3.7. The Monte Carlo (red) and spectral determinant (blue) escape rates as a function of k for $k \in [5.1, 10]$. The two curves lie almost on top of each other. Above $k = 5.699$ (the red interval), the symbolic dynamics is a full shift on two symbols and all periodic orbits up to period 13 are used in the computation of γ. As k is lowered past 5.699, periodic orbits that disappear or become stable in a bifurcation are removed from the spectral determinant computation. Inset: The spectral determinant escape rate computed as a function of period for the k range [5.1,6.6], specified by the colorbar. The escape rate for the bifurcation point, $k = 5.699$, is plotted in black.

the symbolic dynamics is computed from the intersections of the stable and unstable manifolds. The finite-length segments of stable and unstable manifolds used for computing HLD are known as a **trellis**, and the trellis for $k = 5.4$ is shown in Fig. 3.8a. The resulting symbolic dynamics computed from HLD is shown in Fig. 3.8b and the corresponding partitioning scheme computed from HLD is shown in Fig. 3.8c. The periodic orbits are computed from the partitioning scheme as in Sect. 3.5 and as described in Appendix A, and are shown in Fig. 3.9.

3.6.1 Escape rate over hyperbolic plateaus

We now focus on two fully hyperbolic intervals of k whose rigorous bounds were identified by Arai [3], namely $k \in [5.194, 5.5366]$ and $k \in [4.5624, 4.5931]$. Such hyperbolic intervals of k are useful for computing escape rates from periodic orbits because no orbits are lost or created in bifurcations as k is varied over the interval. Once periodic orbits are computed for a given k value within a hyperbolic plateau, they can be computed for the entire interval using periodic orbit continuation. Figure 3.10 shows the escape rate as a function of the highest period orbit used using the spectral determinant for $k = 5.4$, chosen near the center of the hyperbolic plateau. The

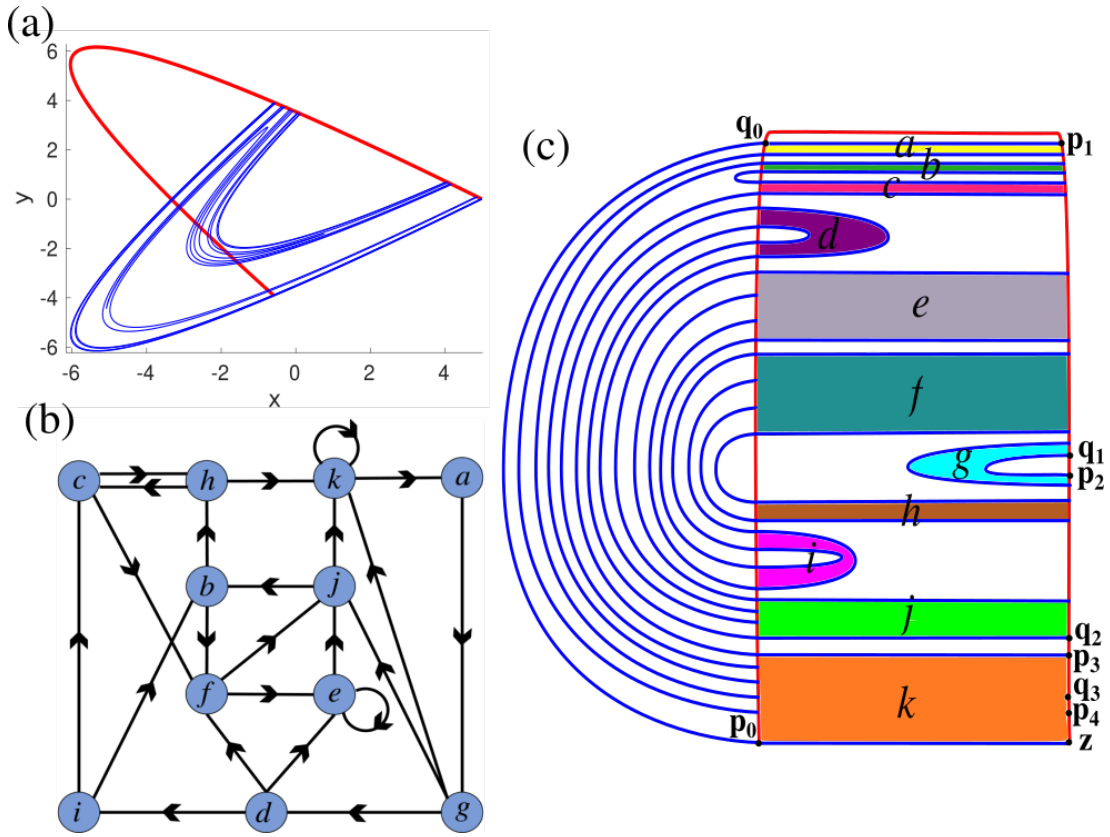

Figure 3.8. (a) The trellis for $k = 5.4$. (b) The transition graph computed from HLD. (c) The corresponding partitions.

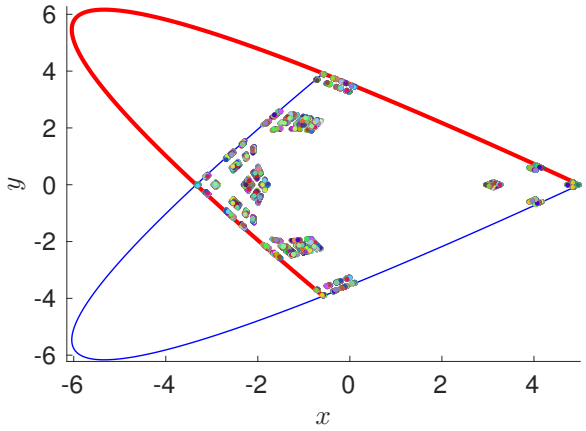

Figure 3.9. All periodic orbits up to period 13 for $k = 5.4$.

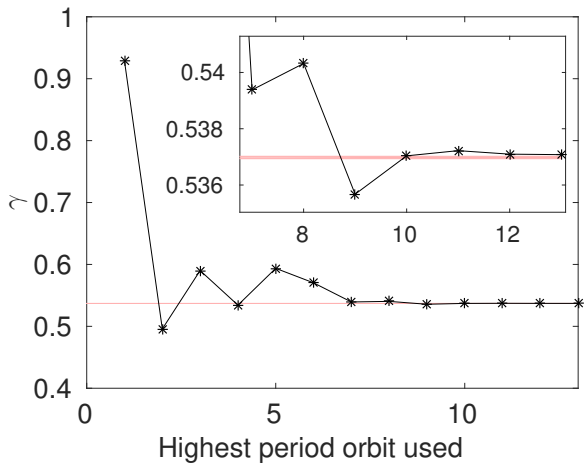

Figure 3.10. Escape rate versus period for $k = 5.4$ computed from periodic orbits (black) and Monte Carlo (red band).

escape rate is then computed for an interval of k that spans $k \in [5.194, 5.5366]$ using periodic orbit continuation, shown in Fig. 3.11a. The same process is used to compute the escape rate for an interval that spans $k \in [4.5624, 4.5931]$. The periodic orbits are first computed for $k = 4.575$ using HLD, then periodic orbit continuation is used to compute the escape rate over the entire interval, shown in Fig. 3.11b. For both hyperbolic plateau intervals, the escape rate computed from periodic orbits accurately predicts the Monte Carlo escape rate within the hyperbolic plateau. As k is lowered below the hyperbolic plateau bound, periodic orbits that become stable or are lost in a bifurcation begin to distort the periodic orbit computation of γ, and the periodic orbit estimate begins to vary from the true value. As k is increased above the hyperbolic plateau bound, orbits that exist at the higher k value are not accounted for, and therefore the periodic orbit estimate of the escape rate becomes less accurate.

3.7 Computing Multiexponential Escape With Nested Zones

For the k values studied in Sects. 3.5 and 3.6, the escape dynamics exhibits a single exponential escape rate as in Eq. (4.1). As k is lowered below 4.28 the phase space can exhibit multiexponential escape rates as in Eq. (4.2) and as shown for $k = 4.1933$ in Fig. 3.3. The inset of Fig. 3.12 shows the phase portrait at $k = 4.1933$ which exhibits three distinct zones, namely Zone 0 (white), Zone I (yellow), and Zone II (red). The period-2 inner structure arises from the stable and unstable

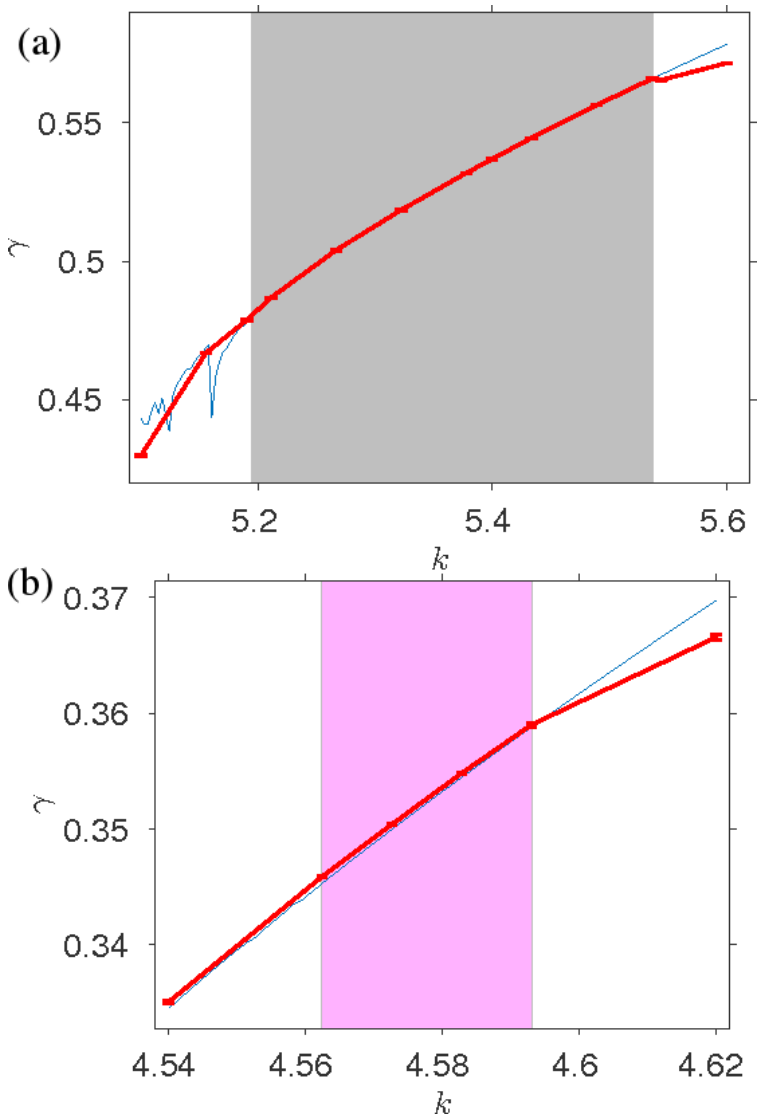

Figure 3.11. Escape rates computed using the spectral determinant (blue) and Monte Carlo escape rate (red) versus k for (a) $k \in [5.1, 5.6]$ and (b) $k \in [4.54, 4.62]$. The shaded intervals denote the hyperbolic plateaus [5.194,5.5366] (grey) and [4.5624, 4.5931] (magenta).

manifolds of an inner fixed point with inversion which lies at the center of Zone II. All periodic orbits within Zone II, except for the fixed point, have a periodicity which is a multiple of two. Although the inner period-two structure in Zone II persists at greater k values, at $k > 4.28$, the boundary of Zone II intersects the boundary of Zone I, and therefore the phase space always exhibits single-exponential escape rates for $k > 4.28$. For $k < 4.28$, there exist intervals of k which exhibit multiexponential escape rates.

3.7.1 Finding an inner hyperbolic plateau

None of the hyperbolic plateaus for the Hénon map noted in previous work [3, 25] are below $k = 4.28$ where multi-exponential escape rates can be observed, so therefore a search for hyperbolic plateaus exhibiting multi-exponential decay was done using HLD. A hyperbolic plateau can be found using HLD by computing the symbolic dynamics as a function of k and finding intervals of k where the symbolic dynamics does not change. The inner red zone in Fig. 3.12, Zone II, can be treated as its own dynamical system which exhibits its own hyperbolic plateaus. When Zone II is viewed under the Hénon map composed with itself, M^2, there are intervals of k where the topology of Zone II related to the topology of the full phase space for the hyperbolic plateaus studied in Sect. 3.6. For example, at $k = 4.3$ under M^2, the bottom half of Zone II has the same exact transition matrix as the full phase space for the wider hyperbolic plateau studied in Sect. 3.6, $k \in [5.194, 5.5366]$. Furthermore the manifolds and partitions of the system have the same topology which is shown in Fig. 3.8. Under the singly composed map M, the topological entropy of Zone II at $k = 4.3$ is equal to $(1/2)\ln(1.969)]$, which is exactly half of the topological entropy of the full phase space for $k \in [5.194, 5.5366]$.

Since the escape is only single-exponential at $k = 4.3$, this k value cannot be used to study multiexponential escape rates using nested zones. Instead to find a k value where Zone II exhibits a hyperbolic plateau and the escape rate is multiexponential, a binary search in HLD was done below $k = 4.28$ to find the value of k for which Zone II has exactly half the entropy as $k \in [4.5624, 4.5931]$, the lower hyperbolic plateau studied in Sect. 3.6. The interval $k \in [4.1930, 4.201]$ was found to have exactly half the topological entropy as $k \in [4.5624, 4.5931]$, and the bottom half of Zone II under M^2 has the same transition matrix as $k \in [4.5624, 4.5931]$

under M. The topology of the inner zone remains the same over this interval and therefore there are no bifurcations in periodic orbits within the inner zone. The symbolic dynamics at $k = 4.1933$, near the center of the plateau, is used to compute the trellis and partitions using HLD to compute periodic orbits.

3.7.2 Monte Carlo computation for nested zones

Unlike in Sects. 3.5 and 3.6 where a detection line is used to define escape for computing γ from the full resonance zone, the escape criterion for computing γ_I, γ_{II}, and $\gamma_{I,II}$ is chosen based on the boundaries of individual resonance zones. The initial points are chosen to be uniformly distributed in a particular zone, and the escape rate is defined as entering a different zone. The zone of a particular point is obtained using a point-in-polygon test. As points are mapped forward, their zone is computed and the number of surviving trajectories is counted as a function of iterate. The different escape rates for different zones can be computed by choosing the appropriate Zones for the initial ensemble of points and escape criterion. For phase spaces such as the one shown in the inset of Fig. 3.12, three distinct escape rates can be computed as summarized in Table II: escape from Zone I, escape from Zone II, and escape from the union of Zones I and II, labeled as γ_I, γ_{II}, and $\gamma_{I,II}$ respectively. The escape rate γ_I is computed by choosing the initial points in Zone I and defining escape as entering Zones II or 0. The escape rate γ_{II} is computed by choosing initial points in Zone II defining escape as entering Zones I or 0. The escape rate $\gamma_{I,II}$ can be computed by choosing initial points in the union of Zone I and Zone II and defining escape as entering Zone 0, but since Zone II has ultimately the slowest escape rate, the result will be dominated by the points starting in Zone II. Therefore $\gamma_{I,II}$ is computed more accurately by choosing initial points in Zone II and defining escape as entering Zone 0. The Monte Carlo curves for γ_I, γ_{II}, and $\gamma_{I,II}$, including the two different ways of computing $\gamma_{I,II}$, are shown in Fig. 3.12 and in Table II.

3.7.3 Nested trellis

An important advantage of the HLD technique is the ability to target individual regions of phase space by including the stable and unstable manifolds of additional periodic orbits, creating a nested trellis [54]. This technique can be used to target Zones I and II in the inset of Fig. 3.12. To

	Starting Zone, Escape Zone	Spect. det.	MC
γ_I	I, 0 $\cup$ II	0.3781	0.35823 $\pm$ 5e-5
γ_{II}	II, 0 $\cup$ I	0.18039	0.18245 $\pm$ 3e-5
$\gamma_{I,II}$	II, 0	0.16512	0.16406 $\pm$ 2e-5

Table 3.2. Summary of the three escape rates γ_I, γ_{II}, and $\gamma_{I,II}$ along with the periodic orbit and Monte Carlo escape rate computations for $k = 4.1933$.

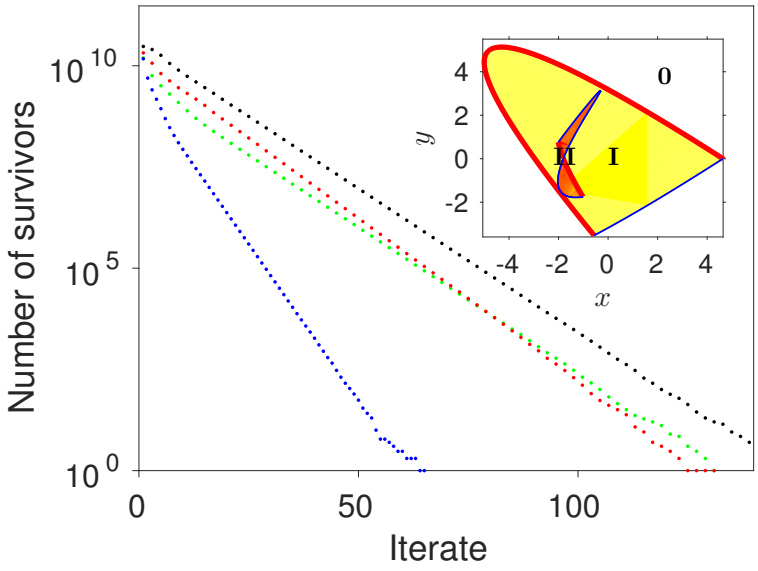

Figure 3.12. Monte Carlo escape rates for different zones for $k = 4.1933$. The initial points are chosen uniformly from the starting zone, and escape occurs when a point enters the escape zone. In green, the Monte Carlo escape rate for $\gamma_{I,II}$ is computed using Zone II as the starting zone and the union of Zone I and Zone 0 as the escape zone . In black, a different computation for $\gamma_{I,II}$ is computed using initial points in Zone II and defining escape as entering Zone 0. The green and black lines are parallel, but the black line yields a better estimate for the value γ_I, because the Monte Carlo for the green data includes points in the outer zone, which have a faster initial escape, while the black line levels off more quickly. In blue, the Monte Carlo escape rate for γ_I is computed, using initial points distributed uniformly in Zone I and defining escape as entering Zone II or Zone 0. In red, the Monte Carlo escape rate γ_{II} is computed using initial points distributed uniformly in Zone II and defining escape as entering Zone II or Zone 0. Inset: The two resonance zones. We denote the unbounded white region as Zone 0, the bounded yellow region as Zone I, and the inner bounded red region as Zone II. Because Zones I and II disconnected, i.e. the manifolds bounding them do not intersect each other, the two resonance zones have separate escape rates.

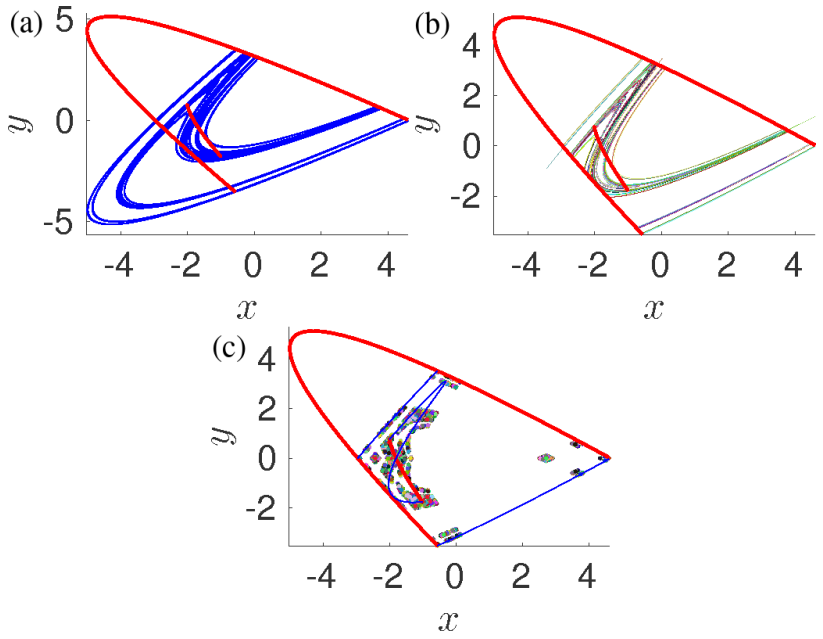

Figure 3.13. (a) Full trellis for $k = 4.1933$. (b) The partitions for $k = 4.1933$. (c) All periodic orbits for $k = 4.1933$.

target the Zone I, the stable and unstable manifolds of the same outer fixed point are used as they were in Sects. 3.5-3.6. To target Zone II, the stable and unstable manifolds of the the inner fixed point with inversion are also included. The resulting tangle is shown in Fig. 3.13a. The additional heteroclinic intersections included in the nested trellis lead to a better sampling of the topology of phase space, compared to using the outer trellis alone. Using the nested trellis results in a more accurate symbolic dynamics containing 351 nodes and 645 edges. The corresponding partitioning computed from HLD is shown in Fig. 3.13b. The periodic orbits computed from the partitions are shown in Fig. 3.13c. From the nested trellis, three different transition matrices are obtained. T_I is the transition matrix for Zone I, T_{II} is the transition matrix for Zone II, and $T_{I,II}$ is the transition matrix for Zones I and II. The transition matrix $T_{I,II}$ contains all the nodes and edges in T_I and in T_{II} , but it also contains additional edges that connect Zones I and II. It does not contain any additional nodes, as all nodes lie in either Zone I or Zone II. The topological entropies of T_I, T_{II}, and $T_{I,II}$ are $\ln(1.8311)$, $\ln(1.3766)$, and $\ln(1.8390)$ respectively. The topological entropy of Zone II at $k = 4.1933$ is exactly half of that of the the full phase space at $k \in [4.5624, 4.5931]$, and the symbolic dynamics of M^2 on the bottom half of Zone II is isomorphic to the symbolic dynamics of the full resonance zone for $k \in [4.5624, 4.5931]$.

3.7.4 Periodic orbits and spectral determinants for nested zones

To compute the escape rate from a given zone using the spectral determinant, we include only periodic orbits from that zone. The escape rate γ_I is the escape from Zone I, and therefore γ_I is computed using periodic orbits that lie only in Zone I, computed from T_I. The escape rate γ_{II} is the escape rate from Zone II, and therefore γ_{II} is computed using only periodic orbits that lie only in Zone II, computed from T_{II}. The escape rate $\gamma_{I,II}$ is the escape rate from both zones, and therefore $\gamma_{I,II}$ is computed using all periodic orbits, computed from $T_{I,II}$. The three distinct escape rates computed with periodic orbits and Monte Carlo simulation are shown in Fig. 3.14 and Table II. Targeting the inner region and capturing the full topology using HLD allows for computing all periodic orbits up to period 20, which yields an accurate value for the escape rate γ_{II} (red). Using the nested trellis approach with the stable and unstable manifolds from both resonance zones also yields an accurate result of the escape rate $\gamma_{I,II}$ (black), even though our computation of HLD has not extracted the exact symbolic dynamics and some periodic orbits may be missing from the computation. The outer escape rate γ_I (blue) is the least accurate, which means some periodic orbits are missing form the HLD computation, or more orbits of higher period are required to accurately obtain the escape rate. Figure 3.15 shows the escape rates computed as a function of k using periodic orbits using periodic orbit continuation, along with the corresponding Monte Carlo escape rates. The inner escape rate γ_{II} is computed accurately over the entire interval. The escape rate for both zones, $\gamma_{I,II}$, is computed most accurately at the k value where HLD is computed, $k = 4.1933$, and captures part of the variation in escape rate as k is varied. The escape rate from the outer zone γ_I is computed less accurately over this k range, but still yields a close result and captures some of the variation as k is varied. The escape rates γ_I, γ_{II}, and $\gamma_{I,II}$ are easily distinguishable and detectable from both the periodic orbit and Monte Carlo escape rate computations.

3.8 Comparison with periodic orbit continuation from the full horseshoe

Due to the monotonic nature of periodic orbits in the Hénon map as k is varied, the periodic orbits found at $k = 10$ can be continued downward and computed for all of the different k values

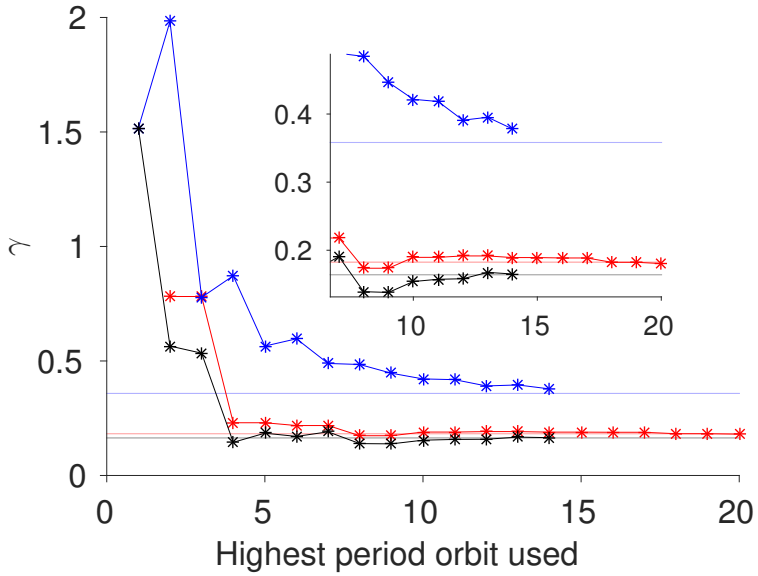

Figure 3.14. The periodic orbit and Monte Carlo computations of γ_I (blue), γ_{II} (red) and $\gamma_{I,II}$ (black) using periodic orbits (lines with star markers) and Monte Carlo (horizontal bands) for $k = 4.1933$.

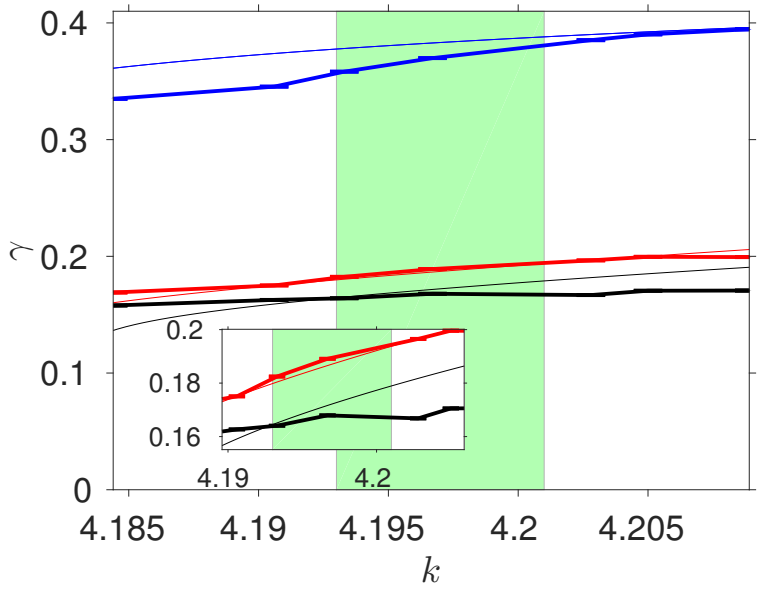

Figure 3.15. The escape rates γ_I (blue), γ_{II} (red), and $\gamma_{I,II}$ (black) computed as a function of k using Monte Carlo (bold with error bars) and with periodic orbits (finer line with no markers). Once the orbit becomes stable or is lost in a bifurcation, it is removed from the spectral determinant calculation for all lower k values.

studied in Sects. 3.5-3.7. This is not the case for all maps, and the HLD technique can be applied in maps where the bifurcation of periodic orbits is not monotonic. Even in cases such as the Hénon map, applying HLD still has benefits over using periodic orbit continuation. Due to the large number of orbits and difficulty in distinguishing the orbits, periodic orbits were only computed up to period 13 for $k > 5.699$, for which the symbolic dynamics is a full shift on two symbols. By computing HLD for the lower k values near 4.1933, periodic orbits were computed for one additional period, at period 14. Targeting a particular k value using HLD allows for the ability to compute all periodic orbits up to a higher period.

Another benefit of targeting a particular k value is that it requires the computation of fewer orbits up to a given period. For example at period 20, the number of periodic orbits at $k = 10$ is 110,013. On the other hand at $k = 4.1933$, the total number of periodic orbits at period 20 is only 22,857. Another way to reduce the number of periodic orbits to compute is by restricting the escape rate computation to a particular region of phase space. For computing γ_{II} in Sect. 3.7, only 143 periodic orbits up to period 20 were necessary to compute the escape rate.

3.9 Computing Multiexponential escape rates in a Mixed Phase Space

A major goal of this work is to use periodic orbits to compute multiexponential escape rates in a mixed phase space which contains stable islands embedded in a chaotic sea. The accurate computation of escape rates in such a space would be important for demonstrating that periodic orbit theory can be used to compute transport rates in realistic physical systems. Computing periodic orbits in a mixed phase space has proven difficult, because the rich dynamics near the stable islands leads to very complicated symbolic dynamics. Figure 3.16 shows the inner zone, Zone II, at $k = 3.888027$. Within Zone II lies a period-6 zone which we call Zone III. The same three decay rates defined in Sect. 3.7 can be defined for this trellis, except that The escape rate from Zone II is then defined as the rate at which trajectories leave Zone II and enter Zone I or Zone III. The escape rate γ_{III} can be defined as the escape rate from Zone III, but we did not compute that decay rate here since we have not computed periodic orbits in that Zone. The decay rates $\gamma_{I,II}$ and γ_{II} are

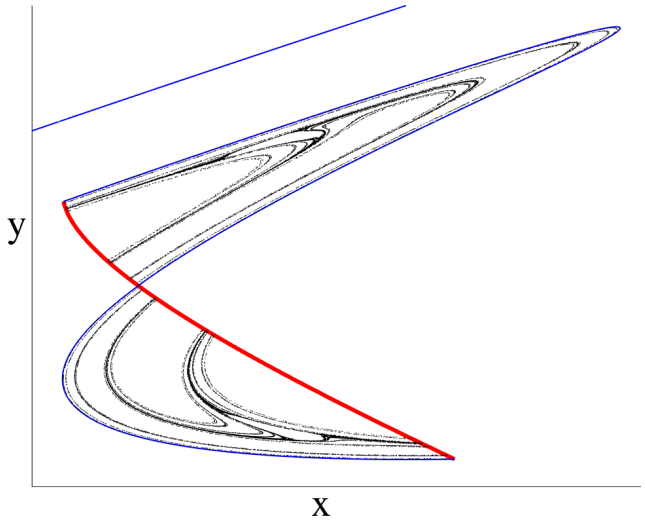

Figure 3.16. The inner Zone, Zone II at $k = 3.888027$. Inside the zone lies a stable island, which has a period-6 structure. The period-6 stable island is associated with a period-6 orbit whose manifolds bound the region. That inner region, shown as the white space within the stable island, is Zone III.

shown in Fig. 3.17. Although the escape rates computed from periodic orbits are close to the Monte Carlo values, the data does not indicate that the convergence is exponential. It may be that some periodic orbits are missing in the computation and were not found by HLD due to not having enough length of the unstable manifold in the trellis. In addition, the convergence gets worse as k is varied. It appears that in a mixed phase space, a small change in k leads to the bifurcation of low-period orbits. This leads to difficulty in computing the escape rate, since the spectral determinant goes to zero whenever the eigenvalue of a periodic orbit approaches 1. An accurate computation of all periodic orbits up to a higher period should still lead to an accurate computation of the escape rate. One way to improve the computation is by adding in more nested tangles, i.e., starting by adding in the trellis associated with the period-6 island.

3.10 Varying the spectral determinant convergence by adding or removing orbits

As a check of the convergence of the spectral determinant, we looked at how the convergence varies when including multiple copies of orbits. For example in Fig. 3.18, the escape rate convergence is shown using one copy of each orbit, two copies of each orbit, and three copies

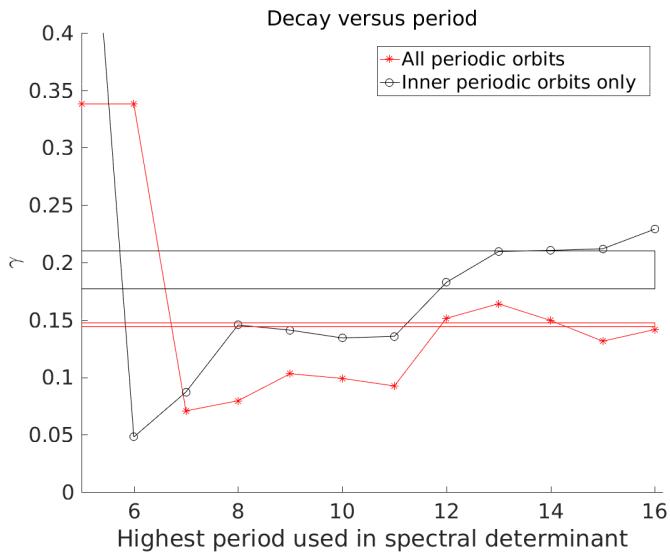

Figure 3.17. The escape rates $\gamma_{I,II}$ and γ_{II} for $k = 3.888027$ exhibiting a mixed phase space. The periodic orbit computation for $\gamma_{I,II}$ is shown in black circles, and the corresponding Monte Carlo decay rate is shown as a black band. The periodic orbit computation of γ_{II} is shown with red x markers and the corresponding Monte Carlo decay rate is shown as a red band.

of each orbit. It was found that the convergence gets worse when using multiple values, however, the escape rate converges to the same rate nonetheless. The dynamical zeta function computation, also shown in Fig. 3.18, converges more slowly than the spectral determinant.

In the case of a nested trellis with a stable period-6 island, the escape rate was difficult to compute because we did not have a full grasp on the symbolic dynamics due to the rich inner structure of the period-6 island. Figure. 3.19 shows the periodic orbit Monte Carlo escape rates at $k = 3.9$. At this k value, there is an inner period-8 orbit that is close to being stable, and the symbolic dynamics computation is missing many important orbits, and therefore does not converge very close to the true value. In an attempt to improve the convergence, we weighed the different periodic orbits by different amounts based on their contribution. We counted the period-1 inner fixed point with inversion twice, we counted the period-6 orbit bounding the resonance zone once, and we counted all other orbits in the inner zone four times–these are the most important orbits for computing the inner escape rate. However, the inclusion of orbits multiple times seemed to make the escape rate computation worse rather than better. It is our conclusion that the best way to compute escape rates from periodic orbits is to include each periodic orbit once.

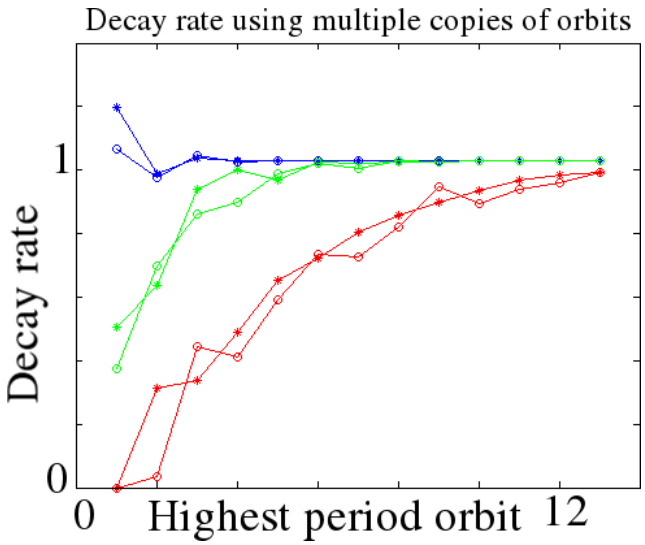

Figure 3.18. The escape rate computed using the spectral determinant (star markers) and dynamical zeta function (circle markers) as a function of highest period orbit used using a single copy of every orbit (blue), two copies of each orbit (green), and three copies of each orbit (red).

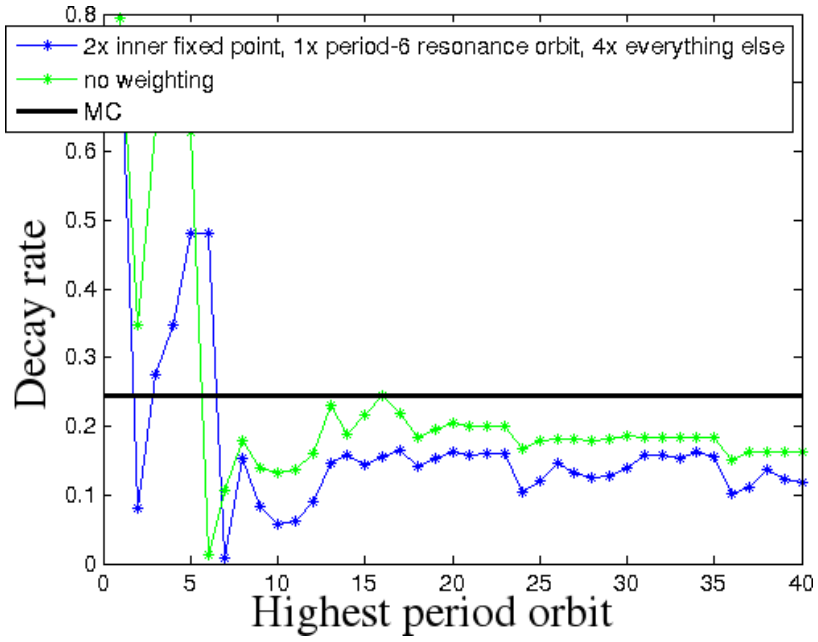

Figure 3.19. The escape rate computed with the spectral determinant (dot markers) and Monte Carlo (black line) for Zone II for $k = 3.9$. In blue, the periodic orbit is shown weighing the inner fixed point two times, the period-6 resonance orbit once, and everything else 4 times. This did not improve the convergence of the escape rate and only made it worse.

3.11 Computing periodic orbits from symbolic dynamics

The computation of periodic orbits from Newton's method requires an initial guess. The HLD technique allows for choosing an intial guess based on partitions and symbolic dynamics. Each periodic orbit has a symbolic itinerary representing it, and the initial guess for each point in a symbolic itinerary is chosen as the center of the partition with the corresponding symbol. For example, for the full shift on two symbols, every periodic orbit can be labeled using a sequence of $\mathbf{0}$'s and $\mathbf{1}$'s. The two labels correspond to the partitions shown in Fig. 3.5. The center of each partition is used as a seed. The seed points are then used in a Newton's method to solve an equation of the form

$$\begin{pmatrix} M(x_0) & = & x_1 \\ M(x_1) & = & x_2 \\ & \vdots & \\ M(x_{n-1}) & = & x_n \\ M(x_n) & = & x_0 \end{pmatrix} \tag{3.16}$$

where M is the map and x_i are coordinates of seed points in the periodic orbit of period n. For example the unknown periodic orbit whose itinerary is 010 consists of a sequence of three unknown points $p_0p_1p_2$. The Netwon's method to solve becomes

$$\begin{pmatrix} M(p_0) & = & p_1 \\ M(p_1) & = & p_2 \\ M(p_2) & = & p_0 \end{pmatrix} \tag{3.17}$$

The initial guess in Newton's method is the sequence of points $p_0p_1p_2 = s_0s_1s_0$ where s_0 is the center of partition 0 and s_1 is the center of the partition 1.

Since the partitions are bounded by segments of stable and unstable manifolds, the partitions for longer symbol strings can be computed by iterating the boundaries of the partitions forward or backward to cut the partitions into smaller portions. For example, one can look at partitions

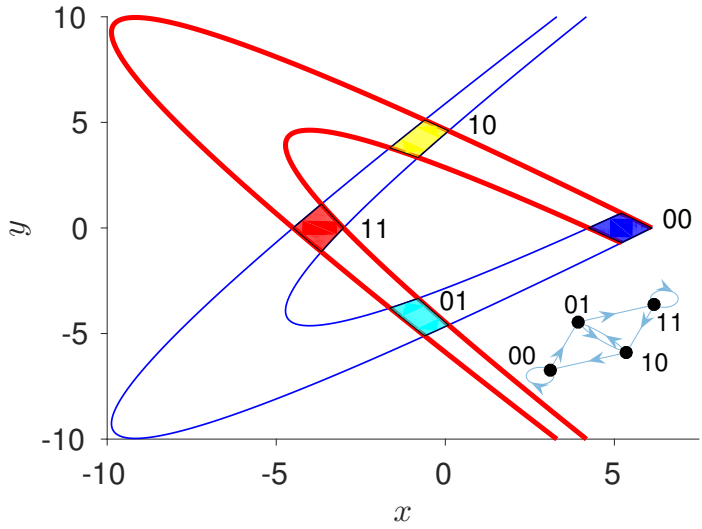

Figure 3.20. A refinement of the full shift on two symbols. The extended stable manifold (red) cuts the partitions for 0 and 1 into four new partitions representing the two-symbol strings 00, 01, 10, and 11. This symbolic dynamics generates the same periodic orbits and therefore has the same topological entropy as the full shift on two symbols, $\ln(2)$. The refined partitions give better initial guesses for periodic orbits.

corresponding to symbol strings of length two. This is done by iterating the stable manifold, whose extra intersections with the partitions cut them into peices. For the full shift on two symbols, this results in cutting the partitions 0 and 1 in Fig. 3.5 into four partitions, 00, 01, 10, and 11 in Fig. 3.20. The seed point for the period-three orbit 010 now becomes $s_{01}s_{10}s_{00}$, by looking one symbol string ahead, up to cyclic permutation, to choose a seed point based on a two-symbol string for each point in the orbit. The four-symbol symbolic dynamics is topologically forced by the new heteroclinic intersections formed by the longer stable manifold, and has the same topological entropy of $\ln(2)$. The partitions in Fig. 3.20 yield better seeds, since each seed point is chosen based on refined partitions from the four-symbol symbolic dynamics. The partitions can be refined for arbitrarily long symbol strings by iterating the stable manifold more and more times.

Refining the partitions only based on longer symbol strings requires extra computational time for iterating and cutting the manifold segments, and also requires highly accurate computations of the manifold segments to begin with. Another method to obtain better seeds from partitions is to map the partition boundaries backwards. Since the implementation of HLD computes a longer unstable manifold and a short stable manifold, partitions are typically formed using long unstable manifold segments with higher curvature and short stable manifold segments with lower

curvature. Using seed points from partition rectangles with longer manifolds and high curvature is unfavorable because the region of phase space is highly stretched after one iterate, making it less likely that Newton's method will terminate on the desired solution. Mapping the rectangles backwards balances the length of the stable and unstable segments bounding partitions and results in a partition element with less curvature, producing a better seed point for approximating the periodic orbit. The extra iterates taken are accounted for in constructing the formula for the periodic orbit solved by Newton's method.

The partitions in Fig. 3.20 are used for computing the periodic orbits used for the interval where the Henon map exhibits a full shift on two symbols. For the rest of the decay rate combinations in Chapter 3, a combination of the cutting and mapping techniques is used. The average of the inverse radius of curvature normalized by the total euclidean length of the manifold is computed for the stable and unstable segments of each partition element. Maximum tolerances for the average curvature and for the width of a partition element are chosen for both the stable and unstable manifolds. Denote the set of all partition elements as $\mathbf{\Sigma}$. A recursive algorithm is applied which terminates when the width and curvature tolerance criteria are satisfied for both stable and unstable segments for all elements of $\mathbf{\Sigma}$. For each partition element σ in $\mathbf{S}$, the partition element is first mapped backward until the diagonal width of the partition is at a minimum, and the curvature is comptued at each iterate. The number of iterates with the lowest curvature is chosen for the partition element, and the curvature and width criteria are computed for the mapped partition element. If either criteria is not satsfied in the unstable (stable) direction, then the stable (unstable) manifold is iterated to cut the unstable (stable) manifold, and new partition elements are computed based on two-symbol symbol strings by adding one symbol to the beginning or end of the symbol string for σ. Then σ is removed from $\mathbf{\Sigma}$ and replaced with the new set of partition elements for two-symbol strings whose prefix or suffix is the symbol string for σ. Then the partition elements are again mapped backward, and the algorithm is then repeated for all elements of $\mathbf{\Sigma}$ until they all satisfy the width and curvature tolerances. This algorithm generates a list of substrings which are the minimum length required to satisfy the curvature and width criteria, the seeds generated from partition rectangles corresponding to the symbol strings computed, and the number of backward iterates taken for each partition rectangle to satsify the criteria. Then for a given symbol in a given

symbolic itinerary for a periodic orbit, the seed is chosen based on the substring which matches the periodic itinerary for the largest number of iterates.

3.12 Concluding Remarks

We have learned from this study that single-exponential and multi-exponential escape rates can be reliably computed using periodic orbits from HLD in lieu of a Monte Carlo simulation requiring tens of billions of orbits. We demonstrate that the result of HLD is very accurate within hyperbolic plateaus where no periodic orbits become stable or are lost in a bifurcation over a range of parameter value. We also compute distinct escape rates from different resonance zones using periodic orbits for a parameter range exhibiting multiexponential escape rates.

3.13 Acknowledgments

The authors acknowledge the support of the U.S. National Science Foundation under Grant No. PHY-1408127 and the East Asia and Pacific Summer Institutes (EAPSI). Monte Carlo simulations were computed on the Multi-Environment Research Computer for Exploration and Discovery (MERCED), which is supported by the National Science Foundation Grant No. ACI-1428783. We gratefully acknowledge discussions with Zin Arai, Tamiki Komatsuzaki, Mikito Toda, and Hiroshi Teramoto.

Chapter 4

Computing ionization rates in a chaotic Rydberg atom using periodic orbits

4.1 Overview

A classical hydrogen atom can be modeled as an electron orbiting a nucleus. The electron is a negatively charged point-mass under the influence of the electric field generated by a stationary proton. The electron's dynamics can be described by a Hamiltonian, and, to make the system chaotic, one can add an external field by adding an extra term to the Hamiltonian. The hydrogen atom in external fields can also be studied experimentally, and the ionization of the atom can be measured by placing a detector sufficiently away from the nucleus so that the electron is detected once it reaches a certain distance from the nucleus. Using the system's Hamiltonian, a Monte Carlo simulation launching millions of orbits can be used to compute the same ionization rate by measuring when each simulated electron passes a given distance from the nucleus. The number of survivors as a function of time can be of the form

$$N(t) = N_0 e^{-\gamma t}, \tag{4.1}$$

where $N(t)$ is the number of surviving trajectories as a function of time, N_0 is a constant, and γ is the asymptotic escape rate. Instead of running a Monte Carlo simulation launching millions of orbits, a sum over tens or hundreds of properly chosen periodic orbits can accurately compute the ionization rate using a formula called the spectral determinant, described in Chapter 3. A firm grasp of the structure of the periodic orbits is required to obtain accurate the ionization rate using the spectral determinant. One way to understand the structure of the periodic orbits is using the system's symbolic dynamics. In a Hamiltonian phase space, the symbolic dynamics can be represented by a set of distinct regions of phase space, the nodes, and the allowed transitions between them in time, the edges. Once the system's symbolic dynamics is known and a symbol is assigned to each node, periodic orbits can be detected by looking for cycles in the graph. The location of the periodic orbits can be found by searching in the regions of phase space associated with each symbol in the symbol sequence. *We wish to compute escape rates in a classically chaotic atomic system from the spectral determinant by computing periodic orbits using improved methods of computing symbolic dynamics*. The ability to systematically compute symbolic dynamics, partitions, and periodic orbits allows for applying periodic orbit theory to a broad range of physical applications, including studying the role of periodic orbits in quantum chaos in a real physical system, which is a future goal of this work.

One challenge we wish to address is computing escape rates in a mixed Hamiltonian phase space, where stable islands are embedded in a chaotic sea. The rich fractal structure of escape dynamics near the stable islands leads to two complications in computing the spectral determinant. The first complication is that the symbolic dynamics becomes very complex, requiring hundreds of symbols, and more complicated periodic orbits are necessary to converge to the true escape rate. The second complication is that the system no longer exhibits a single exponential escape rate as in Eq. (4.1), but rather a multiexponential escape rate given by

$$N(t) = N_0 e^{-\gamma_0 t} + N_1 e^{-\gamma_1 t} + N_2 e^{-\gamma_2 t} + ..., \tag{4.2}$$

where N_0, N_1, N_2 are constants and $\gamma_0, \gamma_1, \gamma_2$ are different escape rates representing different regions of phase space. When the number of terms in Eq. (4.2) is infinite, the resulting curve is an algebraic escape rate.

We address these two complications by using a technique called homotopic lobe dynamics [53, 54] (HLD), which uses the topological forcing by intersections of stable and unstable manifolds of a few anchor orbits to compute symbolic dynamics and partition the phase space. Using HLD, an arbitrarily accurate partition of phase space can be computed by incorporating longer and longer segments of the stable and unstable manifolds of anchor orbits. Moreover, the periodic orbits are identified by which region of phase space they occur in, and the distinct escape rates γ_i in Eq. (4.2) can be computed by computing the spectral determinant using only periodic orbits that lie in the region from which escape is being computed from. The HLD technique can be used to specifically target the symbolic dynamics of a given region to search for periodic orbits in that region. Once the periodic orbits and their eigenvalues are computed, the spectral determinant is used to compute the escape rate. The escape rate computed from the spectral determinant is compared to Monte Carlo computations. This work augments previous studies on heteroclinic tangles by using the symbolic dynamics computed from HLD to compute periodic orbits and transport rates. For other approaches to symbolic dynamics of tangles, see Refs. [12–15, 22, 23, 64, 65].

Although we provide the machinery for computing the spectral determinant in a mixed phase space, we focus this study on a system where the accuracy of the symbolic dynamics can be verified. For a certain range of electron energy and magnetic field, the dynamics of the hydrogen atom exhibits a ternary horseshoe, meaning that the topological entropy is $\ln(3)$ and the dynamics can be described by a full shift on three symbols. For the range of parameter where the topological entropy is $\ln(3)$, the symbolic dynamics does not change and the interval of parameter is called a hyperbolic plateau. By computing periodic orbits over the ranges of hyperbolic plateaus, we can accurately compute the escape rate using the spectral determinant. We also study what happens to the convergence of the escape rate as the parameter is varied within and away from the hyperbolic plateau.

Another future goal of this work is to compare the techniques of HLD with transition state theory. Both methods use invariant manifolds [45] to compute ionization rates in Hamiltonian atomic systems modeling chemical reactions, however, the method of HLD requires a Poincaré surface of section that intersects with the periodic orbit, while transition state theory requires a Poincaré surface of section that does not intersect the periodic orbit. Both techniques are promising for studying chemical reactions in higher dimensions.

4.2 Model system and coordinates

The hydrogen atom in parallel electric and magnetic fields is modeled by the Hamiltonian

$$H = \frac{p^2}{2} - \frac{1}{r} + \frac{1}{8}B^2(x^2 + y^2) + z, \tag{4.3}$$

Where x,y, and z are the physical spatial coordinates, E and B are the scaled energy and magnetic field, written as $B = \tilde{B}\tilde{F}^{-\frac{3}{4}}$ and $E = \tilde{E}\tilde{F}^{-\frac{1}{2}}$, where $\tilde{B}$, $\tilde{F}$, and $\tilde{E}$ are the physical magnetic field strength, electric field strength, and electron energy respectively in atomic units ($e = \hbar = m_e = 1$). We fix $B = 3.5$ and $F = 1.0$ and vary the scaled electron energy E. The Hamiltonian in Eq. 4.3 has three degrees of freedom, however there exists a rotational symmetry in H, and, Eq. 4.3 can be written in terms of cylindrical coordinates ρ, z, p_ρ and p_z as

$$H(\rho, z, p_\rho, p_z) = \frac{1}{2}(p_\rho^2 + p_z^2) + V(\rho, z) = E, \tag{4.4}$$

where

$$V(\rho, z) = -\frac{1}{\sqrt{\rho^2 + z^2}} + z + B^2\rho^2 \tag{4.5}$$

Equations 4.4 and 4.3 have a Coulomb singularity at the origin, and therefore it is useful to use parabolic coordinates u, v, p_u, and p_v given by

$$u = \pm\sqrt{r + z}, \tag{4.6a}$$

$$v = \pm\sqrt{r - z}, \tag{4.6b}$$

and

$$p_u = vp_\rho + up_z, \tag{4.7a}$$

$$p_v = up_\rho - vp_z, \tag{4.7b}$$

where

$$r = \sqrt{\rho^2 + z^2} = \frac{u^2 + v^2}{2}. \tag{4.8}$$

We allow u and v to take both positive and negative values corresponding to a fourfold covering of the cylindrical coordinates. Equations 4.6b and 4.7 have the following inverse transformations:

$$\rho = uv, \tag{4.9a}$$

$$z = \frac{1}{2}(u^2 - v^2), \tag{4.9b}$$

$$p_\rho = \frac{vp_u + up_v}{u^2 + v^2}, \tag{4.10a}$$

$$p_z = \frac{up_u - vp_v}{u^2 + v^2}. \tag{4.10b}$$

We finally introduce the effective Hamiltonian which we use for all subsequent analysis,

$$h(u, v, p_u, p_v) = \frac{1}{2}(p_u^2 + p_v^2) + V(u, v) - 2, \tag{4.11}$$

where V is given by

$$V = -E(u^2 + v^2) + \frac{1}{8}B^2(u^4v^2 + u^2v^4) + \frac{1}{2}(u^4 - v^4). \tag{4.12}$$

Setting $h = 0$ in this Hamiltonian leads to the same trajectories as setting $H = E$, although parameterized by a new time-like variable s, defined by $\frac{ds}{dt} = \frac{1}{2r}$. We define a two-dimensional Poincaré surface of section in the four-dimensional u, v, p_u, p_v phase space by the constraints $u = h = 0$. A point on this surface is specified, up to the sign of p_u , by its coordinates v and p_v.

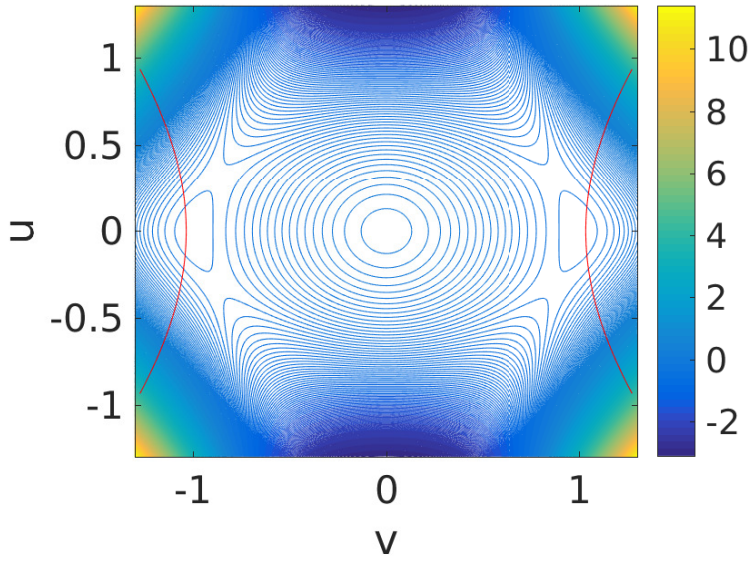

Figure 4.1. The contour plot for potential V in $u-v$ space for E=1.0 and B=3.5. The trajectory of the saddle periodic orbits projected onto the $u-v$ space are shown in red.

We define a discrete-time map M^n using this Poincaré surface of section for integers n. We define the continuous-time map $\mathcal{M}^s$ using the continuous-time variable s.

4.3 Monte Carlo computation of escape

We begin our analysis of the ionization rate for this system by first introducing the Monte Carlo method for computing the ionization rate. The Monte Carlo method serves as a benchmark for a comparison to the ionization rate computed from periodic orbits using HLD later in Sect. 4.5.2. An initial ensemble of trajectories is chosen near the fixed point, and the points are mapped forward in time using the continuous- or discrete-time version of the map. fitting to the number of survivors as a function of time using a fitting function in the form of Eq. 4.1. The escape rate can be computed both for the discrete-time mapping M^n and the continuous-time mapping $\mathcal{M}^s$, and each mapping yields a different escape rate. The continuous time version of escape counts the number of surviving trajectories as a function of the continuous time variable s. The discrete time version of escape rate counts the number of survivors as a function of iterates of the Poincaré mapping defined in Sect. 4.2.

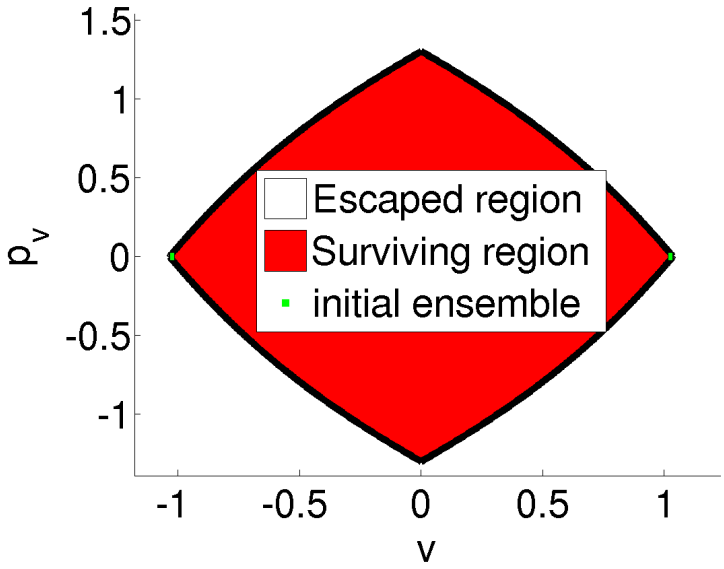

Figure 4.2. The boundary defined by the stable and unstable manifolds of the outer two fixed points, in v, p_v space for $E = 1.0$ and $B = 3.5$. The red region is the surviving region, and the white region is the escaped region. The small green square represents the initial ensemble for the Monte Carlo.

4.3.1 Discrete-time Monte Carlo decay rate

In the discrete-time case, we define our boundary for escape using the stable and manifolds of the hyperbolic fixed points in the plane defined by the Poincaré mapping, $u = 0$. Fig. 4.2 shows the initial and escaped regions for this computation. Fig. 4.3 shows the number of survivors as a function of iterate using the Poincaré surface of section, along with the fitting function used to compute the Monte Carlo ionization rate computed from fitting to the data. The fit is computed by taking the log of the data and using linear regression to extract the ionization rate. The error bars are computed as 95 percent confidence intervals on the fit.

4.3.2 Continuous-time Monte Carlo decay rate

For continuous-time decay, we define our escape using the coordinate $z = \frac{1}{2}(u^2+v^2)$. Escape is defined when this value goes below -1.0, which is sufficiently far from the nucleus that the electron will never return, and thus 'dies.' The number of survivors as a function of time is shown in Fig. 4.4.

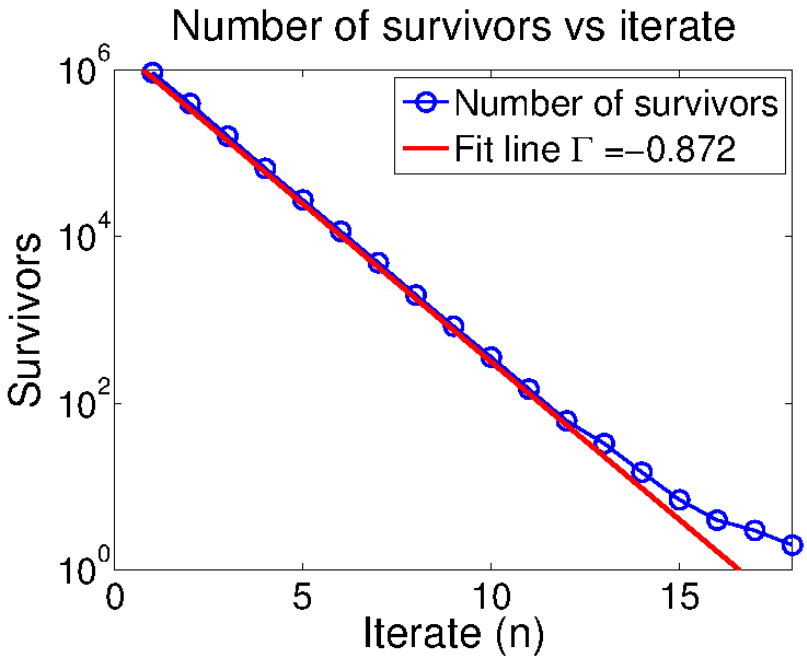

Figure 4.3. Number of survivors as a function of iterates using the Poincaré return map (red) for $E = 1$ and $B = 3.5$. The fit line used to compute the escape rate is shown in red.

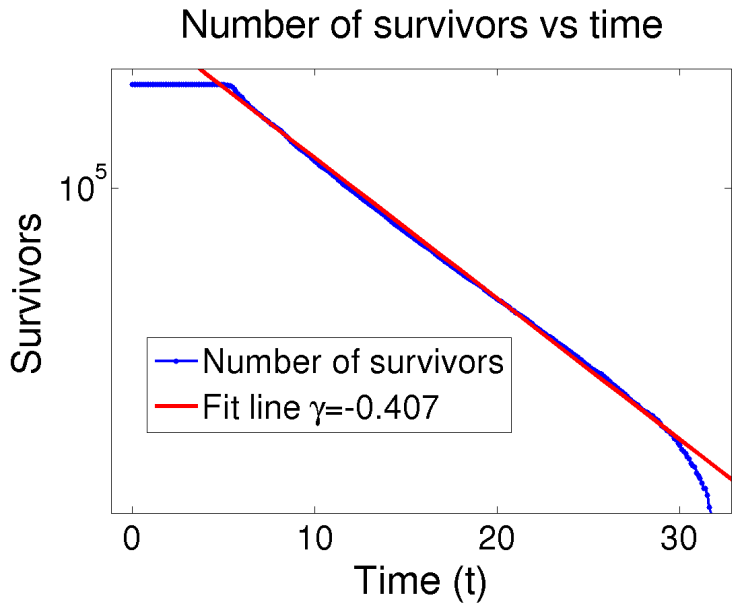

Figure 4.4. Number of survivors as a function of iterates using continuous-time t for E=1.0, B=3.5. The fit line used to compute the escape rate is shown in red.

4.4 Lobe area estimate

Another method of computing the ionization rate is with the lobe area estimate. In this method, the ionization rate is approximated based on the turnstile in 4.6. The upper-right and lower-left lobes in the figure are **escape lobes**. The ionization rate estimated from lobe area, γ_{approx}, can be computed using the formula

$$\gamma_{approx} = \frac{A_{escape}}{A_{resonance}}, \tag{4.13}$$

where A_{escape} is the sum of the areas of the escape lobes, and $A_{resonance}$ is the area of the interior zone, which is shown by itself in Fig. 4.2. The lobe area estimate method can also be improved upon using higher-order corrections, as described by Rom-Kedar [64, 65]. It would be interesting to compare the results in this paper with the method using higher-and-higher-order lobe area corrections described by Rom-Kedar.

4.5 Computing decay rate from the ternary horseshoe using periodic orbits

As we will show, the ionization rate can be computed with much fewer trajectories by utilizing HLD and computing periodic orbits. As in the previous chapters, the trellis is computed from the heteroclinic tangle attached to the fixed points. Then, the symbolic dynamics and partitions are computed using HLD. Finally, the periodic orbits are computed, and the ionization rate is computed from the periodic orbits using the spectral determinant. We choose the parameter $B = 3.5$, $E = 1.0$ because of its simple symbolic dynamics which is a full shift on three symbols. For $B = 3.5$, the trellis maintains a full shift on three symbols for the E interval [0.324, 1.3]. This interval of E was detected by computing the symbolic dynamics as a function of E and detecting intervals over which it does not change. Figure 4.5 shows the topological entropy as a function of E, which is equal to the log of the largest eigenvalue of the transition matrix representing the system's symbolic dynamics. The stable and unstable manifolds computed for applying HLD are are shown in Fig. 4.6. The homotopic lobe dynamics technique allows us to partition this into three regions and label them as 0,1, and 2 shown in Fig. 4.7. The corresponding transition graph is shown in Fig. 4.8. Seeds

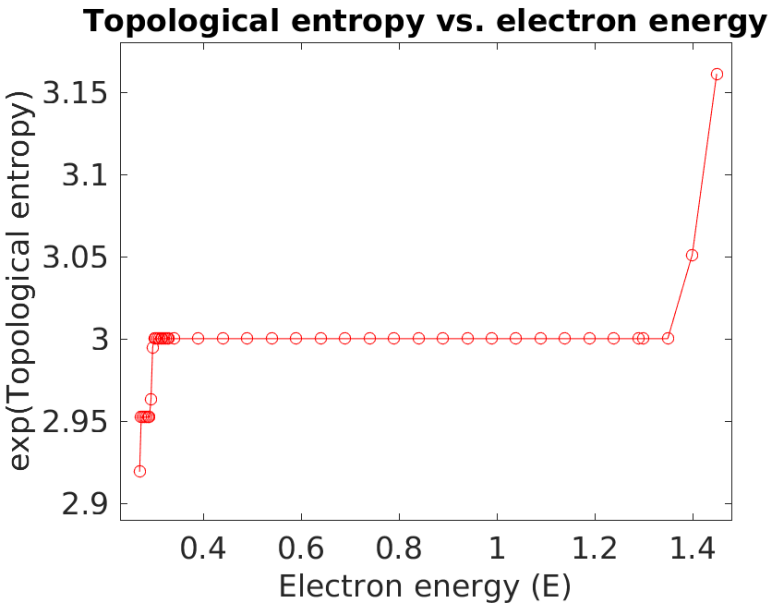

Figure 4.5. The topological entropy as a function of E computed using HLD. The interval [0.32, 1.3] is found to be a hyperbolic plateau with topological entropy equal to $\ln(3)$.

are chosen based on the partitions, and the periodic orbits are computed using a multi-shooting Newton's method. Appendix A describes the computation of a seed based on the partitions.

4.5.1 Decay rate results using periodic orbits

Once all the periodic orbits are computed, the decay rate is computed using the spectral determinant. The algorithm for computing the discrete-time ionization rate using the discrete-time spectral determinant is described in Sect. 3.2. The continuous-time ionization rate is computed in the exact same fashion, only replacing C_n in Eq. 4.15 with

$$C_n = \sum_p n_p e^{-s*T_p} \sum_{r=1}^{\infty} \frac{1}{|\det(1 - M_p^r)|} \delta_{rn_p n}, \tag{4.14}$$

where T_p is the continuous-time period of the periodic orbit and $e^- s$ replaces z, i.e., s is th variable that is varied in order to find the zeros of the spectral determinant.

Fig. 4.10 shows the approximation to the decay rate using periodic orbits. The data on the far right of the figure uses all periodic orbits, and therefore represents the best estimate for the decay rate.

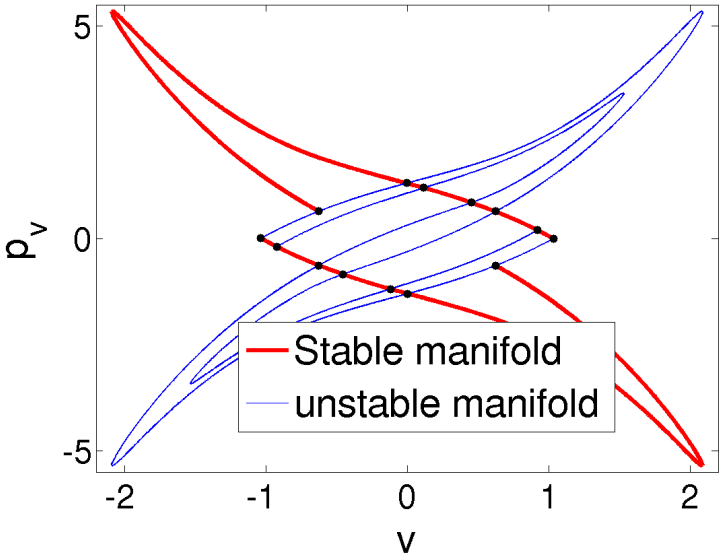

Figure 4.6. The stable and unstable manifolds for the two outer fixed points, i.e. the trellis for E=1.0, B=3.5. The HLD technique computes the topological entropy of this trellis as $\ln(3)$, with symbolic dynamics shown in Fig. 4.8, and the corresponding partitions are shown in Fig. 4.7.

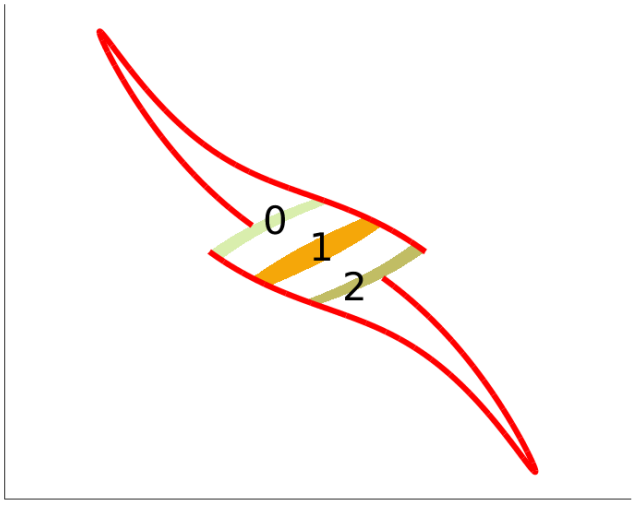

Figure 4.7. The partitions generated by HLD. The corresponding symbolic dynamics is shown in Fig. 4.8 and the tangle used to compute the partitions and symbolic dynamics is shown in Fig. 4.6.

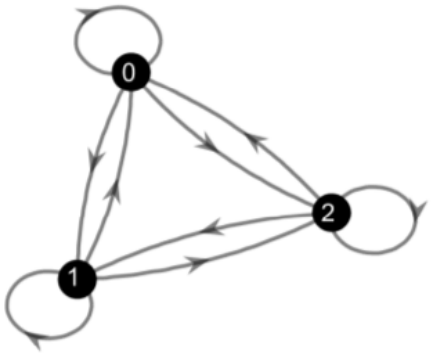

Figure 4.8. The transition graph for the ternary horseshoe. The corresponding partitions for E=1.0, B=3.5 are shown in Fig. 4.7 and the tangle used to compute the partitions and symbolic dynamics is shown in Fig. 4.6.

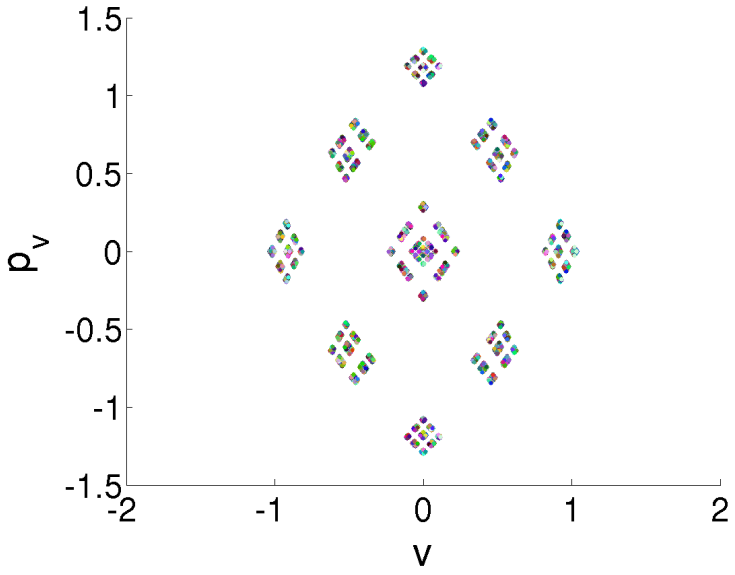

Figure 4.9. All periodic orbits up to period 10 for E=1.0, B=3.5, computed from the symbolic dynamics. There are in total 9382 orbits.

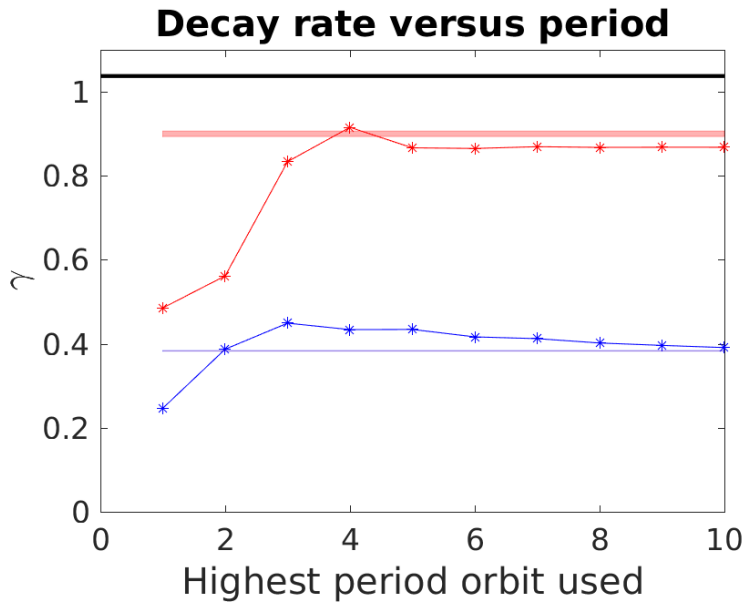

Figure 4.10. Approximation to the decay rate using periodic orbits at B=3.5, E=1.0. All periodic orbits are computed up to a given period, and the decay rate is plotted as a function of the highest period orbit used in the spectral determinant computation. The red lines are the discrete-time periodic orbit decay rate (red line with asterix markers) and the Monte Carlo decay rate (red band). The red lines are the continuous-time periodic orbit decay rate (blue line with asterix markers) and the Monte Carlo decay rate (blue band). The lobe area estimate for the discrete-time decay rate is shown in black. Although the system is fully hyperbolic, the lobe area estimate does not accurately capture the true decay rate.

4.5.2 Periodic orbit continuation

Once periodic orbits are computed for a given electron energy value, they can be used as seeds for computing orbits for a nearby electron energy value, because a small change in electron energy results in a small change in the locations of the periodic orbits. Thus, the electron energy E can be varied iteratively and periodic orbits can be computed over a range of parameter value, which is a technique known as periodic orbit continuation. When a periodic orbit disappears or is no longer stable, it is removed from the computation. Fig. 4.11 shows the result for discrete-time decay at period 10 for different E values where the symbolic dynamics remains the same.

4.5.3 Modifying the definition of escape by removing a region of phase space

We showed in Sect. 4.5.2 that given the periodic orbits up to a given period within the resonance zone, one can compute the escape rate from the resonance zone, i.e. the ionization rate.Another benefit of the periodic orbit computation is that regions of phase space can be removed by removing

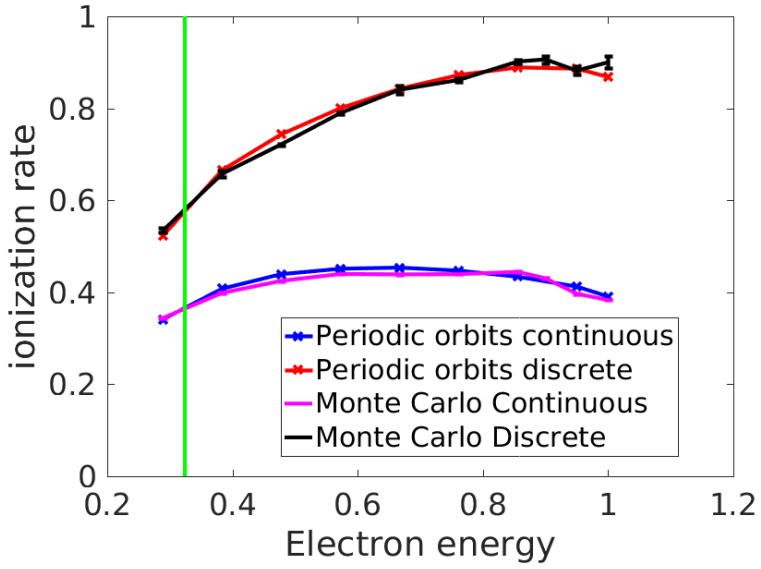

Figure 4.11. Ionization rate computed for the E interval [0.29, 1.0]. The discrete-time ionization rate is shown in red using the spectral determinant and in black using a Monte Carlo technique. The continuous-time ionization rate is shown in blue using the spectral determinant and in magenta using a Monte Carlo technique. The lowest E value with a topological entropy of $\ln(3)$ is plotted in green.

the periodic orbits in that region. Computing the escape rate with a removed region has physical applications. For example, in an experiment where the detector is closer to the nucleus, the escape rate measured by the detector can be computed by removing the periodic orbits that lie past the detector. Although the two rates are physically very similar, we will refer to the escape rate using the removed region as the *escape rate*, and the original definition of escape will be called the *ionization rate*.

We compute the Monte Carlo and periodic orbit escape rates using this new definition of escape. For computing the escape rate with removed region, Fig. 4.12 shows a chosen removed region in black. All periodic orbits that land in the chosen region are removed from the escape rate computation, and hose periodic orbits are not shown. Out of the original 9381 periodic orbits, 3080 are removed from the computation. The periodic orbits that are removed have points that lie inside the removed region, but they also have points that land outside the removed region, so removing them still removes relevant information from the periodic orbit computation. However, the escape rate computed using the remaining set of orbits should still converge to the true value as more and more orbits are included.

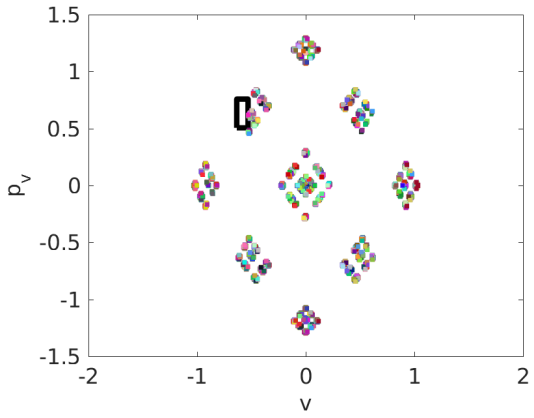

Figure 4.12. The periodic orbits computed up to period 10 with a chosen removed region. The periodic orbits that land in the black region are removed from the computation, and are not shown. The corresponding escape rate computed is shown in Fig. 4.13.

To compute the Monte Carlo simulation with the removed region, the initial ensemble of trajectories is iterated exactly the same as in Sect. 4.3, only now there is an additional criterion for escape, which is landing in the black region. In addition to the trajectories that are said to escape by a certain iterate in Sect. 4.3, points that land in the black region are also said to have escaped. This leads to an escape rate that must be greater than the ionization rate computed in Sect. 4.3. Figure 4.13 shows the approximation to the decay rate as a function of the highest period orbit used, which shows a good convergence within the Monte Carlo error bounds. The escape rate computed using the removed region in Fig. 4.13 converges more slowly than the ionization rate in Fig. 4.10 computed using all orbits.

4.6 Studying the semiclassical version of the system

Discovering the ternary horseshoe in a realistic, classically chaotic atomic system is the crux of this work so far and leads to the easy computation of periodic orbits. Now that we have computed periodic orbits for this system, we can study it in depth using periodic orbit theory, including the system's quantum and semiclassical counterparts. Cvitanovic et. al [17] previously analyzed the quantum and classical correspondence using periodic orbits in the three-disk scattering system due to its simple symbolic dynamics. In our system, we can apply the same analysis. Once this analysis is completed, it can be used to guide novel experiments studying quantum chaos. The algorithm

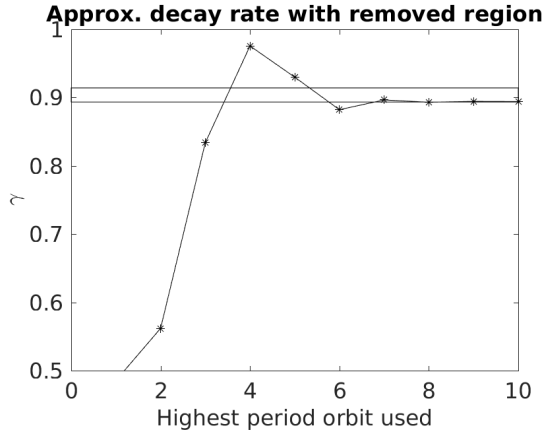

Figure 4.13. The approximation to the escape rate as a function of the highest period periodic orbit used in the computation (asterisks), while removing the periodic orbits that land in a certain chosen region, which is shown in Fig. 4.12. The black rectangle shows the corresponding Monte Carlo escape rate bounds.

used for computing the classical spectral determinant is shown in Sect. 3.2, and the semiclassical spectral determinant is computed in the exact same fashion, only replacing C_n from Eq. 4.15 with the following trace coefficients:

$$C_n = \sum_p n_p e^{-s*T_p + i\hbar - i\pi m/2} \sum_{r=1}^{\infty} \frac{1}{|\det(1 - M_p^r)|} \delta_{r n_p n}, \tag{4.15}$$

where T_p is the continuous-time period of the periodic orbit, s is th variable that is varied in order to find the zeros of the spectral determinant, and $i = \sqrt{-1}$ and m is the Maslov index. The Maslov index is equal to the number of times the unstable vector rotates around the trajectory as one moves along it.

In order to complete the analysis, the quantum resonances must be computed using the periodic orbits. Our collaborator Hiroshi Teramoto has done some initial computations for quantum resonances using a technique called complex scaling. Once resonances are found, the classical periodic orbits will be continued using periodic orbit continuation into that set of parameter values, which could be complex.

4.6.1 Computing the Maslov index from symbolic dynamics

Since the Maslov index is a purely topological quantity that does not vary with coordinate transformations, the Maslov index should be computable from the symbolic dynamics alone. We

have come up with a scheme where each symbol contributes a certain number of *turns*. For example, in Fig. 4.7, the partitions labeled **0** and **2** each contribute 1 to the Maslov index, and the partition labeled **1** contributes 2 to the Maslov index. For a periodic orbit with itinerary 0121, for example, the total Maslov index is 1+2+1+2 = 6. Although we have not proven this scheme, we showed by computing the Maslov index numerically that this scheme works up to period 7, and we postulate that it should work for higher periods as well.

4.7 Concluding remarks

We have computed periodic orbits in a full ternary horseshoe over a range of initial electron energies in the hydrogen atom in parallel electric and magnetic fields. The lower and upper limits of the hyperbolic plateau exhibiting a ternary horseshoe were found using HLD. The ionization rate was accurately computed from the periodic orbits for all electron energies within the hyperbolic plateau. The escape rate was also computed in the case where a region of phase space is removed, which results in removing the periodic orbits from the Monte Carlo escape rate computation.

The future goal of this work is to compute the semiclassical resonances. Further work would include finding other hyperbolic plateaus, and computing multi-exponential escape rates for this system as in Sect. 3.7.

Chapter 5

Understanding Transport Bottlenecks By Measuring the Network Betweenness Centrality

Having a firm grasp on the symbolic dynamics of a system can potentially provide more information than just transport rates. For example, one can ask whether the symbolic dynamics can help to find the locations of transport bottlenecks. A **transport bottleneck** is a region of phase space responsible for a large portion of transport between two other regions of phase space. Given the two zones, Zone I and Zone II in the inset of Fig. 3.12 from Chapter 3, for example, consider the set of trajectories that move from Zone I to Zone II. Regions regions which many of those trajectories pass through are called transport bottlenecks. Computing transport bottlenecks is an important problem in chemical reaction dynamics, and other techniques of computing transport bottlenecks utilize normal form theory and transition state theory [45–47, 72]. We wish to use network properties of symbolic dynamics to infer useful information about phase space geometry. In this preliminary work, we try to infer information about transport bottlenecks from the system's symbolic dynamics computed with HLD.

5.1 Defining communities in a symbolic dynamics network

We choose a parameter value of the Hénon map, $k = 3.963$, which contains a very complex symbolic dynamics, exhibiting two zones just like the system studied in Fig. 3.12. One method to visualize complex graphs such as the symbolic dynamics transition graph for $k = 3.963$ is using the force-directed layout [30], which uses attractive forces between adjacent nodes and repelling forces between distant nodes. Shown in Figure 5.1, this visual representation of the graph implies that there may be a community structure within the graph. A **community** in a graph is a set of nodes that are denseley connected internally, but may not be densely connected to nodes outside the set. For Fig. 5.1, we can visually infer that some community structure exists, i.e, nodes on the left of Fig. 5.1 are clustered together and nodes on the right of Fig. 5.1 are clustered together, without having many connections between them. Although this is not a rigorous definition of detecting communities, we use this as a justification for defining Zone I to be its own community and Zone II to be its own community in the subsequent analysis. A plethora of graph algorithms exist for detecting communities in networks [24]. A future approach of this work will use community detection algorithms for finding communities, rather than defining them based on zones. From now on, we will refer to the set of nodes in Zone I as Community I, and the set of nodes in Zone II as Community II. We will start the analysis of this graph along with the chosen set of communities using a modification of a quantity called betweenness centrality.

5.2 Modified Betweenness Centrality

The betweenness centrality is a way to measure the "importance" of nodes by seeing how many shortest paths pass through a given node.

$$C_B(g) = \sum_{(a,b)} \frac{n_{ab}(g)}{N_{ab}} \tag{5.1}$$

where $n_{ab}(g)$ is the number of shortest paths from a to b passing through g, and N_{ab} is the total number of shortest paths from a to b. In the original definition of betweenness centrality, the sum in Eq. 5.1 is taken over all pairs of nodes (a, b). This gives the "importance" in a node as viewing

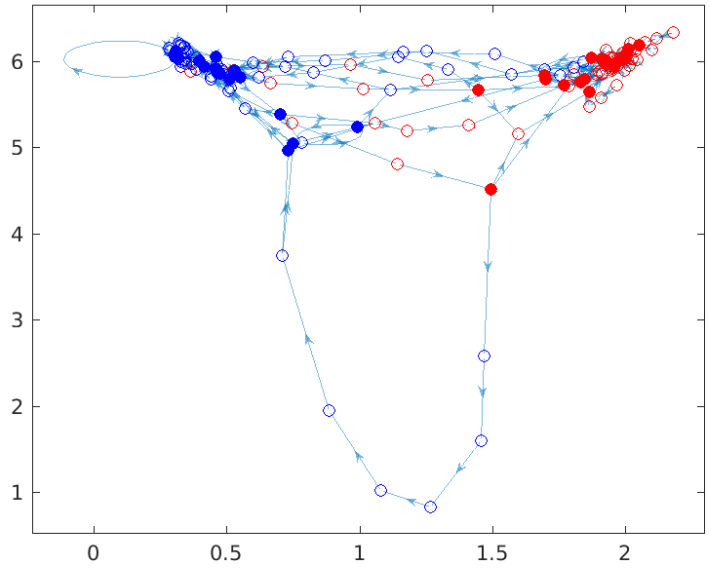

Figure 5.1. The symbolic dynamics network for the Hénon map for $k = 3.963$.

how it can transport material throughout all the other nodes. However, we are interested in viewing the transport *between zones*. We modified this definition by narrowing down which pairs (a, b) we include in the sum. Therefore we define $C_{B,i\to o}$ as the betweenness centrality from inner to outer, where the sum is taken over all pairs a, b where a is in the inner region and b is in the outer region. Likewise the value $C_{B,o\to i}$ is defined as the betweenness centrality from outer to inner, where the sum is taken over all pairs a, b where a is in the outer region and b is in the inner region. In both cases, the value $C_{B,i\to o}$ or $C_{B,o\to i}$ can be computed for any node g in the graph. We propose that this modified version of betweenness centrality can reveal transport structure in the symbolic dynamics network, and can help identify transport bottlenecks. We computed betweeness centrality for all the nodes for our test case, the Hénon map at $k = 3.963$. The distribution of $C_{B,i\to o}$ is shown in Fig. 5.2, and the distribution of $C_{B,o\to i}$ is shown in Fig. 5.3. In both cases, a majority of the nodes do not have a high value of betweenness centrality, which indicates that not all nodes are equally responsible for transport between the two zones.

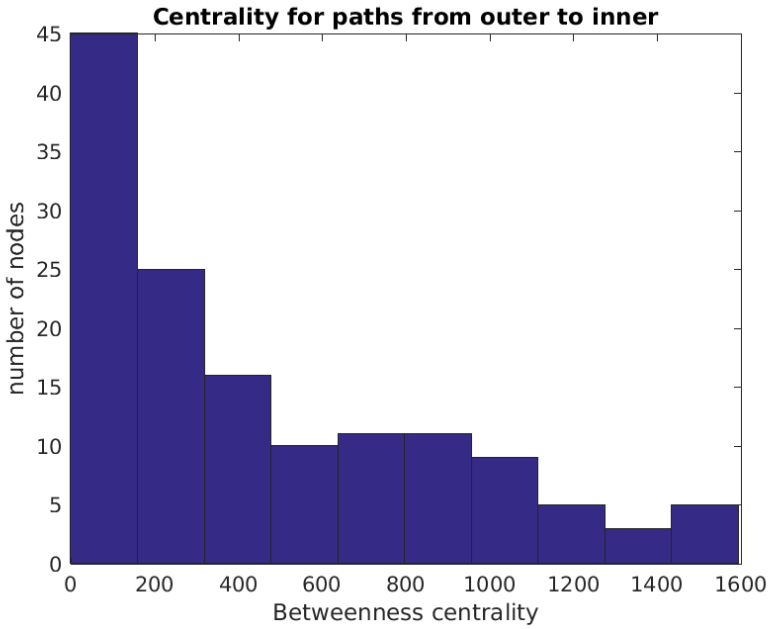

Figure 5.2. The distribution of betweenness centrality from Zone II to Zone I, $C_{B,i\to o}$.

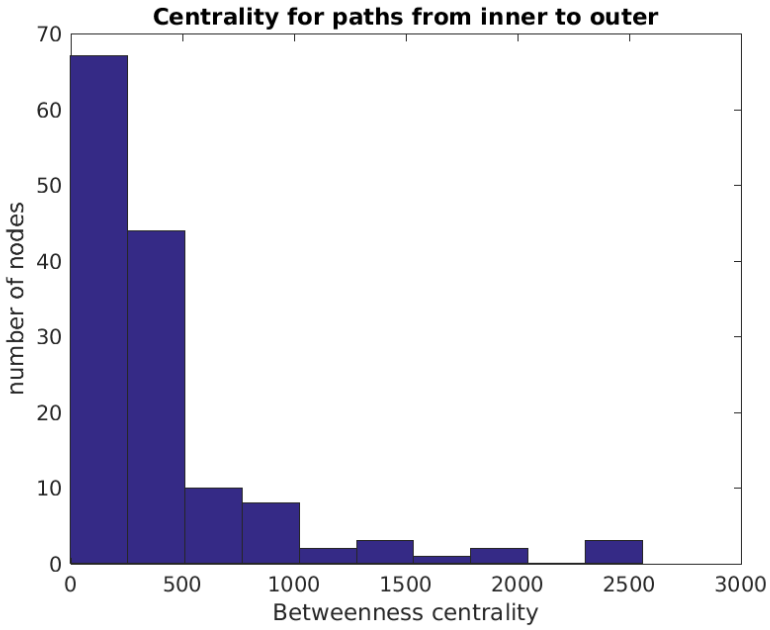

Figure 5.3. The distribution of betweenness centrality from Zone II to Zone I, $C_{B,o\to i}$.

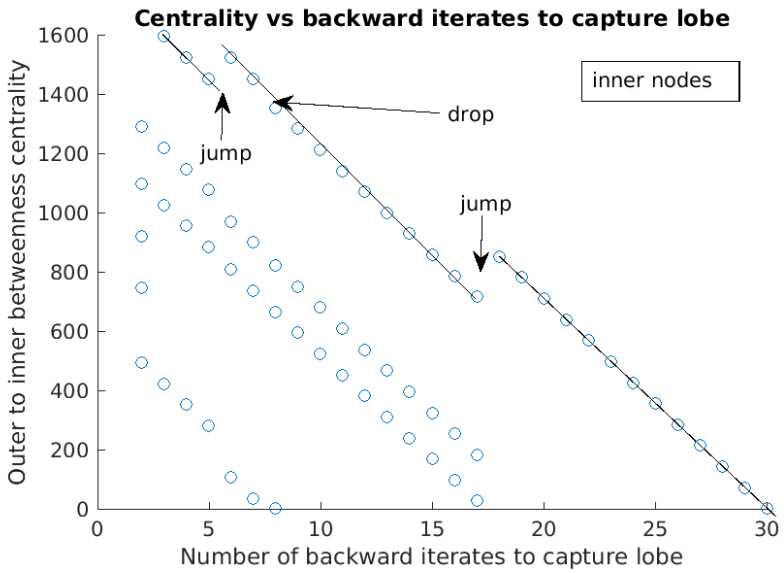

Figure 5.4. The betweenness centrality $C_{B,o\to i}$ computed as a function of the number of backward iterates to the capture lobe of Zone II. The nodes with a line through them indicate the subgraph studied in Fig 5.5.

5.3 Computing betweenness centrality as a function of the 'distance' to the capture lobe

The two zones Zone I and Zone II each have an escape lobe and a capture lobe that are responsible for transport between them. All nodes that escape a given zone in one iterate must pass through an escape lobe, and are captured in a capture lobe. In Zone I, a node that that has just been captured or just escaped might have high betweenness centrality, and this might explain the outliers in Figs. 5.2 and 5.3. It was found by inspecting the outlying nodes, that all the nodes with high betweenness centrality $C_{B,i\to o}$ lie in Zone I, and the nodes with high betweenness centrality $C_{B,o\to i}$ are in Zone II. We want to know about the relationship of betweenness centrality to the transport between zones, so therefore, we plot $C_{B,i\to o}$ against the number of iterates it takes for the node to escape from Zone II, and we plot $C_{B,o\to i}$ as a function of the number of iterates it takes for the node to be captured by Zone I. Figure 5.4 shows a scatter plot over all nodes in Zone II plotting the betweenness centrality $C_{B,o\to i}$ as a function of the number of backward iterates to the escape capture of Zone II. As expected, there is a downward trend showing that the nodes with the highest betweenness centrality have only a few iterates to the escape lobe. The nodes with the highest betweenness centrality seem to lie on a straight line. The slope of this line is equal to the

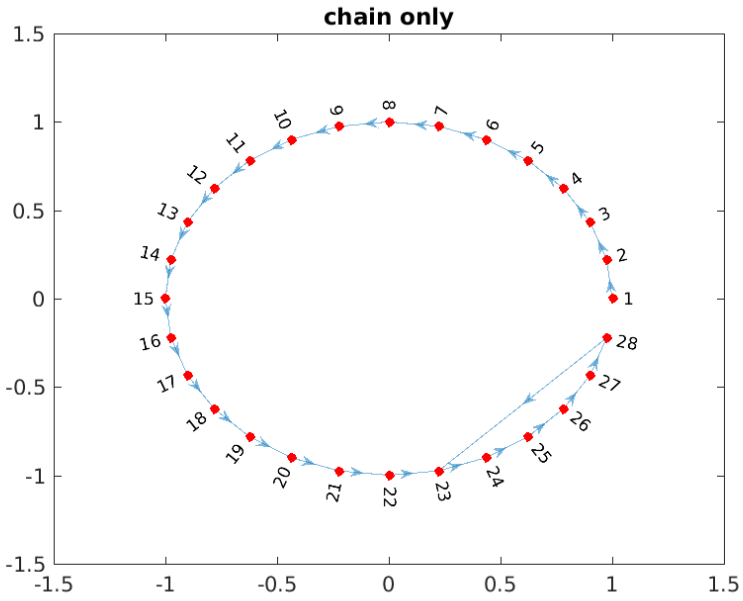

Figure 5.5. The distribution of betweenness centrality from Zone II to Zone I, $C_{B,i\to o}$.

total number of nodes in Zone I. The reason for this becomes clear when studying the subgraphs containing the chains. However, it was initially surprising why the betweenness centrality lies on straight lines. The reason for this is due to chains of nodes. That is, for the nodes with highest betweenness centrality, there is a long chain of nodes, with little or no branching out, that leads to the node that escapes. An example of such a chain is shown in Figs. 5.5- 5.6. The jumps and drops in the betweenness centrality occur exactly where there are incoming nodes (for jumps) or outgoing nodes (for drops) into the chain, as shown in Fig. 5.6.

The chaining leads to all the nodes in the chain contributing to the centrality computed from Eq. 5.1, and leads to a high betweenness centrality value computed for that node. When an incoming node comes into the chain, it adds to the centrality. When an outgoing node comes out of the chain, then some shortest paths can go out of the zone without passing through the final node, leading to a drop in the betweenness centrality computed. This shows how the chaining structure of the symbolic dynamics can be computed from our modified version of betweenness centrality.

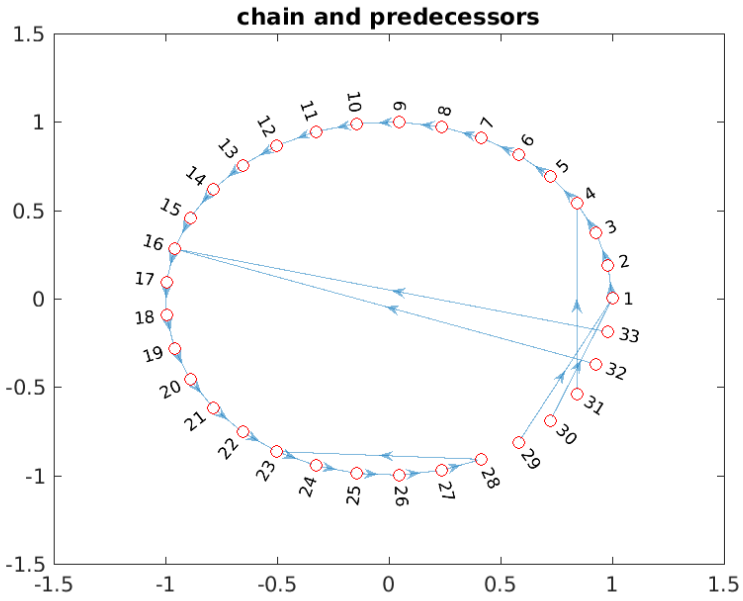

Figure 5.6. The distribution of betweenness centrality from Zone II to Zone I, $C_{B,i\to o}$.

5.4 Conclusions and future work

This work is still in its early stages and we are trying to address bigger questions. For one, it is not clear whether the structures noted here are a consequence of the method of computation of symbolic dynamics, or whether they are an inherent property of the system. In order to test this, it would be useful to compute betweenness centrality using symbolic dynamics computed from different methods. Futhermore, the definition of communities based on the resonance zones seems to work, but it may be useful to check if the resonance zones themselves can be identified using only knowledge of the symbolic dynamics. A future goal of this work is to compute resonance zones in high-dimensional systems using network properties of symbolic dynamics.

5.5 Acknowledgements

The author thanks Mikito Toda as this project was born under his supervision in Nara. The author also thanks Tamiki Komatsuzaki, Hiroshi Teramoto, and Kevin Mitchell for their supervision over this project. We acknowledge the NSF EAPSI scholarship for funding this work.

Bibliography

[1] Detecting and locating near-optimal almost-invariant sets and cycles. *SIAM Journal on Scientific Computing*, 24(6):1839–1863, 2003.

[2] M. R. Allshouse and J.-L. Thiffeault. *Physica D: Nonlinear Phenomena*, 241(2):95–105, 2012.

[3] Z. Arai. On hyperbolic plateaus of the hénon map. *Experimental Mathematics*, 16(2):181–188, 2007.

[4] M. Bestvina and M. Handel. *Topology*, 34:109, 1995.

[5] A. Beuf, J.-N. Gence, P. Carrière, and F. Raynal. *International Journal of Heat and Mass Transfer*, 53(4):684–693, 2010.

[6] P. Boyland. *Topology and its Applications*, 58(3):223–298, 1994.

[7] P. Boyland, M. Stremler, and H. Aref. *Physica D: Nonlinear Phenomena*, 175(1):69–95, 2003.

[8] P. L. Boyland, H. Aref, and M. A. Stremler. *J. Fluid Mech.*, 403:277–304, 2000.

[9] M. Budisic and J.-L. Thiffeault. *Chaos*, 25(8):–, 2015.

[10] S. Candelaresi, D. I. Pontin, and G. Hornig. Quantifying the tangling of trajectories using the topological entropy. *arXiv preprint arXiv:1702.00441*, 2017.

[11] P. Collins. In *Geometry and topology in dynamics*, volume 246 of *Contemp. Math.*, pages 65–86. Amer. Math. Soc., Providence, RI, 1999.

[12] P. Collins. *Int. J. Bifurcation Chaos Appl. Sci. Eng.*, 12:605–617, 2002.

[13] P. Collins. *Dyn. Syst.*, 19:1–39, 2004.

[14] P. Collins. *Dyn. Syst.*, 20:369–400, 2005.

[15] P. Collins. *Exp. Math.*, 14(1):75–86, 2005.

[16] P. Cvitanović, R. Artuso, R. Mainieri, G. Tanner, and G. Vattay. *Chaos: Classical and Quantum*. Niels Bohr Institute, Copenhagen, 2010. `ChaosBook.org`.

[17] P. Cvitanović and B. Eckhardt. Periodic-orbit quantization of chaotic systems. *Physical review letters*, 63(8):823, 1989.

[18] R. L. Davidchack, Y.-C. Lai, E. M. Bollt, and M. Dhamala. *Physical Review E*, 61(2):1353, 2000.

[19] S. Day, R. Frongillo, and R. Trevino. Algorithms for rigorous entropy bounds and symbolic dynamics. *SIAM Journal on Applied Dynamical Systems*, 7(4):1477–1506, 2008.

[20] M. Du and J. Delos. Effect of closed classical orbits on quantum spectra: Ionization of atoms in a magnetic field. i. physical picture and calculations. *Physical Review A*, 38(4):1896, 1988.

[21] M. Du and J. Delos. Effect of closed classical orbits on quantum spectra: Ionization of atoms in a magnetic field. ii. derivation of formulas. *Physical Review A*, 38(4):1913, 1988.

[22] R. W. Easton. *Transactions of the American Mathematical Society*, 294(2):719–732, 1986.

[23] R. W. Easton. Oxford Univ. Press, 1998.

[24] S. Fortunato. Community detection in graphs. *Physics reports*, 486(3):75–174, 2010.

[25] R. M. Frongillo. Topological entropy bounds for hyperbolic plateaus of the h\'enon map. *arXiv preprint arXiv:1001.4211*, 2010.

[26] G. Froyland. *Physica D: Nonlinear Phenomena*, 200(3):205–219, 2005.

[27] G. Froyland, O. Junge, and G. Ochs. *Physica D: Nonlinear Phenomena*, 154(1):68–84, 2001.

[28] G. Froyland and K. Padberg. *Physica D: Nonlinear Phenomena*, 238(16):1507–1523, 2009.

[29] G. Froyland and K. Padberg-Gehle. In *Ergodic Theory, Open Dynamics, and Coherent Structures*, pages 171–216. Springer, 2014.

[30] T. M. Fruchterman and E. M. Reingold. Graph drawing by force-directed placement. *Software: Practice and experience*, 21(11):1129–1164, 1991.

[31] R. H. Goodman and J. K. Wróbel. High-order bisection method for computing invariant manifolds of two-dimensional maps. *International Journal of Bifurcation and Chaos*, 21(07):2017–2042, 2011.

[32] E. Gouillart, J.-L. Thiffeault, and M. D. Finn. *Phys. Rev. E*, 73:036311, Mar 2006.

[33] P. Grover, S. D. Ross, M. A. Stremler, and P. Kumar. *Chaos*, 22(4):–, 2012.

[34] M. C. Gutzwiller. Periodic orbits and classical quantization conditions. *Journal of Mathematical Physics*, 12(3), 1971.

[35] M. C. Gutzwiller. *Chaos in Classical and Quantum Mechanics*. Springer, New York, 1990.

[36] R. Hagiwara and A. Shudo. An algorithm to prune the area-preserving hénon map. *Journal of Physics A: Mathematical and General*, 37(44):10521, 2004.

[37] T. Haszpra and T. Tél. *Journal of the Atmospheric Sciences*, 70(12):4030–4040, 2013.

[38] M. Hénon. A two-dimensional mapping with a strange attractor. *Communications in Mathematical Physics*, 50(1):69–77, 1976.

[39] A. Holle, J. Main, G. Wiebusch, H. Rottke, and K. Welge. Quasi-landau spectrum of the chaotic diamagnetic hydrogen atom. *Physical review letters*, 61(2):161, 1988.

[40] A. Holle, G. Wiebusch, J. Main, B. Hager, H. Rottke, and K. Welge. Diamagnetism of the hydrogen atom in the quasi-landau regime. *Physical review letters*, 56(24):2594, 1986.

[41] K. C. Howell, B. T. Barden, R. S. Wilson, and M. W. Lo. Trajectory design using a dynamical systems approach with application to genesis. *Astrodynamics 1997*, pages 1665–1684, 1997.

[42] C. Jaffé, S. D. Ross, M. W. Lo, J. Marsden, D. Farrelly, and T. Uzer. Statistical theory of asteroid escape rates. *Phys. Rev. Lett.*, 89(1):011101, Jun 2002.

[43] R. V. Jensen, S. M. Susskind, and M. M. Sanders. "chaotic ionization of highly excited hydrogen atoms: Comparison of classical and quantum theory with experiment". *Phys. Rep.*, 201(1):1 – 56, 1991.

[44] D. Kleppner and J. B. Delos. Beyond quantum mechanics: Insights from the work of martin gutzwiller. *Foundations of Physics*, 31(4):593–612, 2001.

[45] T. Komatsuzaki and R. S. Berry. Dynamical hierarchy in transition states: Why and how does a system climb over the mountain? *Proceedings of the National Academy of Sciences*, 98(14):7666–7671, 2001.

[46] T. Komatsuzaki, K. Hoshino, and Y. Matsunaga. Regularity in chaotic transitions on multibasin landscapes. *Geometric Structures of Phase Space in Multidimensional Chaos: Applications to Chemical Reaction Dynamics in Complex Systems, Volume 130*, pages 257–313, 2005.

[47] C.-B. Li, M. Toda, and T. Komatsuzaki. Bifurcation of no-return transition states in many-body chemical reactions. *The Journal of chemical physics*, 130(12):124116, 2009.

[48] T.-Y. Li and J. A. Yorke. Period three implies chaos. *American mathematical monthly*, pages 985–992, 1975.

[49] J. Main, G. Wiebusch, A. Holle, and K. Welge. New quasi-landau structure of highly excited atoms: The hydrogen atom. *Physical review letters*, 57(22):2789, 1986.

[50] J. Main, G. Wiebusch, K. Welge, J. Shaw, and J. Delos. Recurrence spectroscopy: Observation and interpretation of large-scale structure in the absorption spectra of atoms in magnetic fields. *Physical Review A*, 49(2):847, 1994.

[51] V. V. Meleshko and A. M. Gomilko. *Proceedings of the Royal Society of London A: Mathematical, Physical and Engineering Sciences*, 460(2043):807–819, 2004.

[52] K. Mitchell, J. Handley, J. Delos, and S. Knudson. *Chaos: An Interdisciplinary Journal of Nonlinear Science*, 13(3):892–902, 2003.

[53] K. A. Mitchell. *Physica D*, 238(7):737–763, 2009.

[54] K. A. Mitchell. *Physica D: Nonlinear Phenomena*, 241(20):1718 – 1734, 2012.

[55] K. A. Mitchell and J. B. Delos. *Physica D: Nonlinear Phenomena*, 221(2):170 – 187, 2006.

[56] K. A. Mitchell and J. B. Delos. The structure of ionizing electron trajectories for hydrogen in parallel fields. *Physica D: Nonlinear Phenomena*, 229(1):9–21, 2007.

[57] K. A. Mitchell, J. P. Handley, B. Tighe, A. Flower, and J. B. Delos. Analysis of chaos-induced pulse trains in the ionization of hydrogen. *Phys. Rev. A*, 70:043407, 2004.

[58] K. A. Mitchell, J. P. Handley, B. Tighe, A. Flower, and J. B. Delos. Chaos-induced pulse trains in the ionization of hydrogen. *Phys. Rev. Lett.*, 92:073001, 2004.

[59] S. Newhouse and T. Pignataro. *Journal of Statistical Physics*, 72(5-6):1331–1351, 1993.

[60] S. E. Newhouse. *Ergodic Theory and Dynamical Systems*, 8(8*):283–299, 1988.

[61] J. Nickolls, I. Buck, M. Garland, and K. Skadron. Scalable parallel programming with cuda. *Queue*, 6(2):40–53, 2008.

[62] P. S. Pacheco. *Parallel programming with MPI*. Morgan Kaufmann, 1997.

[63] P. Rao, A. Duggleby, and M. A. Stremler. *Journal of Fluids Engineering*, 134(4):041203, 2012.

[64] V. Rom-Kedar. *Physica D: Nonlinear Phenomena*, 43(2):229–268, 1990.

[65] V. Rom-Kedar. *Nonlinearity*, 7(2):441, 1994.

[66] S. Smale. *Bulletin of the American mathematical Society*, 73(6):747–817, 1967.

[67] M. A. Stremler and J. Chen. *Physics of Fluids*, 19(10):–, 2007.

[68] M. A. Stremler, F. Haselton, and H. Aref. *Philosophical Transactions of the Royal Society of London A: Mathematical, Physical and Engineering Sciences*, 362(1818):1019–1036, 2004.

[69] M. A. Stremler, S. D. Ross, P. Grover, and P. Kumar. *Phys. Rev. Lett.*, 106:114101, Mar 2011.

[70] A. D. Stroock, S. K. W. Dertinger, A. Ajdari, I. Mezic, H. A. Stone, and G. M. Whitesides. *Science*, 295(5555):647–651, 2002.

[71] M. Stroock, Dertinger Adjari. *Philosophical Transactions of the Royal Society of London A: Mathematical, Physical and Engineering Sciences*, 362(1818):971–986, 2004.

[72] H. Teramoto, M. Toda, M. Takahashi, H. Kono, and T. Komatsuzaki. Mechanism and experimental observability of global switching between reactive and nonreactive coordinates at high total energies. *Phys. Rev. Lett.*, 115:093003, Aug 2015.

[73] J.-L. Thiffeault. *Phys. Rev. Lett.*, 94:084502, Mar 2005.

[74] J.-L. Thiffeault. *Chaos: An Interdisciplinary Journal of Nonlinear Science*, 20(1):017516, 2010.

[75] T. Topçu and F. Robicheaux. Chaotic ionization of a highly excited hydrogen atom in parallel electric and magnetic fields. *Journal of Physics B: Atomic, Molecular and Optical Physics*, 40(10):1925, 2007.

[76] Z. YoU, E. J. Kostelich, and J. A. Yorke. *International Journal of Bifurcation and Chaos*, 1(03):605–623, 1991.

[77] L.-S. Young. In *Entropy*, pages 313–327. Princeton University Press Princeton, NJ, 2003.